

Stony Brook University



OFFICIAL COPY

The official electronic file of this thesis or dissertation is maintained by the University Libraries on behalf of The Graduate School at Stony Brook University.

© All Rights Reserved by Author.

Lead Optimization and Slow-Onset Inhibition of the Enoyl-ACP Reductase (InhA)

from *Mycobacterium Tuberculosis*

A Dissertation Presented

by

Pan Pan

to

The Graduate School

in Partial Fulfillment of the

Requirements

for the Degree of

Doctor of Philosophy

in

Chemistry

Stony Brook University

August 2012

Stony Brook University

The Graduate School

Pan Pan

We, the dissertation committee for the above candidate for the
Doctor of Philosophy degree, hereby recommend
acceptance of this dissertation.

**Peter J. Tonge – Dissertation Advisor
Professor, Department of Chemistry**

**Francis Johnson - Chairperson of Defense
Professor, Department of Chemistry**

**David F. Green – Third Committee Member of Defense
Professor, Department of Chemistry**

**Stephen G. Walker – Outside Committee Member of Defense
Associate Professor, School of Dental Medicine, Stony Brook University**

This dissertation is accepted by the Graduate School

Charles Taber
Interim Dean of the Graduate School

Abstract of the Dissertation

**Lead Optimization and Slow-Onset Inhibition of the Enoyl-ACP Reductase (InhA)
from *Mycobacterium Tuberculosis***

by

Pan Pan

Doctor of Philosophy

in

Chemistry

Stony Brook University

2012

The enoyl-ACP reductase (InhA) catalyzes the last step of fatty acid biosynthesis in *Mycobacterium tuberculosis*, and is a validated target for antitubercular drugs. Our group previously reported diaryl ether InhA inhibitors that are highly active against *M. tuberculosis* (MIC = 3.15 $\mu\text{g}/\text{mL}$). Further studies showed that introducing an *ortho* methyl group on the inhibitor B-ring resulted in a 430-fold increase in binding affinity. To understand the role of this methyl group, and design more potent inhibitors, analogs with various *ortho* groups on the B-ring were synthesized and evaluated. Enzyme inhibition was found to be highly sensitive to the size of the B-ring substituent, with electron withdrawing groups resulting in the highest binding affinity. Analogues with two B-ring substituents were also synthesized, but none resulted in improved inhibition, presumably due to steric hindrance. Pyridyl and pyrimidinyl B-rings were also incorporated, which led to an improvement in antimicrobial activity (MIC = 0.4 $\mu\text{g}/\text{mL}$).

The diaryl ethers were found to have modest *in vivo* efficacy, likely limited by high lipophilicity and metabolic instability. Pyranones and 4-pyridones were used to replace the phenol A-ring, which led to low ClogP values (2-4) and increased metabolic stability. The top compound had comparable MIC values to the diaryl ethers and an AUC/MIC value that had increased 5 fold.

In order to reduce the number of rotatable bonds, cyclic groups were used to replace the flexible hexyl group on the A-ring. Amine and ether linkers between the cyclic groups and the A-ring resulted in lower lipophilicity without altering the binding affinity.

Drug-target residence time is important for *in vivo* drug efficacy. Progress curve analysis was used to identify diaryl ethers that were time dependent inhibitors of InhA. Together with X-ray crystallography, MD simulations, and direct measurements of inhibitor dissociation, the residence time of the compounds on InhA were correlated with the energy changes during dissociation. These data support the importance of helix-6 and helix-7 motion in the time dependent inhibition of InhA, together with the observation that a steric clash between residues V203 and I215 is particularly important for modulating the energy of the transition state leading to the final enzyme-inhibitor complex. Significantly, replacement of V203 or I215 with Ala resulted in the loss of slow-onset inhibition by **PT070**. However, slow-onset inhibition was regained with PT162 and **PT163**, which place bulky groups between the mutated residues, thus compensating for the decrease in side chain bulk. These studies support the importance of interactions between helix-6 and 7, and suggest ways in which residence time can be rationally modulated.

Dedication

Pan Pan dedicates this dissertation to his parents

Pan Hua & Yu Jinying

for their precious love, understanding, and support.

Table of Contents

List of Figures.....	xi
List of Tables.....	xiv
List of Schemes.....	xvi
List of Abbreviations.....	xvii
Chapter 1. Introduction of Tuberculosis and Development of InhA Inhibitors as Potential Antitubercular Drugs.....	1
An Overview of Tuberculosis (TB)	2
<i>The History of TB</i>	2
<i>Pathology of M. Tuberculosis</i>	3
<i>Challenges in TB Control</i>	5
Current Diagnosis, Prevention, and Treatment of TB	6
Mechanisms of Antitubercular Drugs	11
<i>Inhibition of Fatty Acid Biosynthesis</i>	11
<i>Inhibition of Arabinogalactan and Peptidoglycan Biosynthesis</i>	12
<i>Inhibition of Protein Synthesis</i>	13
<i>Inhibition of DNA Replication and Transcription</i>	14
The Type II Fatty Acid Biosynthesis Pathway (FASII) in <i>M. tuberculosis</i>	15
Direct Inhibition of InhA.....	21

Slow-onset Inhibition of InhA.....	24
Research Project Overview.....	27
Chapter 2. Modifications on the A-Ring of the Diaryl Ethers that Target InhA.....	29
Background.....	30
<i>InhA in Fatty Acid Biosynthesis</i>	30
<i>Diaryl Ethers as InhA Inhibitors</i>	31
<i>Modifications to the A-Ring Substituents</i>	37
Synthesis Strategies for the Diaryl Ethers with A-Ring Substituents.....	39
Results and Discussion.....	44
<i>Van Der Waals Space for A-Ring Substituents</i>	44
<i>The Diaryl Ethers with Amine and Ether Substituted A-rings</i>	46
Summary.....	49
Experimental Section	50
<i>Measurement of IC₅₀ Values</i>	50
<i>Organic Synthesis</i>	52
Chapter 3. SAR Studies Focused on the B-Ring of the Diaryl Ethers that Target InhA. 66	
Background.....	67
<i>The Lipinski's Rules</i>	67

<i>Design of B-ring Modifications</i>	70
Synthesis Strategies for B-ring Modified Diaryl Ethers.....	74
Results and Discussion.....	78
<i>Analogs with Mono B-ring Substituents</i>	78
<i>Analogs with di-Substituted B-rings</i>	82
<i>Analogs with Heterocyclic B-rings</i>	85
<i>Activities against Nonreplicating M. tuberculosis.</i>	90
<i>General Binding Model for InhA</i>	92
Summary.....	95
Organic Synthesis.....	96
Enzyme Activity Assays	107
<i>Preparation of trans-2-Dodecenoyl-CoA (DD-CoA)</i>	108
<i>Measurement of K_i Values</i>	110
 Chapter 4. Synthesis, Activity, and Drug-like Properties of 4-Pyranone and 4-Pyridone Inhibitors.....	 112
Background.....	113
<i>Pharmacokinetics in Drug Development</i>	113
<i>4-Pyranones and 4-Pyridones as Important Pharmacophores</i>	116
<i>Design of InhA Inhibitors with 4-Pyranone and 4-Pyridone A-Rings</i>	122

Synthetic Strategies for the 4-Pyranones and 4-Pyridones.....	124
Results and discussion	128
<i>SAR of 4-Pyranone Inhibitors</i>	128
<i>SAR of 4-Pyridone Inhibitors</i>	130
<i>Cofactor Preference for 4-Pyridone Binding to InhA</i>	136
<i>Pharmacokinetics</i>	139
Summary.....	141
Experimental Section	143
<i>Enzyme Activity Assays</i>	143
<i>Thermofluor</i>	143
<i>Organic Synthesis</i>	143
Chapter 5. Mechanism of Slow-Onset Inhibition of InhA.	156
Background.....	157
<i>On-Target Residence Times: Missing Criteria in Drug Development</i>	157
<i>Slow-Onset Inhibition</i>	159
<i>Residence Times and In Vivo Efficacy</i>	160
<i>Mechanisms of Slow-onset Inhibition</i>	162
Materials and Methods.....	165
<i>Expression and Purification of InhA</i>	165

<i>Site-Directed Mutagenesis, Expression and Purification of InhA Mutants.</i>	166
<i>Measurement of K_i Values</i>	167
<i>Progress Curve Analysis</i>	167
<i>Rapid Dilution Experiments</i>	168
<i>Organic Synthesis</i>	169
Results and Discussion.....	170
<i>The Energy Barrier in the Transition State</i>	170
<i>The Loop Motion Mechanism of Slow-onset Inhibition</i>	178
<i>Identification of Tight Binding Slow-Off Inhibitors</i>	180
<i>In Vivo Efficacy of Slow-onset Diaryl Ethers</i>	184
Summary.....	187
Conclusions and Future Work	189
SAR on the A-Ring of the Diaryl Ethers	189
SAR on the B-Ring of the Diaryl Ethers	190
SAR of the Pyranones and Pyridones.....	191
Mechanisms of Slow-Onset Inhibition of InhA.....	192
References.....	194

List of Figures

Figure 1.1. The life cycle of <i>M. tuberculosis</i>	4
Figure 1.2. First-line antitubercular drugs.....	9
Figure 1.3. Mycolic acids in the outer layer of the cell wall.....	15
Figure 1.4. Fatty acid biosynthesis in <i>M. tuberculosis</i>	16
Figure 1.5. Activation of isoniazid by KatG.....	17
Figure 1.6. The benzoylhydrazine-NAD adduct (BH-NAD).....	17
Figure 1.7. The X-ray structure of thienodiazaborine bound to ecFabI.	19
Figure 1.8. Scaffolds of Other InhA inhibitors.....	23
Figure 1.9. The two step mechanism for slow-onset enzyme inhibition.....	24
Figure 1.10. Structures of ecFabI in the absence and presence of triclosan.....	25
Figure 1.11. The structure of PT070.....	26
Figure 2.1. The reduction reaction of FASII, catalyzed by InhA.	30
Figure 2.2. Interactions between PT005 and residues in the active site.....	33
Figure 2.3. Compound 20 bound to InhA.	37
Figure 2.4. Designs of A-ring substituents.....	38
Figure 2.5. PT070 and compound 20 bound to the active site of InhA.....	46
Figure 2.6. The semilog concentration-response plot of PT144 titration.	51
Figure 3.1. The InhA inhibitor PT004 and PT070.	68
Figure 3.2. Residues interacting with PT070.....	71
Figure 3.3. PT070 analogs with various groups on the B-ring.....	72
Figure 3.4. Diaryl ethers with heterocyclic B-rings.	72

Figure 3.5. A design of codrugs mimicking isoniazid and pyrazinamide.....	73
Figure 3.6. The correlation between MIC and K_i values.	81
Figure 3.7. PT091 and PT109 docked into the active site of InhA.....	84
Figure 3.8. Analysis of interactions around the B-ring of PT070.	88
Figure 3.9. MIC and K_i values of the pyridyl diaryl ethers.....	89
Figure 3.10. Structures of InhA inhibitors	92
Figure 3.11. Common binding mode for InhA inhibitors.	94
Figure 3.12. A two-step slow-onset mechanism.	111
Figure 4.1. Enzyme catalyzed reactions in Phase I metabolism.	114
Figure 4.2. Reactions in Phase II metabolism.....	115
Figure 4.3. Structures of the 4-pyranone, 4-pyridone, and phenol.	117
Figure 4.4. The 2-pyridone FabI inhibitor CG400549 [147].	121
Figure 4.5. The design of InhA inhibitors with 4-pyranone and 4-pyridone A-rings.	123
Figure 4.6. Comparison of the phenyl and pyridyl B-ring.....	133
Figure 4.7. PT070 and PT155 bound to InhA.....	134
Figure 4.8. The correlation between MIC and IC_{50} values.....	135
Figure 4.9. The dihedral angle τ_1 -1-6-5 in the cofactor $NAD^+/NADH$	137
Figure 4.10. Inhibitor binding changes the T_m of a protein. Taken from [151].	137
Figure 4.11. AUC and T above MIC.	139
Figure 5.1. The cost of pharmaceutical research.	157
Figure 5.2. Thermodynamic and kinetic parameters.	158
Figure 5.3. Rapid reversible and slow-onset inhibition.	159
Figure 5.4. Residence time and survival percentage are correlated.	161

Figure 5.5. The diaryl ethers PT004 and PT070.	163
Figure 5.6. The substrate binding loop in the active site.	163
Figure 5.7. X-ray crystallographic structures of PT070, PT092, and PT119 bound to InhA.....	173
Figure 5.8. A close view of Val203 and Ile215 in the active site.....	174
Figure 5.9. Schematic energy diagram of PT070 and PT119 binding to InhA.....	175
Figure 5.10. Interactions in the active sites of InhA bound to PT070 and PT119.	177
Figure 5.11. Schematic reaction coordinate for slow-off inhibitors.	181
Figure 5.12. The substrate binding loop in InhA complex with PT003 and PT005.	182
Figure 5.13. <i>In vivo</i> efficacy of PT070 and PT091.....	184
Figure 5.14. <i>In vivo</i> efficacy of PT091 (IP).	185

List of Tables

Table 1.1. Six classes of second-line antitubercular drugs.....	10
Table 1.2. INH-NAD Analogs	18
Table 1.3. Antitubercular activity of diazaborine derivatives.....	20
Table 1.4. SAR study of triclosan against InhA.	22
Table 2.1. Development of the diaryl ethers.....	32
Table 2.2. SAR of the A-ring of the diaryl ethers.	35
Table 2.3. The diaryl ethers with various A-ring substituents.	45
Table 2.4. A-ring substituents with ether and amine linkers.	47
Table 2.5. Initial velocities at various concentrations of PT144.....	51
Table 2.6. Contributors for synthesis of the diaryl ethers.	52
Table 3.1. B-ring modified diaryl ether inhibitors.	69
Table 3.2. Derivatives with <i>ortho</i> substituent groups on the B-ring.	79
Table 3.3. Derivatives with di-substituted B-ring.	83
Table 3.4. Docking results of PT091 and PT109 with InhA.	85
Table 2.5. Derivatives with heterocycle B-rings.....	87
Table 3.6. Activities of InhA inhibitors against nonreplicating <i>M. tuberculosis</i>	91
Table 3.7. Contributors for synthesis of the diaryl ethers.	96
Table 4.1. Pharmacokinetic parameters for PT004 in male C57/BL6 mice.	116
Table 4.2. Modifications on 1-N of 4-pyridone FabI inhibitors.	118
Table 4.3. Modifications on 3-C (the B-ring) of 4-pyridone derivatives.	120
Table 4.4. <i>In vitro</i> activities of the 4-pyranones.....	129

Table 4.5. <i>In vitro</i> activities of the 4-pyridones.	131
Table 4.6. 4-Pyridones derivatives with pyridyl B-rings.	132
Table 4.7. Thermofluor results of PT070 and PT166.....	138
Table 4.8. Pharmacokinetic parameters for InhA inhibitors.	140
Table 4.9. Contributors for synthesis of the 4-pyranones and the 4-pyridones.	144
Table 5.1. Examples of ligand-target complexes that have long residence times.	160
Table 5.2. Nucleotide primers for preparation of InhA mutants.	167
Table 5.3. Enzyme binding kinetics of the diaryl ethers.....	172
Table 5.4. Binding kinetics of the diaryl ethers to InhA and its mutants.....	179
Table 5.5. Slow-onset inhibitors with rapid binding steps.	183

List of Schemes

Scheme 2.1. Synthesis of compound PT089 and PT090.....	39
Scheme 2.2. Synthesis of the intermediate 46.....	40
Scheme 2.3. Synthesis of PT144 and PT158.....	40
Scheme 2.4. Derivatives with amine substituents on the A-ring.....	41
Scheme 2.5. Demethylation with BBr ₃	42
Scheme 2.6. Synthesis of the diaryl ethers with ether substituted A-rings.....	42
Scheme 3.1. The synthesis of PT095.....	74
Scheme 3.2. Synthesis of compound 60.....	75
Scheme 3.3. Synthesis of compound PT091, PT092, PT096, and PT119.....	75
Scheme 3.4. Synthesis of compound PT130.....	76
Scheme 3.5. Synthesis of (<i>E</i>)-methyl dodec-2-enoic acid (74).....	109
Scheme 4.1. An example of the synthesis of the first 4-pyranones and 4-pyridones. .	124
Scheme 4.2. Synthesis of the intermediate 122.....	125
Scheme 4.3. Synthesis of the 4-pyridones with phenyl B-rings.....	126
Scheme 4.4. Synthesis of the 4-pyridones with pyridyl B-rings.....	127

List of Abbreviations

AcOH	Acetic acid
ACP	Acyl carrier protein
BCG	Bacille Calmette-Guérin
BSA	Bovine serum albumin
<i>B. subtilis</i>	<i>Bacillus subtilis</i>
calcd	Calculated
CFU	Colony-forming unit
ClogP	Calculated logarithm of partition coefficient between
CoA	Coenzyme A
DD-CoA	<i>Trans</i> -2-Dodecenoyl-CoA
DMF	dimethylformaide
DMSO	Dimethyl sulfoxide
DNA	Deoxyribonucleic acid
<i>E. coli</i>	<i>Escherichia coli</i>
ecFabI	Enoyl-ACP reductase from <i>Escherichia coli</i>
ESI	Electrospray ionization
EtOH	Ethanol
<i>F. tularensis</i>	<i>Francisella tularensis</i>
FabI	Enoyl-ACP reductase
FabK	Enoyl-ACP reductase
FAS-I	Eukaryotic fatty acid biosynthesis
FAS-II	Bacterial fatty acid biosynthesis

ftuACP	ACP from <i>F. tularensis</i>
HCl	Hydrochloric acid
HIV	Human immunodeficiency virus
HPLC	High-performance liquid chromatography
HRMS	High-resolution mass spectroscopy
HTS	High-throughput screening
IC ₅₀	The half maximal inhibitory concentration
InhA	Enoyl-ACP reductase from <i>Mycobacterium tuberculosis</i>
KatG	Mycobacterial catalase-peroxidase
KOH	Potassium hydroxide
LB	Luria Broth
logP	Logarithm of partition coefficient between <i>n</i> -octanol and water
LORA	Low oxygen recovery assay
<i>M. tuberculosis</i>	<i>Mycobacterium tuberculosis</i>
MDR-TB	Multidrug-resistant TB
MeOH	Methanol
MHz	Megahertz
MIC	Minimal Inhibitory Concentration
MRSA	Methicillin-resistant <i>Staphylococcus aureus</i>
MS	Mass spectrum
NAC	<i>N</i> -Acetylcysteamine
NAD ⁺	Nicotinamide adenine dinucleotide (oxidized form)
NADH	Nicotinamide adenine dinucleotide (reduced form)
NaOH	Sodium hydroxide

NMR	Nuclear magnetic resonance
O.D. 600	Optical density at 600 nm
PCR	Polymerase chain reaction
pdb	Protein data bank
PIPES	Piperazine-N,N'-bis(2-ethanesulfonic acid)
rt	Room temperature
<i>S. aureus</i>	<i>Staphylococcus aureus</i>
saFabI	Enoyl-ACP reductase from <i>S. aureus</i>
SAR	Structure-activity relationship
sat.	Saturated
SDS-PAGE	Sodium dodecyl sulfate polyacrylamide gel electrophoresis
TB	Tuberculosis
THF	Tetrahydrofuran
WHO	World Health Organization
wt	Wild type
XDR-TB	Extensively drug-resistant tuberculosis

Acknowledgments

Foremost, I would like to express my gratefully and sincerely gratitude to my advisor Prof. Peter J. Tonge for the continuous support of my Ph.D. education, study, and research; for his patience, motivation, enthusiasm, and encouragement; and for his guidance that helped me in all the time of research and writing of this thesis. I could not have imagined finishing my Ph.D. study without him.

Besides, I would like to thank Prof. Francis Johnson, the chairperson of my dissertation committee, for his valuable suggestions and knowledgeable comments in guiding my research. I am grateful to Prof. David F. Green, the third member of my dissertation committee, for all his kind help and insightful advice. It is a pleasure to thank Prof. Stephen G. Walker, the outside member of my committee, for his support and encouragement.

I would like to thank all the current members and some alumni of Tonge group for your stimulating discussion, generous help, and warm friendship. All my friends in Stony Brook have brightened my years in the graduate school.

Finally, I owe my deepest gratitude to my parents, for giving birth to me at the first place, and for their support and love that carry me through all the hard and happy moments so far.

Chapter 1. Introduction of Tuberculosis and Development of InhA Inhibitors as Potential Antitubercular Drugs.

Tuberculosis (TB) is a common and often deadly contagious disease, which is becoming a global threat to human health due to the emergence of multidrug-resistant (MDR-TB) and extensively drug-resistant (XDR-TB) strains of *Mycobacterium tuberculosis* [1, 2]. According to reports from the World Health Organization (WHO), there were 8.8 million cases of TB in 2010 [3], which killed more people than any other infectious disease [1]. In addition, TB is the leading cause of death among people with HIV. For these reasons, the development of novel, efficient chemotherapy is an urgent need. In this chapter, a brief overview of TB, current treatments of the disease, and development of antitubercular drugs are summarized.

An Overview of Tuberculosis (TB)

The History of TB

The history of TB can be traced back to 20,000 years ago, and its pathogen *Mycobacterium tuberculosis* (*M. tuberculosis*) is thought to have co-evolved with humans [1]. There were many fallacies about TB, which was initially known as “consumption” or “the white plague”, because of its mystery and the fact that no helpful treatment was available except for sanatoria [4]. At one stage, it was even believed that TB could be inherited. Not until 1882 was *M. tuberculosis* discovered by Dr. Robert Koch, as the pathogen of TB, using methylene blue and Bismarck brown staining [5]. This method was later developed into the well-known Ziehl-Neelsen staining [6]. Due to the high lipid and mycolic acid content in its cell wall, *M. tuberculosis* does not give typical Gram staining results, and therefore is classified as an acid-fast bacterium [7].

M. tuberculosis is an aerobic rod-shaped bacillus that divides at an extremely slow rate of every 20-24 hours per generation [8, 9]. Although *M. tuberculosis* is the predominant pathogen of human TB, other mycobacteria such as *Mycobacterium bovis*, *Mycobacterium africanum*, *Mycobacterium canetti*, and *Mycobacterium microti* can also cause mycobacterial infections, but these species are less common.

Pathology of M. Tuberculosis

TB is spread from person to person almost exclusively by small-particle aerosols with diameters of 1-5 μm that may contain 1-10 tubercle bacilli. The minimum infectious dose ranges from one single bacterium upward [10]. After being inhaled into the alveolar space, the infectious bacilli are deposited and begin to replicate. The bacilli will colonize the walls of pulmonary cavities, where they are believed to be phagocytosed by alveolar macrophages.

M. tuberculosis is a facultative, intracellular bacterial pathogen that survives and multiplies within phagosomes. It arrests maturation of phagosomes and resists acidification [11]. While in macrophages, the bacteria induce localized inflammatory response, which leads to recruitment of mononuclear cells, providing fresh host cells for expanding bacterial population and finally assembling the granuloma. The continuous immune response attracts lymphocytes and foamy macrophages, builds a more organized structure, and vascularizes the granuloma [10]. In a more mature granuloma, the fibrous sheath becomes more marked, which reduces the number of blood vessels penetrating the structure, and more foamy macrophages are present. These changes result in the formation of caseous debris in the center of the granuloma. Finally, infectious bacilli are released into the airways when the granuloma cavitates and collapses into the lungs [12] (**Figure 1.1**).

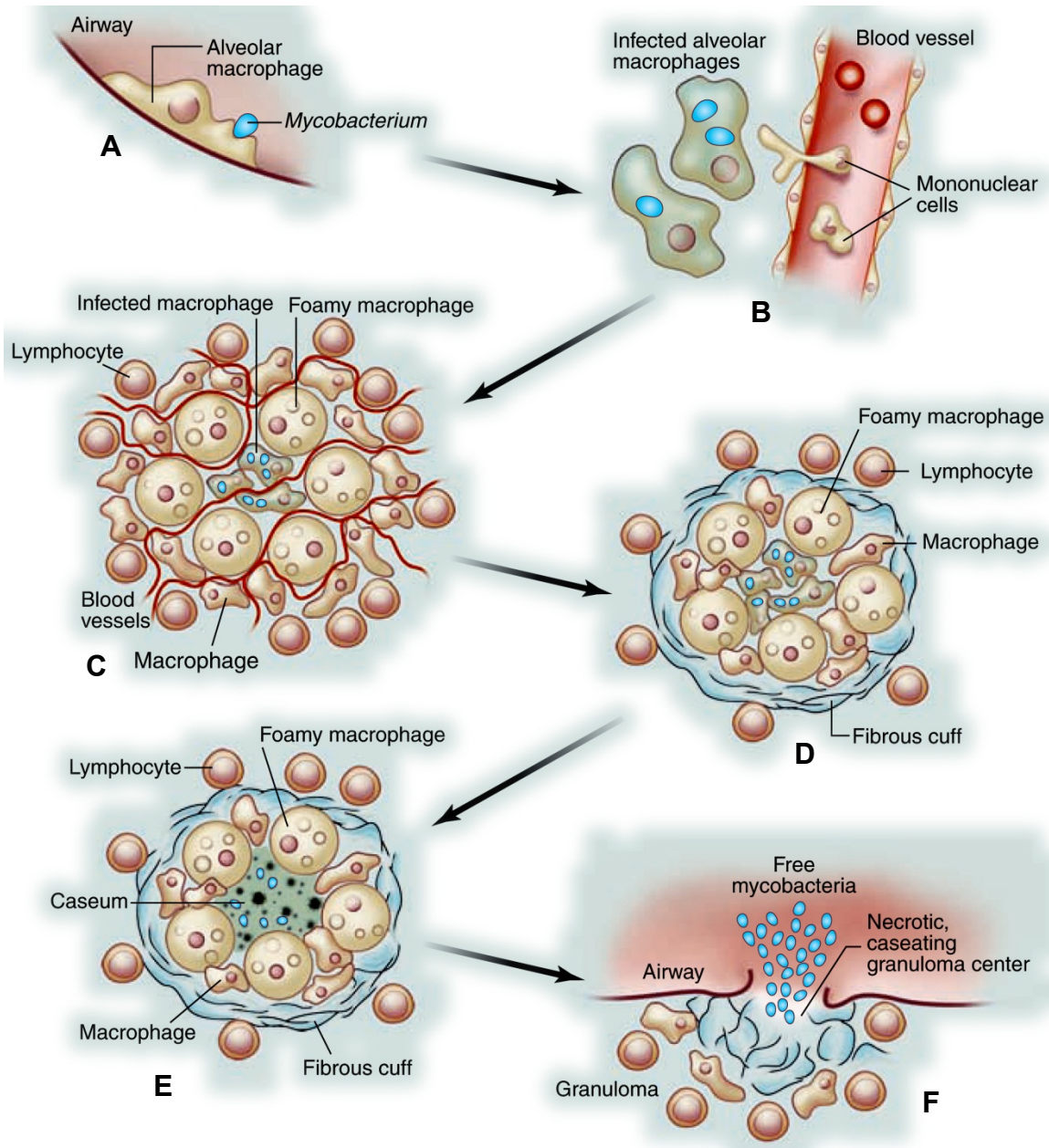


Figure 1.1. The life cycle of *M. tuberculosis*.

Taken from [10]. **A.** The infection is initiated when *M. tuberculosis* bacilli are inhaled and phagocytosed by alveolar macrophages. **B.** The inflammatory response leads to the recruitment of monocytes and extensive neovascularization. **C.** The granuloma forms when macrophages differentiate to epithelioid cells, multinucleate giant cells, and foam cells. **D.** The granuloma becomes further stratified by the formation of a fibrous cuff. **E.** Caseum accumulates in the granuloma center. **F.** Infectious bacilli are released into the airways.

M. tuberculosis survives and duplicates slowly in macrophages, which makes TB difficult to cure. In fact, there is some evidence that the human immune system may be necessary for TB infection [13]. About 90% of *M. tuberculosis* infected people have asymptomatic, latent TB infection, with only a 10% chance that the latent infection will progress to TB disease [14, 15].

Challenges in TB Control

Currently, three major challenges limit our ability to effectively eradicate TB: drug resistance, HIV-coinfection, and regimen non-compliance.

Multi-drug-resistant tuberculosis (MDR-TB) is defined as tuberculosis that is resistant to at least isoniazid and rifampicin [16]. MDR-TB that is resistant to any member of the quinolone family and at least one of the following second-line antitubercular injectable drugs: kanamycin, capreomycin, or amikacin, is defined as extensively drug-resistant tuberculosis (XDR-TB) [15, 17]. It was reported by the WHO that 22% of new tuberculosis cases were MDR-TB in 2008 [18]. There are an estimated 25,000 cases of XDR-TB emerging every year [19], and by the end of 2010, 69 countries have reported at least one case of XDR-TB. These forms of TB do not respond to the standard six month treatment and can take two years or more to treat with drugs that are less potent, more toxic, and much more expensive [19].

In 2010, there were 1.1 million deaths from TB among HIV-negative people and an additional 0.35 million deaths from HIV-associated TB [3, 20]. By now, TB is the leading cause of death among people living with HIV; almost one in four deaths among people with HIV is due to TB [20].

Typical tuberculosis chemotherapy involves the use of several first-line and second-line antitubercular drugs over a period of at least six months. The regimen is tedious and difficult to maintain. Non-compliance of the treatment often results in TB recurrence and serious drug resistance [15, 21, 22].

Current Diagnosis, Prevention, and Treatment of TB

A quick, preliminary diagnosis of TB is based on the medical history and symptoms of a patient. The result is fairly inaccurate and, in most circumstances, requires further diagnosis. A physical examination is a direct method to evaluate the overall condition of disease development in a patient, which will provide information for further diagnosis. Although a physical examination cannot confirm or exclude TB infection, it is still an essential part of the diagnosis. Further diagnosis includes *M. tuberculosis* infection tests, chest radiographs, and bacteriologic examinations.

In the US, two methods are currently available for detection of *M. tuberculosis*: the Mantoux tuberculin skin test (TST) and interferon- γ release assays (IGRAs), which help to identify TB or latent TB in infected people. However, a negative result does not exclude the diagnosis of TB or latent TB [23]. With pulmonary TB

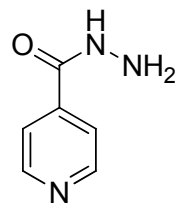
being the most common form of the disease, the chest radiograph is useful for diagnosis of TB. In some instances, a computerized tomography (CT) scan may provide additional information, for instance, more detailed images of parts of the body that cannot easily be seen on a standard chest radiograph. Chest radiographs may be used to exclude pulmonary TB disease in an HIV-negative person, while a bacteriological examination gives direct evidence of *M. tuberculosis* infection. In practice, the bacteriological examination includes specimen collection, acid-fast bacilli (AFB) smear classification, nucleic acid amplification (NAA), specimen culturing, and drug-susceptibility tests. This method is the most reliable diagnosis method, giving the most detailed information about *M. tuberculosis* strains from the specimen, as well as epidemiologic records of TB transmission. Unfortunately, its application is limited due to laboratory conditions, time lines, and cost consideration [24].

Vaccination is considered to be the long-term solution for TB [25]. So far, the only available vaccine for TB is the bacille Calmette-Guérin (BCG). The BCG vaccine is an attenuated vaccine derived from a strain of *Mycobacterium bovis* that was developed over several years by Calmette and Guérin at the Pasteur Institute in Lille, France. An early version of BCG was first administered to humans in 1921. Since then, many different strains have been derived and used throughout the world. Many highly TB-prevalent countries vaccinate infants with BCG as part of their TB control effort to prevent children from contacting severe disseminated TB or TB meningitis. However, the efficacy of BCG has been

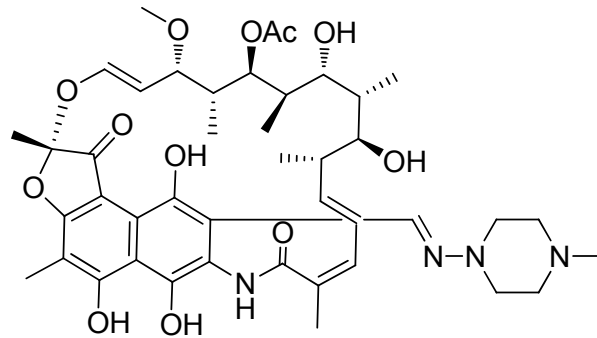
questioned as very limited protection was reported in some countries [26]. Moreover, the vaccination interferes with the ability to determine TST reactivity. For these two reasons, BCG vaccination is not generally recommended in the US [23].

TB treatment is a difficult, long-term task that needs constant adjustment according to the bacteria strain, disease progress, and physiological condition of the patient. The lack of treatment observance seems to be the main reason of occurrence and spread of MDR-TB [27], which highlights the importance of the directly observed therapy short course (DOTS).

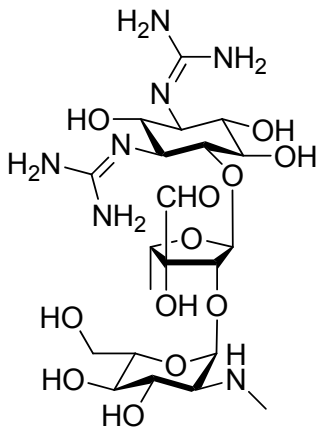
Currently, there are five first-line antitubercular drugs available for TB chemotherapy: isoniazid, rifampicin, pyrazinamide, streptomycin, and ethambutol (**Figure 1.2**). Second-line antitubercular drugs are less commonly used due to poor efficacy or side effects; they can be divided into six classes of antibiotics (**Table 1.1**). For new TB cases, standard chemotherapy is two months of isoniazid, rifampicin, pyrazinamide, and ethambutol, followed by four months of isoniazid and rifampicin or ethambutol [28]. A treatment guideline for MDR or XDR-TB has not been well established yet. Generally, it is suggested that at least five drugs should be chosen from first and second-line antitubercular drugs that are still active to MDR-TB strains [29]. The regimen for HIV co-infected TB is even more complicated due to interference with antiviral therapy, and more studies are needed to determine the proper drug combinations.



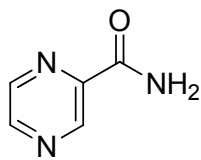
Isoniazid



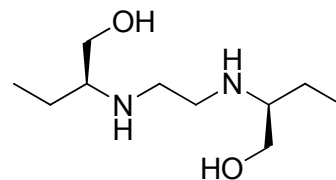
Rifampicin



Streptomycin



Pyrazinamide

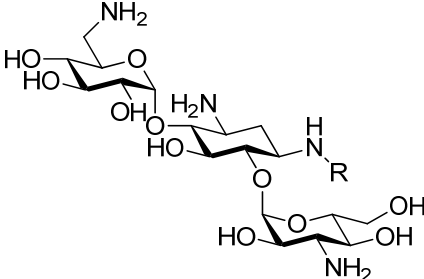
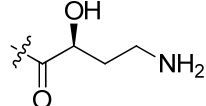
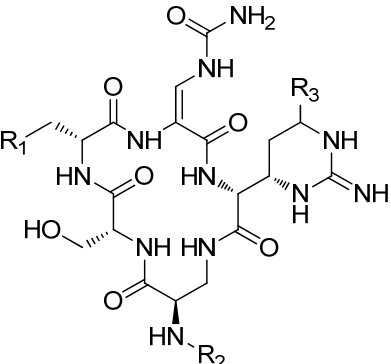
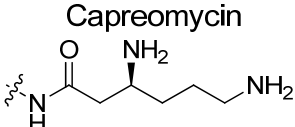
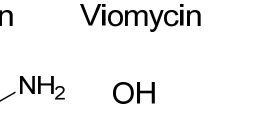
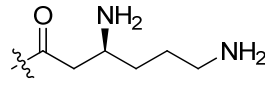
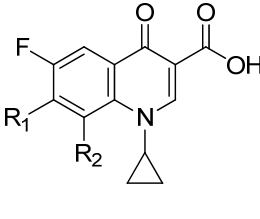
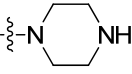
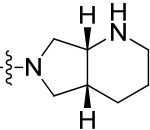
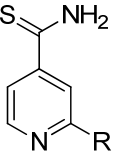
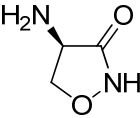
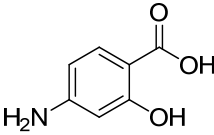


Ethambutol

Figure 1.2. First-line antitubercular drugs.

The structures of first-line antitubercular drugs isoniazid, rifampicin, streptomycin, pyrazinamide, and ethambutol.

Table 1.1. Six classes of second-line antitubercular drugs.

Drug class	Examples
Aminoglycosides	 <p>Amikacin (AK) R = </p> <p>Kanamycin (KM) R = H</p>
Polypeptides	 <p>Capreomycin R₁ =  Viomycin R₁ = </p> <p>R₂ = H R₂ = </p> <p>R₃ = H R₃ = OH</p>
Fluoroquinolones	 <p>Ciprofloxacin (CIP) R₁ = H R₂ = </p> <p>Moxifloxacin (MXF) R₁ = OMe R₂ = </p>
Thioamides	 <p>Ethionamide R = CH₂CH₃</p> <p>Prothionamide R = CH₂CH₂CH₃</p>
Cycloserine	
<i>p</i> -Aminosalicylic acid (PAS)	

Mechanisms of Antitubercular Drugs

Mechanisms of major antitubercular drugs are summarized below, which include inhibition of fatty acid biosynthesis, peptidoglycan biosynthesis, protein synthesis, and DNA replication and expression. Some targets of antitubercular drugs are still unclear and need to be identified [30, 31]. The determination of current drug mechanisms and discovery of new targets are important and will lead to the development of new antitubercular drugs.

Inhibition of Fatty Acid Biosynthesis

Isoniazid blocks the type II fatty acid biosynthesis pathway (FASII) by inhibiting the InhA enzyme, and its mechanism will be discussed in detail in following sections. Similar to isoniazid, ethionamide, prothionamide, and thiacetazone can be transformed into highly reactive species by mycobacterial enzyme EthA; these reactive intermediates will react with any nucleophile. It was reported that thiacetazone forms an adduct with glutathione [32]. Ethionamide also forms new adducts [33], although the structures have not been identified. These adducts are likely to inhibit InhA, as resistance to ethionamide is related to a mutation on *inhA* gene for some *M. tuberculosis* strains [34].

Pyrazinamide has become a very important drug against TB since 1985, but the mode of action is still under debate. Some evidence suggests that

pyrazinamide is taken into cells as a prodrug, and it is then hydrolyzed to pyrazinoic acid by pyrazinamidase [35], which will inhibit the type I fatty acid biosynthesis pathway (FASI) [36]. Another possible result of releasing pyrazinoic acid is disturbed charge equilibrium across cell membranes, which leads to irreversible acidification and kills even persistent cells [37]. Recently, Zhang *et al.* found that pyrazinoic acid also kills persistent *M. tuberculosis* by binding to the ribosomal protein S1 and subsequently inhibiting trans-translation, a process involved in rescuing ribosomes that have stalled while decoding mRNA [38].

Inhibition of Arabinogalactan and Peptidoglycan Biosynthesis

One of the reasons that *M. tuberculosis* is difficult to eradicate is the special structure of its cell wall. The outer membrane of *M. tuberculosis* consists of peptidoglycan, arabinogalactan, and mycolic acids. Peptidoglycan is a polymer formed with amino acids and saccharides, supporting the cell wall structure and protecting cells from exogenous toxins. Arabinogalactan, a layer of polysaccharides made of arabinose and galactose, connects the peptidoglycan and mycolic acids. Inhibition of the biosynthesis of arabinogalactan or peptidoglycan destroys the basic cell wall structure and kills *M. tuberculosis*.

Researchers found that ethambutol interferes with the arabinan biosynthesis [39, 40], although the mechanism is not clear. In addition, it also changes levels of other metabolites in the outer membrane, suggesting that there are multiple

targets [41]. The second-line drug D-cycloserine was found to inhibit D-alanine racemase [42] and D-alanine–D-alanine ligase [43], which are necessary for the synthesis of UDP-muramyl-pentapeptide, a building block of peptidoglycan. As a member of β -lactam antibiotics, amoxicillin inhibits the transpeptidase that cross-links the peptide side chains, and thus stops the biosynthesis of peptidoglycan [44]. Similar to other riminophenazines, clofazimine changes the outer membrane of *M. tuberculosis*, which is consistent with a previously identified “generalized membrane-disrupting effect” [45]. However, the mechanism still needs to be clarified.

Inhibition of Protein Synthesis

Aminoglycosides, including streptomycin, kanamycin, and amikacin, target the 30S subunit of ribosome and lead to mistranslation of mRNA [46]. Sharing the same mechanism, cyclic peptide antibiotics capreomycin and viomycin cause cross resistance to aminoglycosides in *M. tuberculosis* [47]. Contrary to aminoglycosides, macrolides stop protein expression by binding to the 50S subunit of ribosome [48]. Other antibiotics that show inhibitory activity against *M. tuberculosis* by inhibiting the 50S subunit include linezolid, a fully synthetic antimicrobial [49]; pleoromutilin antibiotics [50], including tiamulin and valdemulin; and nocathiacins [51], a class of thiazole-containing peptides.

Inhibition of DNA Replication and Transcription

Rifamycins are a group of natural or semi-synthetic antibiotics. They are highly effective against *M. tuberculosis* with a unique mechanism—binding to the β -subunit of the DNA-dependent RNA polymerase [52]. Various derivatives were developed to improve pharmacokinetics, including rifapentin and rifametane [53]. Fluoroquinolones are a large family of synthetic antibiotics. They target the ATP-dependent DNA gyrase (topoisomerase II) and the ATP-dependent topoisomerase IV to inhibit the growth of *M. tuberculosis* [54]. So far, four generations of fluoroquinones were developed to reduce side effects and improve activity and pharmacokinetics.

Other mechanisms of antitubercular drugs include inhibition of dihydrofolate reductase, siderophore biosynthesis [55], FtsZ protein [56], and menaquinone biosynthesis [57, 58]. Notably, even though mechanisms of all the first and second-line drugs are discussed here, some of them are still not clear, and more information is required to determine the mode of action [59].

The Type II Fatty Acid Biosynthesis Pathway (FASII) in *M. tuberculosis*

The outer layer of the mycobacterial cell wall is comprised predominantly of mycolic acids (**Figure 1.3**), very long chain (C_{60} - C_{90}) fatty acids that are important for the ability of *M. tuberculosis* to live and replicate inside macrophages, and also for the inability of many antibiotics to penetrate into the cytosol [60, 61].

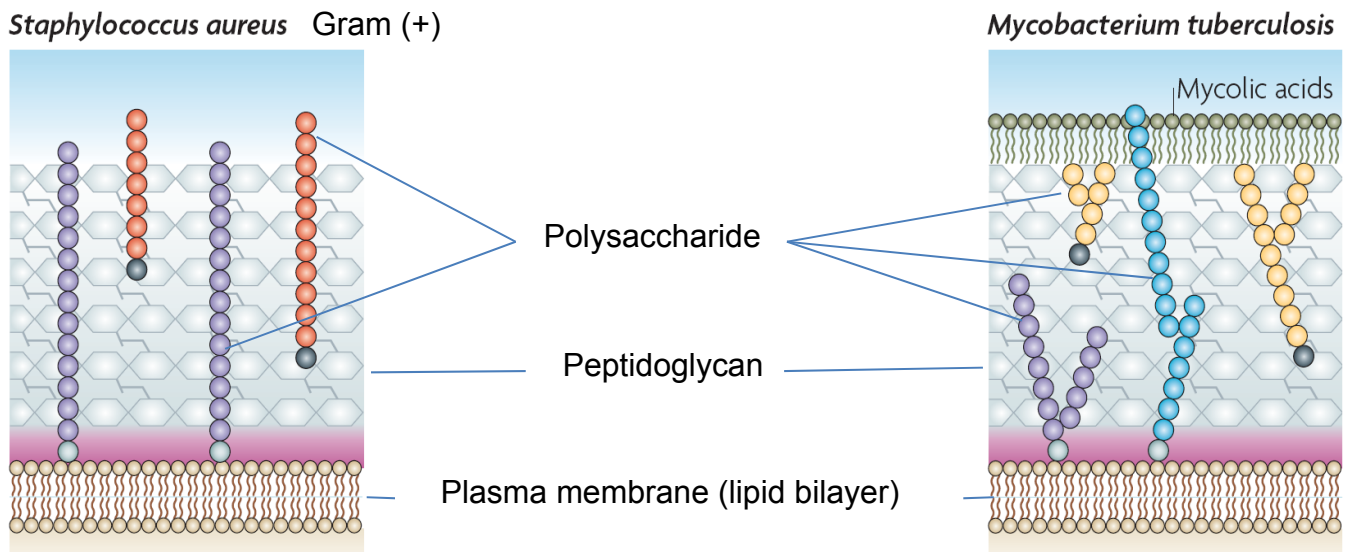


Figure 1.3. Mycolic acids in the outer layer of the cell wall.

Cell wall structures of *S. aureus* and *M. tuberculosis*, including the plasma membrane, peptidoglycan, and polysaccharide. Taken from [62].

The fatty acid precursors required for mycolic acid biosynthesis are generated by the mycobacterial type I (FASI) and type II (FASII) biosynthetic pathways (**Figure 1.4**). The FASI enzyme complex, which is homologous to the synthase found in mammalian cells, catalyzes the *de novo* synthesis of C_{20} - C_{24} fatty acyl-

CoAs from acetyl-CoA and malonyl-CoA. In the FASII pathway, chain elongation utilizes malonyl-ACP generated from malonyl-CoA by FabD, the malonyl-CoA:ACP transacylase. Entry of fatty acids into the FASII pathway is mediated by the β -ketoacyl-ACP synthase FabH, which condenses the acyl-CoA with malonyl-ACP. The resulting β -ketoacyl-ACP is reduced by the NADPH-dependent reductase MabA, dehydrated by an unidentified enzyme, and reduced by the NADH-dependent enoyl-ACP reductase InhA. Thereafter, subsequent rounds of elongation are primed by the β -ketoacyl-ACP synthases KasA and KasB. The resulting fatty acids from the FASII system are up to C₅₆ in length.

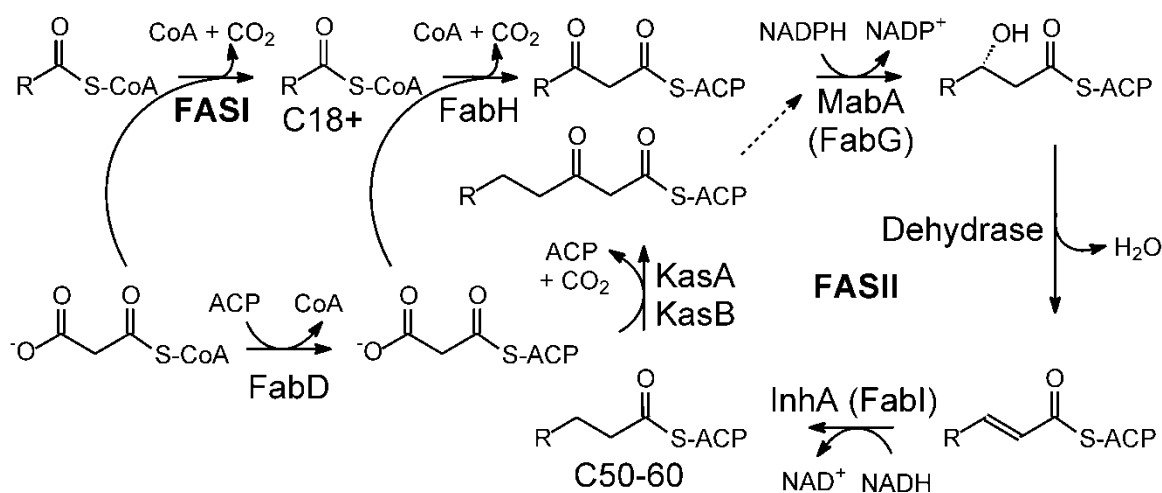


Figure 1.4. Fatty acid biosynthesis in *M. tuberculosis*.

InhA, also known as FabI in other organisms, plays an essential role in cell viability and is a target for the TB drug isoniazid [63-68], as Jacobs and coworkers have demonstrated that inactivation of InhA in *M. smegmatis* results in cell lysis [69]. The action of isoniazid depends on the activity of the mycobacterial catalase-peroxidase KatG [70], which catalyzes the addition reaction of isoniazid

and NAD(H) when the drug enters *M. tuberculosis* cells (**Figure 1.5**). The 4S isomer (**3**) of the adduct is a sub-nanomolar slow-onset inhibitor of InhA [68].

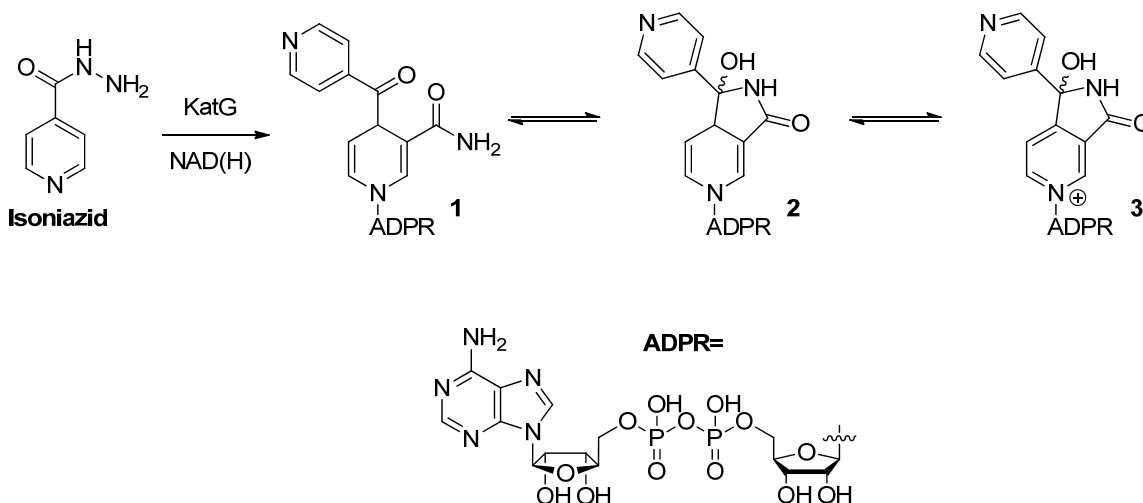


Figure 1.5. Activation of isoniazid by KatG.

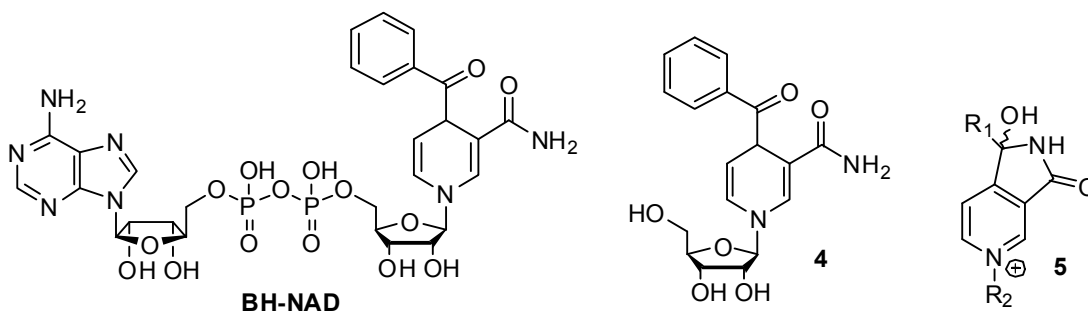
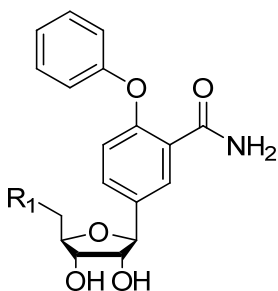


Figure 1.6. The benzoylhydrazone-NAD adduct (BH-NAD).

In order to explore SAR involving the INH-NAD inhibitor, the benzoylhydrazone-NAD adduct (**BH-NAD**) and its analogs have been synthesized (**Figure 1.6**) [71]. **BH-NAD** competitively inhibits InhA with a K_i value < 1 nM [68],

but preliminary studies also showed that benzoic hydrazide is less readily activated than isoniazid.

Table 1.2. INH-NAD Analogs



Compound	R ₁	IC ₅₀ (μM)
6	-OH	>100
7	-OPO(OH) ₂	>100
8	-ADP	27

A series of 4-phenoxybenzamides have also been prepared in order to mimic key elements of the INH-NAD adduct (**Table 1.2**) [72]. However, as seen for the **BH-NAD** analogues, none of these analogues significantly affected InhA activity, indicating the importance of the nucleotide for InhA inhibition.

Diazaborines are another class of compounds that inhibit FabI enzymes by covalently interacting with the NAD cofactor. A diazaborine was first identified in 1981 as a novel inhibitor of lipopolysaccharide biosynthesis [73]. The mechanism of enzyme inhibition with specific focus on *Escherichia coli* FabI (ecFabI) has been studied in detail using X-ray crystallography and site-directed mutagenesis

[74-78]. The compounds form adducts with the cofactor through a bond between the NAD^+ 2'-ribose hydroxyl group and the diazaborine boron atom (**Figure 1.7**). Thus, in this respect they mirror the mechanism of action of isoniazid, although the diazaborines are not prodrugs.

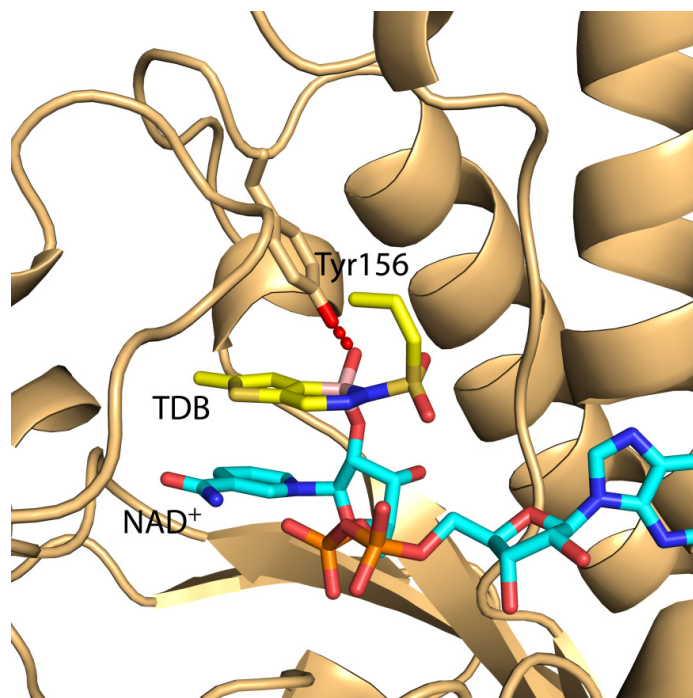


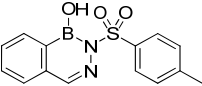
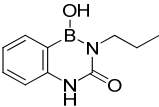
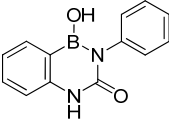
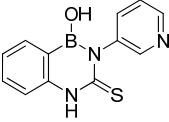
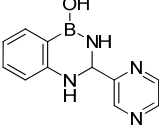
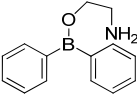
Figure 1.7. The X-ray structure of thienodiazaborine bound to ecFabI.

The X-ray structure of thienodiazaborine (TDB, yellow) bound to ecFabI, with NAD^+ (blue) as the cofactor [74]. The figure was made with PyMol [79].

Davis *et al.* synthesized six compounds and determined their MIC values using two different types of media, representing two different populations in TB infection (**Table 1.3**) [80]. In general the antibacterial activity of the compounds was modest, with the best MIC being 8 $\mu\text{g/ml}$. Comparison of **10** with **11** and **12** indicates that large substituents are preferred on N-2, together with a carbonyl

(C=O or C=S) at C-3 (**11**, **12**, **13**). Bioisosteres **11** and **12** have the same potency, while a typical benzodiazaborine **9** has moderate antibacterial activity. Surprisingly, the ring-opened amine **14** has similar activity to that of **9**.

Table 1.3. Antitubercular activity of diazaborine derivatives.

Compound	Structure	MIC ($\mu\text{g/ml}$)
Isoniazid		0.02
Pyrazinamide	Figure 1.2	197
9		$12^a/96^b$
10		$>128^a/>128^b$
11		$8^a/16^b$
12		$8^a/16^b$
13		$>128^a/128^b$
14		$16^a/64^b$

^a MIC was measured in Bactec 6A media.
^b MIC was measured in Bactec 12B media.

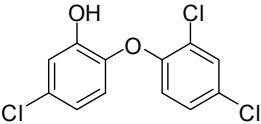
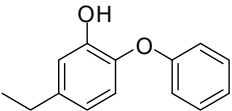
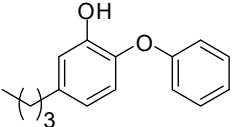
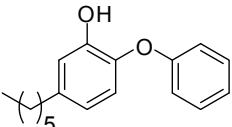
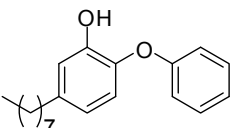
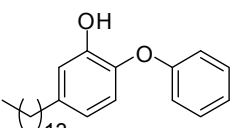
Although isoniazid is a potent InhA inhibitor, drug resistance arose from the long history of its clinical utilization and limits its applications. Importantly, because the primary mechanism of resistance to isoniazid occurs from mutations in KatG and not from mutations in InhA [70, 81-84], inhibitors of InhA that do not require KatG activation should be active against the majority of isoniazid-resistant *M. tuberculosis* strains [85].

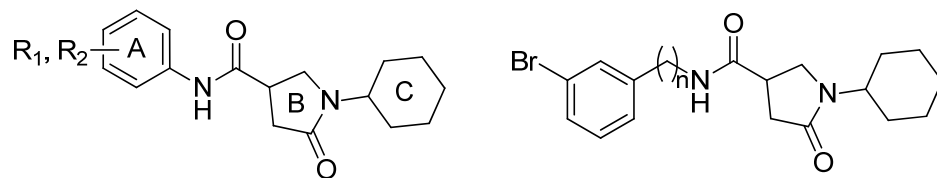
Direct Inhibition of InhA

Previously, our group reported diaryl ethers as direct InhA inhibitors that showed inhibitory activity for both isoniazid sensitive and resistant *M. tuberculosis* strains [86]. To mimic structures of natural substrates for InhA, alkyl chains were added to the diaryl ethers. As a result, the activity greatly increased (**Table 1.4**) [86]. The optimal length of the alkyl chain is 6-8 carbons. The best compound **PT005** has K_i value as low as 1.1 nM and MIC value of 1.9 $\mu\text{g/mL}$.

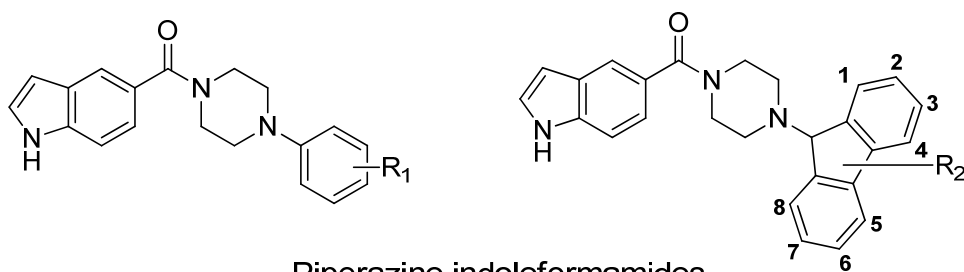
Compounds with other scaffolds were also identified as InhA inhibitors using high-throughput screening (HTS), including pyrrolidine carboxamides [87], piperazine indoleformamides [88-90], pyrazole derivatives [88], and arylamides [87, 90] (**Figure 1.8**). Some of these compounds, as well as diaryl ethers, showed high *in vitro* potency against InhA and *M. tuberculosis* and moderate *in vivo* efficacy.

Table 1.4. SAR study of triclosan against InhA.

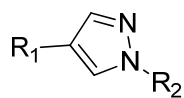
Compound	Structure	IC ₅₀ (nM)	K _i (nM)	MIC (µg/mL)
Triclosan		1000	220 ± 20	12.5 ± 0
PT001		2000		3.8 ± 0
PT006		80		1.0 ± 0
PT004		10	9.4 ± 0.5	2.1 ± 0.9
PT005		5	1.1 ± 0.2	1.9 ± 0.5
PT007		150	30.3 ± 4.7	176



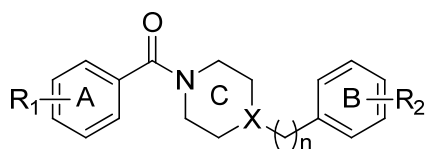
Pyrrolidine carboxamides



Piperazine indoleformamides



Pyrazole derivatives



Arylamides

Figure 1.8. Scaffolds of Other InhA inhibitors

General structures of pyrrolidine carboxamides, piperazine indoleformamides, pyrazoles, and arylamides.

Slow-onset Inhibition of InhA

A central theme in FabI inhibitor discovery concerns the role that inhibitor binding plays in ordering of a loop of amino acids close to the active site, which is known as the substrate binding loop. Based on our own work, we believe that loop ordering is the structural event that occurs when FabI enzymes interact with slow-onset inhibitors. In this type of inhibition, the initial rapid association of enzyme and inhibitor is followed by a slow step that results in formation of the final EI* complex (**Figure 1.9**).

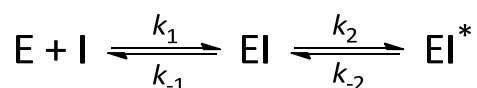


Figure 1.9. The two step mechanism for slow-onset enzyme inhibition.

In this equation, k_1 and k_2 are the forward rate constants of the first and second steps, and k_{-1} and k_{-2} are the backward rate constants of the first and second steps. Assuming that $k_{-1} \gg k_2$ and k_{-2} , then hence the overall dissociation constant $k_{off} \approx k_{-2}$, and the residence time is defined as $1/k_{-2}$ [91].

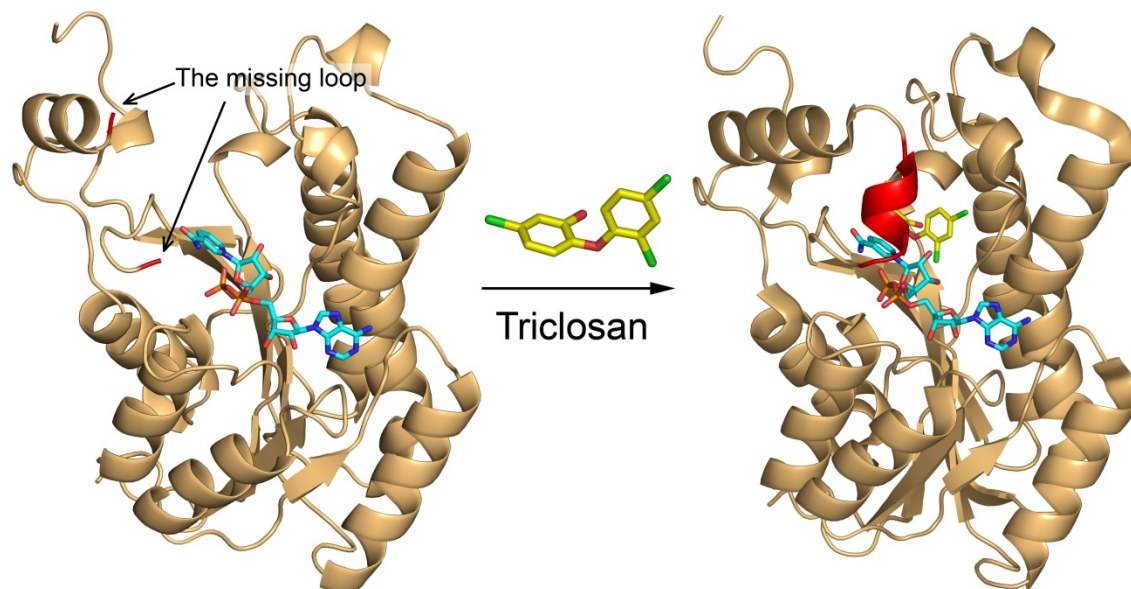


Figure 1.10. Structures of ecFabI in the absence and presence of triclosan.

One part of the substrate binding loop was disordered and missing in the crystallographic structure (left). The ends of the missing loop are in red. The loop becomes ordered and present as an α -helix upon binding of triclosan (right). The loop is in red. The figure was made from 1dfi.pdb [74] and 1qsg.pdb [92] for the binary and ternary enzyme complexes, respectively with PyMol [79].

A classic example of slow-onset inhibition is ecFabI inhibited by the diaryl ether antibacterial agent triclosan [92-94]. The X-ray structures of ecFabI in a binary complex with the oxidized cofactor NAD^+ , and in a ternary complex with NAD^+ and triclosan (**Figure 1.10**) showed that formation of the ternary enzyme inhibitor complex leads to ordering of the substrate binding loop (red).

Importantly, slow-onset enzyme inhibitors have long residence times on their enzyme targets which, in a growing number of cases, is thought to be critical for *in vivo* drug activity [91, 95-97]. In particular, compounds with long residence times will remain bound to their targets even when the free drug concentration is

low, thus prolonging their biological activity. In the case of tuberculosis drug discovery, this hypothesis increases the motivation for developing inhibitors that promote loop ordering and are slow-onset inhibitors of InhA. Previously, our group showed that the slow-onset inhibitor **PT070** (**Figure 1.11**) resulted in ordering of the substrate binding loop of InhA, which confirms the connection between the loop conformation and slow-onset kinetics [98]. However, the structural basis and loop motion mechanism has not been elucidated yet, which hampers the design of new slow-onset inhibitors and modulation of residence times.

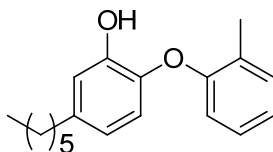


Figure 1.11. The structure of PT070.

Research Project Overview

This research project focuses on chemically modified diaryl ether InhA inhibitors, with the objective of improving antitubercular activity and pharmacokinetics. Detailed structure-activity relationship (SAR) studies have also been performed in order to understand the mechanism of slow-onset inhibition and to modulate the residence time of slow-onset inhibitors of InhA. IC_{50} values were determined for all synthesized inhibitors, and K_i values were determined for selected inhibitors. MIC values were measured against *M. tuberculosis* (H37Rv) by the Slayden lab in Colorado State University.

Previous B-ring analysis of the diaryl ether InhA inhibitors failed to improve the binding affinity to InhA and activity against *M. tuberculosis*. To obtain higher *in vitro* activity, B-ring modified diaryl ethers with more complex structures were synthesized, and their activity was tested with both enzyme and cell based assays. In Chapter 2, we present new diaryl ether inhibitors with similar K_i values but 10-fold lower MIC values, compared to the parent compound **PT070**.

To improve pharmacokinetics, the highly hydrophobic A-ring was modified to include hydrophilic heterocycles, providing new scaffolds for InhA inhibitors. The enzyme binding affinity, MIC values, and pharmacokinetics were determined for these derivatives. In Chapter 3, the effect of the A-ring structure on antimicrobial activity and pharmacokinetics are summarized.

Crystallographic data suggest that substituent groups on the A-ring contribute most to the van der Waals contact between inhibitors and the active site. In Chapter 4, substituent groups on the A-ring were modified to include cyclic structures, and the linker between the groups and the A-ring was changed to oxygen and nitrogen.

Finally, the mechanism of slow-onset inhibition was explored with different diaryl ether inhibitors. Together with results from computational simulation and X-ray crystallography, a new slow-onset mechanism was proposed. In Chapter 5, this mechanism was confirmed with new inhibitors and InhA mutants.

Chapter 2. Modifications on the A-Ring of the Diaryl Ethers that Target InhA.

Isoniazid is activated by the mycobacterial enzyme KatG and subsequently reacts with nicotinamide adenine dinucleotide (NAD⁺/NADH), forming adducts that then inhibit InhA. Mycobacteria primarily acquire resistance to isoniazid through mutations in KatG, therefore, direct InhA inhibitors that do not require intracellular activation will provide a future solution for isoniazid-resistant TB. In 2006, our group reported a series of diaryl ethers that potently inhibit InhA, but the A-ring substituents were seldom modified. To understand the SAR of the A-ring substituents and improve the *in vitro* activities through A-ring modifications, cyclic groups were attached to the A-ring via linkers of various lengths. To lower the ClogP values and enhance the binding affinity, ether and amine linkers were also introduced to the A-ring. The results showed that the addition of cyclic groups on the A-ring can spatially occupy the active site and increase the affinity of the compounds for InhA. Ether linkers in the A ring substituent do not affect the binding affinity significantly, but they diminished antibacterial activity against *M. tuberculosis*. Amine linkers resulted in higher IC₅₀ and MIC values, and thus are not beneficial modifications.

Background

InhA in Fatty Acid Biosynthesis

InhA, the enoyl-ACP reductase from *M. tuberculosis*, is homologous to the FabI enzyme in other bacteria. It catalyzes the last step of the FASII cycle, which involves the reduction of enoyl-ACP to acyl-ACP, using the reduced form of NADH as the cofactor. With both the substrate and the cofactor bound into the active site, the *pro*-S 4-H of NADH is transferred to the β -carbon of the substrate, producing an enolate intermediate and the oxidized cofactor NAD⁺. The intermediate subsequently tautomerizes to the product through protonation (Figure 2.1) [63, 66].

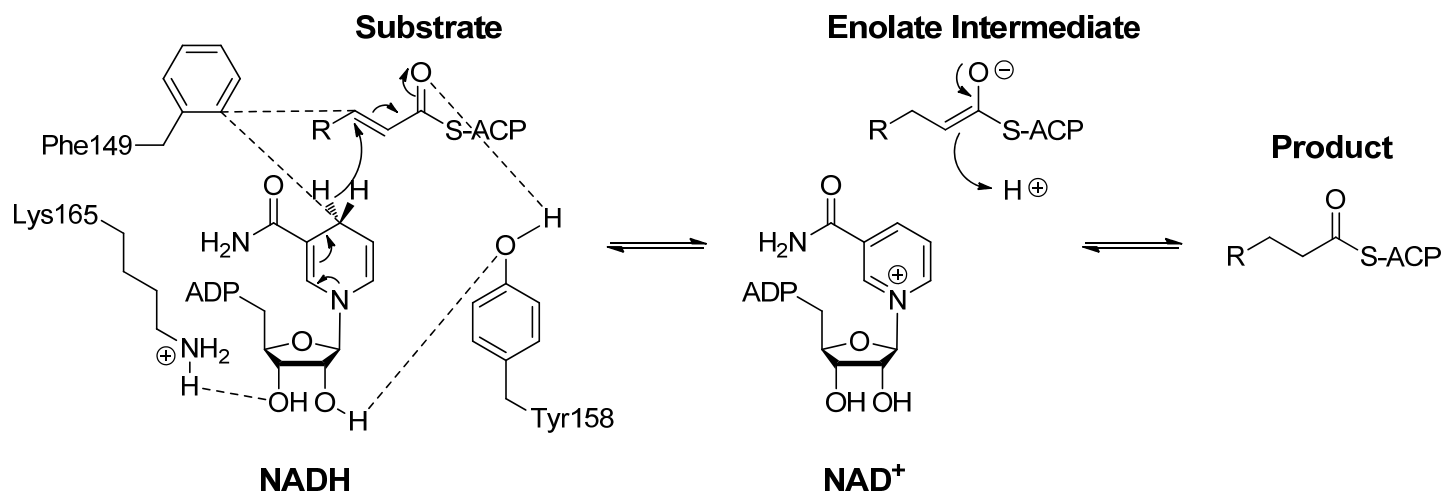


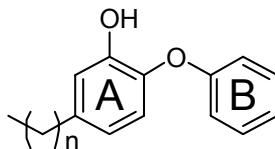
Figure 2.1. The reduction reaction of FASII, catalyzed by InhA.

As described in Chapter 1, InhA is the main target of the front-line antitubercular drug isoniazid [64], which is a prodrug and requires activation by the KatG enzyme [70]. Isoniazid resistance is a major challenge in TB control and, together with resistance to rifampicin, is a component of MDR-TB [70, 81]. As at least 50% of isoniazid-resistant clinical isolates involve deletions or mutations in KatG [81, 99]. Direct inhibition of InhA will overcome the majority of isoniazid resistance.

Diaryl Ethers as InhA Inhibitors

In 2006 our group synthesized a series of diaryl ether compounds that were nanomolar inhibitors of InhA, and showed potent activity against both isoniazid sensitive and resistant strains of *M. tuberculosis* [86, 100] (**Table 2.1**). Linear alkyl groups were introduced into the A-ring of these compounds to mimic the long acyl chains of the natural substrates. The results showed that the binding affinities increased as the alkyl group was elongated from two carbons to eight carbons. The X-ray structure of the **PT005**:InhA complex [86] was compared with that of hexadecenoyl-*N*-acetylcysteamine (16C-NAC) bound to InhA [101], which revealed essential interactions that are involved in substrate binding to InhA (**Figure 2.2**). A longer alkyl group (**PT007**) significantly decreased the binding affinity (**Table 2.1**), probably because the group is too large to be accommodated.

Table 2.1. Development of the diaryl ethers.



Compound	IC ₅₀ (nM)	MIC ^a (μg/mL)			
		H37 _{Rv}	W210	TN587	NHN20
Triclosan	1000 ± 100	12.5 ± 0	14.7 ± 3.8	12.5 ± 0	12.5 ± 0
PT001 (n=1)	2000 ± 700	3.8 ± 0	N.D. ^b	N.D. ^b	N.D. ^b
PT006 (n=3)	80 ± 15	N.D. ^b	N.D. ^b	N.D. ^b	N.D. ^b
PT004 (n=5)	11 ± 1	2.1 ± 0.9	2.9 ± 0.4	2.0 ± 1.0	3.1 ± 0
PT005 (n=7)	5.0 ± 0.3	1.9 ± 0.5	2.6 ± 0.4	2.0 ± 1.0	2.4 ± 0.76
PT007 (n=13)	150 ± 24	176	N.D. ^b	N.D. ^b	N.D. ^b
Isoniazid	N.D. ^b	0.05 ± 0	0.03 ± 0.02	2.4 ± 1.3	0.03 ± 0

a H37_{Rv} is isoniazid-sensitive *M. tuberculosis*. W210, TN587, NHN20 are clinical strains of *M. tuberculosis* with various sensitivities to isoniazid.

b Not determined.

The table was reproduced from [86].

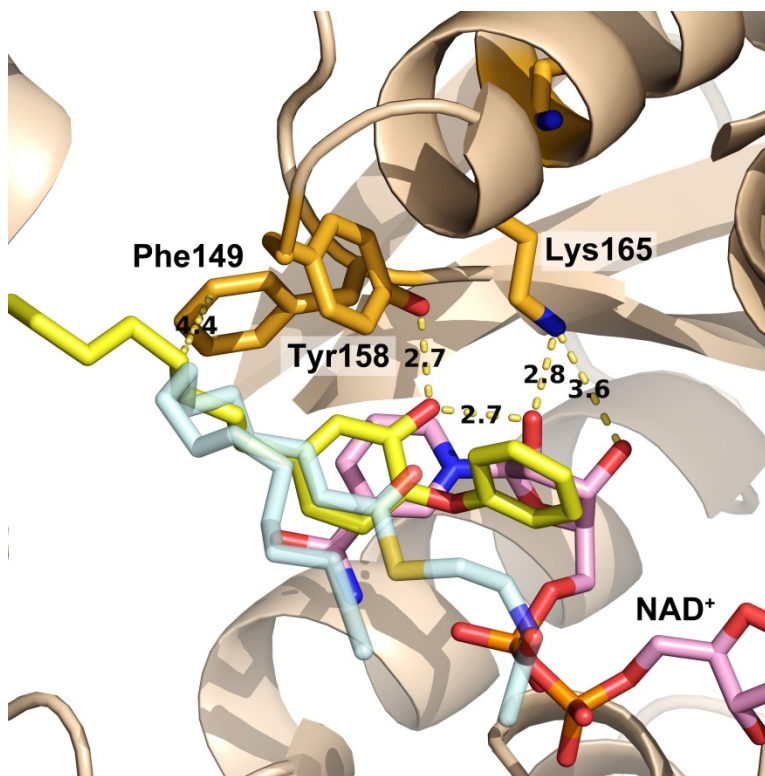


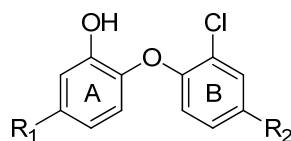
Figure 2.2. Interactions between PT005 and residues in the active site.

Overlaid X-ray crystallographic structures of **PT005** (yellow, 2b37.pdb) [86] and 16C-NAC (pale cyan, 1bvr.pdb) [101] bound to InhA, in the presence of NAD^+ (pink). The figure was generated with PyMol [102]

The superimposed structures showed that the diphenyl ethers bind to the active site with favored interactions, including hydrogen bonding with Tyr158 and Lys165 and hydrophobic contacts between Phe149 and the A-ring octyl group. In addition, hydrogen bonding between the A-ring phenol and the ribose of NAD^+ , along with π - π stacking between the A-ring and the nicotinamide of NAD^+ also stabilized the enzyme-inhibitor complex. The hydrophobic contacts between the A-ring alkyl group and Phe149 are especially important, since variation in lengths of the alkyl groups could change the binding affinity by hundreds of folds.

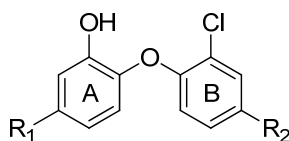
Freundlich and coworkers reported a series of diaryl ethers based on the structure of triclosan with various A-ring substituents (**Table 2.2**) [103]. The activity data indicated that hydrophobic interactions are favored for the A-ring substituents, with a correlation between the length of the alkyl group and the binding affinity, which is consistent with previous observations by our group (**Table 2.1**) [86]. When a cyclic group is introduced into the A-ring, a linker with at least one carbon is necessary for tight binding inhibitors. Compounds that have benzene or pyridine connected to the A-ring through linkers varying from one to three carbons showed similar activity. The crystallographic structure of **F7** (3fng.pdb) [103] revealed key interactions between the inhibitor and the active site residues (**Figure 2.3**), which includes hydrogen bonding and hydrophobic contacts similar to the diaryl ether inhibitors reported by our group.

Table 2.2. SAR of the A-ring of the diaryl ethers.



	Compound		IC ₅₀ (nM)	MIC (µg/ml)
	R ₁	R ₂		
15	-CH ₃	-Cl	800 ± 99	N.D. ^b
16		-Cl	>10,000	N.D. ^b
17	-COOH	-Cl	>10,000	N.D. ^b
18	-CONH ₂	-Cl	>10,000	N.D. ^b
19	-Ph	-Cl	>10,000	N.D. ^b
20	-CH ₂ Cy	-Cl	110 ± 31	9.4
21	-CH ₂ CH ₃	-Cl	120 ± 19	N.D. ^b
22	-(CH ₂) ₂ CH ₃	-Cl	91 ± 15	N.D. ^b
23	-(CH ₂) ₃ CH ₃	-Cl	55 ± 20	9.4
24		-Cl	96 ± 46	19
25		-Cl	63 ± 9	N.D. ^b
26		-Cl	130 ± 56	N.D. ^b
27	2-pyridyl	-CN	>10,000	N.D. ^b
28	3-pyridyl	-Cl	>10,000	N.D. ^b
29	4-pyridyl	-CN	>10,000	N.D. ^b

Table 2.2. SAR of the A-ring of the diaryl ethers.



	Compound		IC ₅₀ (nM)	MIC (µg/ml)
	R ₁	R ₂		
30	-CH ₂ (2-pyridyl)	-Cl	29 ± 11	N.D. ^b
31	-CH ₂ (3-pyridyl)	-Cl	42 ± 10	N.D. ^b
32	-CH ₂ (4-pyridyl)	-CN	75 ± 16	N.D. ^b
33	- <i>o</i> -tolyl	-Cl	1300 ± 77	N.D. ^b
34	- <i>o</i> -tolyl	-CN	>10,000	N.D. ^b
35	- <i>m</i> -tolyl	-Cl	870 ± 110	N.D. ^b
36	<i>p</i> -F-Ph-	-Cl	>10,000	N.D. ^b
37	-Bn	-Cl	51 ± 6	9.4
38	-(CH ₂) ₂ Ph	-Cl	21 ± 8	19
39	-(CH ₂) ₃ Ph	-Cl	50 ± 14	4.7
Triclosan			1000 ± 100 ^a	12.5 ± 0 ^a
Isoniazid			N/A	0.05 ± 0 ^a

The table was reproduced from [103].

a Data were taken from [86].

b Not determined.

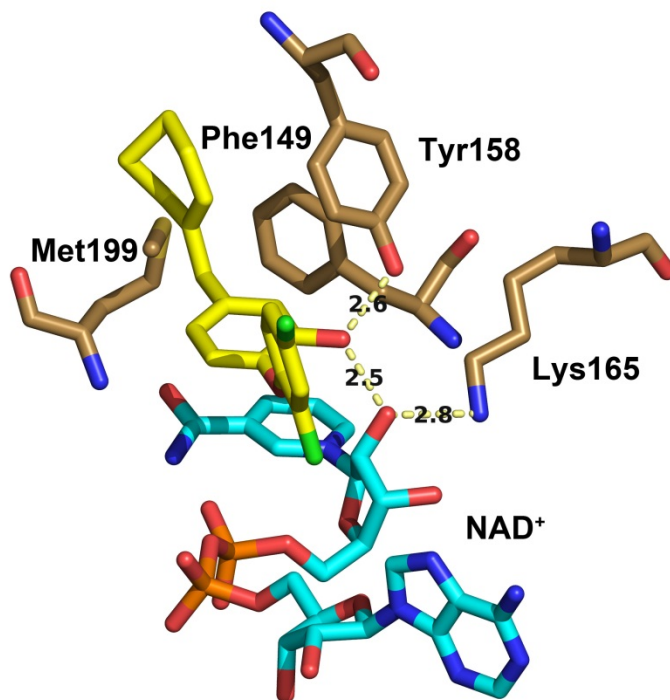


Figure 2.3. Compound 20 bound to InhA.

The structure shows important interactions between compound **20** (yellow), the cofactor NAD^+ (cyan), and key residues in the active site. The figure was made with 3fng.pdb [103] and PyMol [102].

Modifications to the A-Ring Substituents

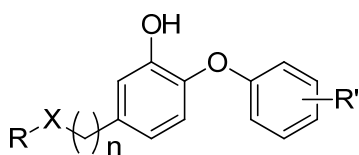
Although the diaryl ethers showed potent binding affinity to InhA, most of their MIC values are higher than isoniazid. Therefore, two designs were proposed to improve the activity of the diaryl ethers against *M. tuberculosis* (**Figure 2.4**):

- 1) Changes in the size and shape of the A-ring substituents to increase the binding affinity.

Based on previous SAR studies, van der Waals interactions contribute most to the binding affinity, and cyclic groups are well tolerated in the active site. Therefore, phenyl and cyclohexyl groups were attached to the A-ring through linkers with one or two carbons. These derivatives were evaluated with enzyme and cell based assays to understand the SAR of A-ring substituents and synthesize inhibitors with higher binding affinity.

2) A-ring substituents with ether or amine linkers to lower the ClogP values and increase cell membrane permeability.

Another reason that the diaryl ethers do not show sub-micromolar MIC values may be high ClogP values (>5.5) that could result in poor cell membrane permeability. To lower the ClogP values and improve cell permeability, ether and amine linkers were used to connect substituents to the A-ring.



X = C, O, N

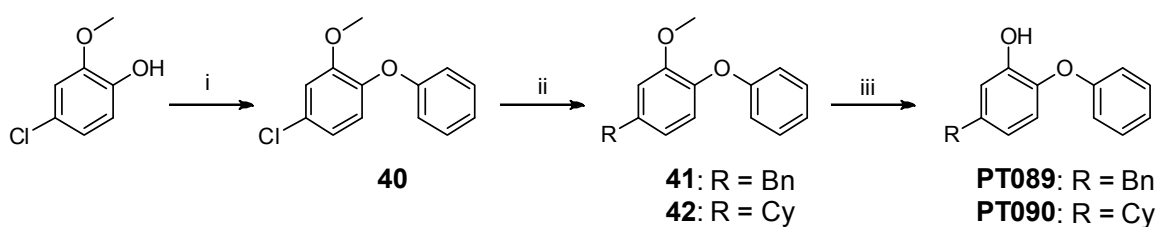
R = alkyl, phenyl, cyclohexyl

n = 0, 1

Figure 2.4. Designs of A-ring substituents.

Synthesis Strategies for the Diaryl Ethers with A-Ring Substituents

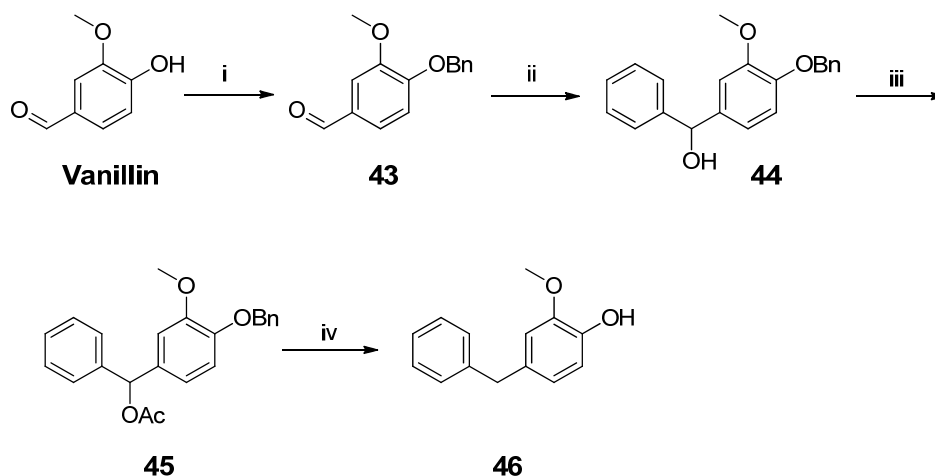
Synthesis of compound **PT089** and **PT090** was accomplished by following previously reported methods (**Scheme 2.1**) [86, 104]. Briefly, a Buchwald-Hartwig coupling reaction was used to connect the commercially available A-ring and B-rings, and the following Negishi coupling introduced the A-ring substituents. Finally, demethylation with BBr_3 gave the target compounds **PT089** and **PT090**.



Scheme 2.1. Synthesis of compound **PT089** and **PT090**.

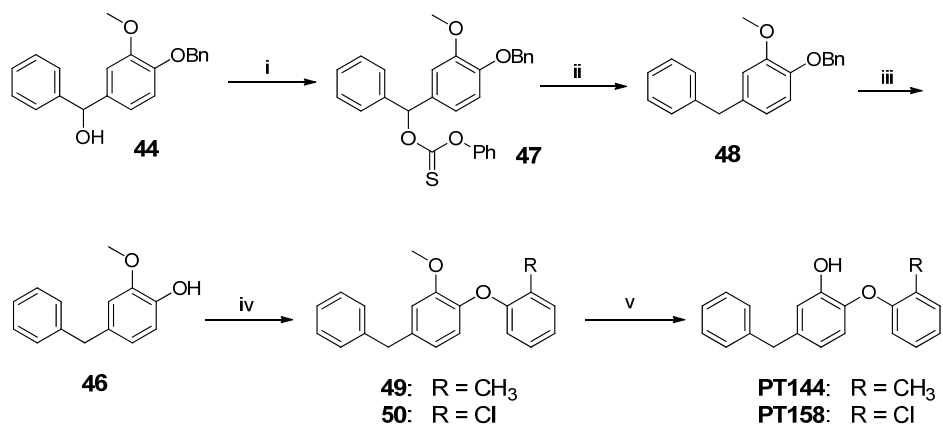
Reagents and conditions: i) $(\text{CuOTf})_2 \cdot \text{PhH}$, Cs_2CO_3 , ArCO_2H , EtOAc , toluene, $110\text{ }^\circ\text{C}$, 24 hr, 76%; ii) R-ZnCl_2 , 2% $\text{Pd}(\text{P}(t\text{-Bu})_3)_2$, THF/NMP , $130\text{ }^\circ\text{C}$, 48 hr; iii) BBr_3 , CH_2Cl_2 , $-78\text{ }^\circ\text{C}$ to rt.

The palladium catalyst used in Negishi coupling is expensive and difficult to store due to its high sensitivity to air and moisture. Consequently, synthesis schemes that avoid the use of Negishi coupling were developed. The key intermediate **46** was obtained with four steps (**Scheme 2.2**). First, vanillin was benzylated and then reacted with PhMgCl to give compound **44**. Acetylation and hydrogenation provided compound **46**. The hydrogenation was performed at different conditions, and only high pressure H_2 (>20 psi) produced by a hydrogenator gave compound **46**.



Scheme 2.2. Synthesis of the intermediate 46.

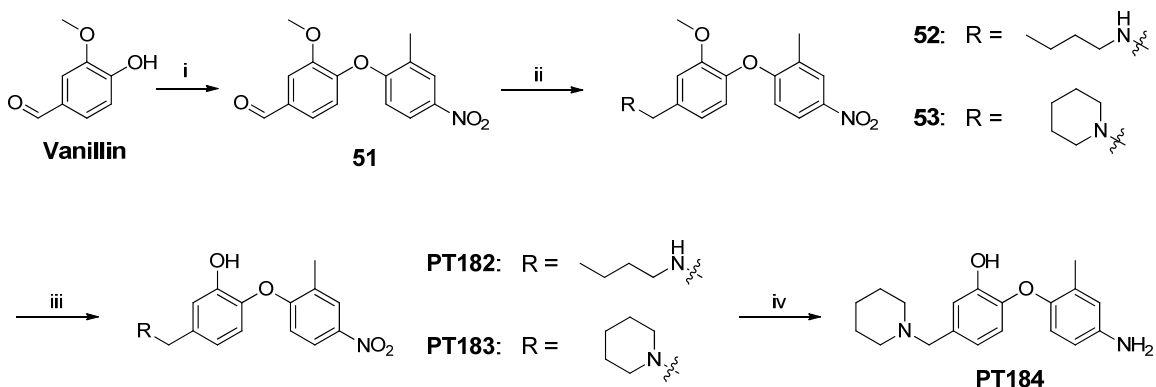
Reagents and conditions: i) BnBr, KOH (5% aq), MeOH, reflux, 2 hr, 91%; ii) PhMgCl, CH₂Cl₂, 0 to rt, 1 hr, 92%; iii) Ac₂O, pyridine, 0 to rt, 1.5 hr, 96%; iv) H₂, Pd-C, EtOH, overnight, 83%.



Scheme 2.3. Synthesis of PT144 and PT158.

Reagents and conditions: i) phenyl carbonochloridothioate, Py, CH₂Cl₂, 4 hr, rt, 91%; ii) (*n*-Bu)₃SnH, AIBN, toluene, 115 °C, 24 hr, 86%; iii) H₂, Pd-C, EtOH, 6 hr, rt, 93%; iv) (CuOTf)₂·PhH, Cs₂CO₃, ArCO₂H, EtOAc, toluene, 110°C, 24 hr; v) BBr₃, CH₂Cl₂, -78°C.

As an alternative to hydrogenation, (**Scheme 2.3**), compound **44** was converted to compound **47**, and then the thionoester was cleaved by Barton-McCombie deoxygenation [105] using $(n\text{-Bu})_3\text{SnH}$ as the hydrogen donor. The benzyl group was removed by hydrogenation to give compound **46**. Finally, Buchwald coupling and demethylation described above gave compounds **PT144** and **PT158**.

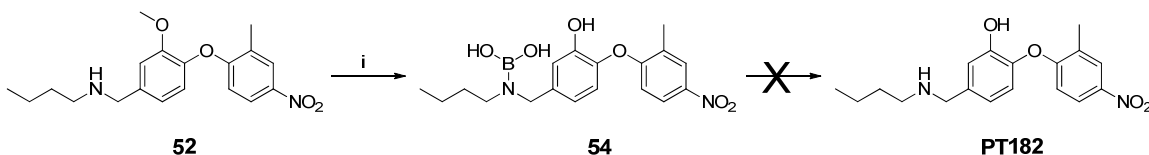


Scheme 2.4. Derivatives with amine substituents on the A-ring.

Reagents and conditions: i) K_2CO_3 , 2-fluoro-5-nitrotoluene, 18-crown-6, DMF, 110°C , 2 hr, 84%; ii) amine, NaBH_3CN , THF, rt, 2 hr; iii) HBr (44%), AcOH, 120°C , overnight; iv) Zn, NH_4Cl , MeOH, reflux, 0.5 hr, 73%.

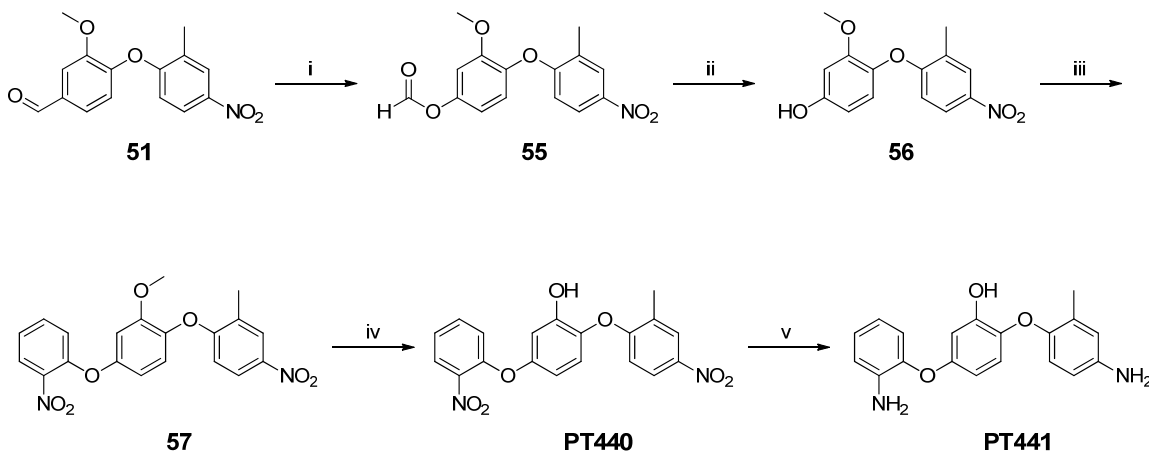
The diaryl ethers with amine substituted A-rings were synthesized starting with a $\text{S}_{\text{N}}\text{Ar}$ reaction of vanillin (**Scheme 2.4**). A linear and a cyclic amine were attached to aldehyde **51** using reductive amination with NaBH_3CN [106] to give compounds **52** and **53**. Demethylation of compound **52** with BBr_3 provided only the byproduct **54**, because of the nucleophilicity of the amine (**Scheme 2.5**).

Attempts at converting **54** to **PT182** with NaOH were not successful. An alternative route involving HBr and AcOH [107, 108] was used to hydrolyze **52** and **53** to the corresponding diaryl ethers (**Scheme 2.4**). Subsequently, Clemmensen reduction of **PT183** gave **PT184**.



Scheme 2.5. Demethylation with BBr₃.

Reagents and conditions: i) BBr₃, CH₂Cl₂, 0 to rt, overnight.



Scheme 2.6. Synthesis of the diaryl ethers with ether substituted A-rings.

Reagents and conditions: i) *m*-CPBA, CH₂Cl₂, rt, overnight, 88%; ii) K₂CO₃, MeOH, H₂O, reflux, 1 hr, 80%; iii) K₂CO₃, 1-fluoro-2-nitrobenzene, 18-crown-6, DMF, 110 °C, 2 hr, 85%; iv) BBr₃, CH₂Cl₂, 0 °C to rt, 3 hr, 82%; v) Zn, NH₄Cl, MeOH, reflux, 0.5 hr, 74%.

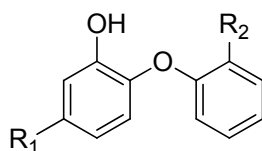
Ethers were introduced into the A-ring substituents by peroxidation of compound **51** with *m*-CPBA, followed by hydrolysis with K₂CO₃ (**Scheme 2.6**). Compound **56** was then connected to nitrobenzene by a S_NAr reaction with 1-fluoro-2-nitrobenzene. Demethylation of compound **57** gave **PT440**, which could be converted to **PT441** by a Clemmensen reduction.

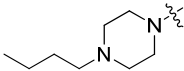
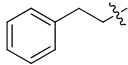
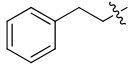
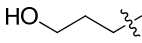
Results and Discussion

Van Der Waals Space for A-Ring Substituents

Phenyl, cyclohexyl, and other linear groups were introduced into the A-ring of the diaryl ethers, and their IC₅₀ and MIC values were determined (**Table 2.3**). The diaryl ethers **PT004**, **PT070**, and **PT091** with an A-ring hexyl group were used as the control compounds for phenyl, tolyl, and *ortho*-chlorophenyl B-rings, respectively. The results showed that hydrophobic A-ring substituents are favored, while highly polar groups resulted in weak binding affinity (**PT066**, **PT094**, and **PT100**). The shape of the A-ring substituent, either linear or cyclic, does not affect binding significantly, but the linker, however, is important for inhibition. Compounds that lack a flexible linker between the A-ring and cyclic groups have very high IC₅₀ and MIC values (**PT090** and **PT100**). A methylene linker between the A-ring and the phenyl group (**PT089**, **PT144**, and **PT158**) resulted in the same IC₅₀ and MIC values as the parent compounds, while a two-carbon linker (**PT084** and **PT162**) increased IC₅₀ values by 7-10 fold and MIC values by 4 fold. These SAR observations are consistent with previously reported data [103]. The X-ray crystallographic structure of **PT070** bound to InhA was superimposed with that of compound **20** (**Figure 2.5**). The structures showed that both compounds bind to the same region of the active site and that the cyclohexyl group and the hexyl group occupy the same space and tightly fit into the active site. However, a cyclic group should be a better pharmacophore, considering that it has less degrees of freedom.

Table 2.3. The diaryl ethers with various A-ring substituents.



	Compound		IC ₅₀ (nM)	MIC (µg/mL)
	R ₁	R ₂		
PT004^a	<i>n</i> -C ₆ H ₁₃	-H	11 ± 1	2.1
PT066	-COH	-H	N/A ^d	40.8
PT090	-Cy	-H	820.7 ± 153.1	12.5
PT100		-H	N/A ^d	70.0
PT089	-Bn	-H	49.6 ± 3.3	3.13
PT084		-H	144.1 ± 13.4	12.5
PT070^{b, c}	<i>n</i> -C ₆ H ₁₃	-CH ₃	50.7 ± 4.2	3.13
PT144	-Bn	-CH ₃	56.4 ± 5.5	3.13
PT162		-CH ₃	360.1 ± 78.4	12.5
PT094		-CH ₃	4326 ± 628	N.D. ^e
PT091^c	<i>n</i> -C ₆ H ₁₃	-Cl	49.5 ± 2.2	1.56
PT158	-Bn	-Cl	20.08 ± 2.24	1.25

^a Data taken from [86].

^b Data taken from [109].

^c Compounds will be discussed in Chapter 3.

^d No significant inhibition observed at 1 µM.

^e Not determined.

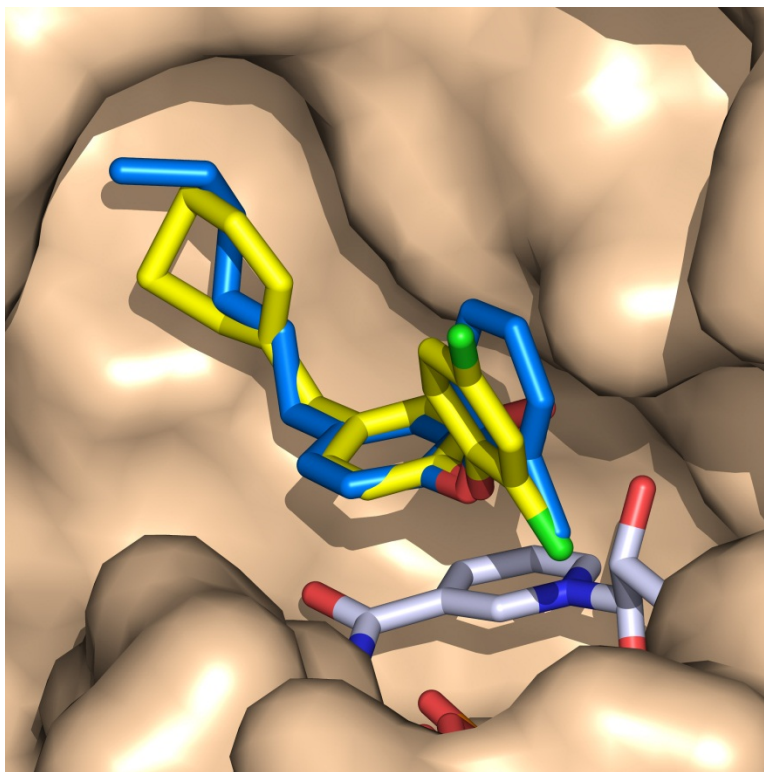


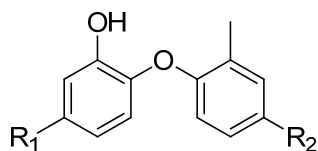
Figure 2.5. PT070 and compound 20 bound to the active site of InhA.

Overlaid structures of **PT070** (blue, 2x23.pdb) [109] and **20** (yellow, 3fng.pdb) [103] bound to InhA, in the presence of NAD⁺ (gray).

The Diaryl Ethers with Amine and Ether Substituted A-rings

To lower the ClogP values and thus improve cell permeability, amine and ether substituted A-rings were included in the diaryl ethers (**Table 2.4**). **PT070** [109] and **PT107** were used as the control compounds, and their activities will be discussed in Chapter 3 in detail. Derivatives **PT184** and **PT441** have not been tested yet, so they are not included in the table.

Table 2.4. A-ring substituents with ether and amine linkers.



Compound	Compound		IC ₅₀ (nM)	MIC (μg/mL)
	R ₁	R ₂		
PT070^{a, b}	<i>n</i> -C ₆ H ₁₃	-H	50.7 ± 4.2	3.13
PT181		-H	253.1 ± 14.4	50
PT160		-H	94.2 ± 5.3	12.5
PT107^b	<i>n</i> -C ₆ H ₁₃	-NO ₂	50 ± 5	6.25
PT182		-NO ₂	N/A ^c	N.D. ^d
PT183		-NO ₂	N/A ^c	N.D. ^d
PT440		-NO ₂	88.1 ± 3.6	12.5

a Data taken from [109].

b Compounds will be discussed in Chapter 3.

c No significant inhibition observed at 1 μM.

d Not determined.

Consistent to previous SAR data, **PT181**, with a polar A-ring substituent showed significantly higher IC₅₀ and MIC values, whereas an ether linker in the A-ring substituent (**PT160** and **PT440**) resulted in similar binding affinity, compared to the parent compounds. Surprisingly, both compounds showed much higher MIC values than the parent compounds. This may be because the ether bond is less stable than alkyl bond and could be hydrolyzed inside the cells. Amino groups on the A-ring (**PT182** and **PT183**) totally abolished activity against InhA and *M. tuberculosis*, which indicates that 2'-nitrogen is not favored in the hydrophobic active site, because either the amine or water molecules solvating the amine are highly hydrophilic.

Summary

To understand the SAR of the A-ring substituents and improve the binding affinity of the diaryl ethers to InhA, various groups were introduced into the A-ring. Only hydrophobic groups were favored in the active site, because most residues in this portion of the substrate binding site are nonpolar. Our data are consistent with SAR results reported by Freundlich [110], showing that the active site can accommodate A-ring substituents of various sizes and shapes, but that a linker between the A-ring and these bulky substituents is essential.

For our diaryl ether inhibitors, a methylene linker resulted in the same activity as the parent compounds with an A-ring hexyl group, and is better than a two-carbon linker.

Ether connected hexyl and phenyl groups on the A-ring both resulted in similar IC_{50} values, compared to the parent compounds, but higher MIC values, which may be because of the instability of the ether bond. Amines on the A-ring totally abolished binding affinity, indicating that polar groups are not tolerated.

Experimental Section

Measurement of IC₅₀ Values

The half maximal inhibitory concentration (IC₅₀) refers to the concentration of inhibitor that effects a 50% reduction in enzymatic activity under a specific set of reaction conditions. Determination of IC₅₀ values is a rapid assay to compare inhibitor affinity. However, the result is dependent on enzyme concentration, substrate, and substrate concentration, and it does not give mechanistic information.

Kinetic assays using DD-CoA and InhA were performed as described previously [111]. NADH (250 μM), DD-CoA (22 μM), and the inhibitor were first mixed in PIPES buffer (pH 6.8). Initial velocities were measured after the reaction was initiated by adding InhA (20, 50, or 100 nM). IC₅₀ values were determined by varying the concentration of the inhibitor and fitting the experimental data to **Equation 2.1**.

$$y = 100\% / [1 + ([I]/IC_{50})^s] \quad \text{Equation 2.1}$$

In **Equation 2.1**, [I] is the inhibitor concentration, y is percent activity (the ratio between initial velocities with and without inhibitors), and the slope factor (s) is 1.0. Data fitting was performed using Grafit 4.0 (Erithacus Software Ltd.). Raw data of PT144 were given as an example (**Table 2.5, Figure 2.6**).

Table 2.5. Initial velocities at various concentrations of PT144.

[PT144] (nM)	0	10	20	40	80	160	320
Initial velocities (Abs/min)	0.0535	0.0470	0.0426	0.0337	0.0201	0.0139	0.0074
<i>y</i>	100	87.9	79.6	63.0	37.6	26.0	13.8

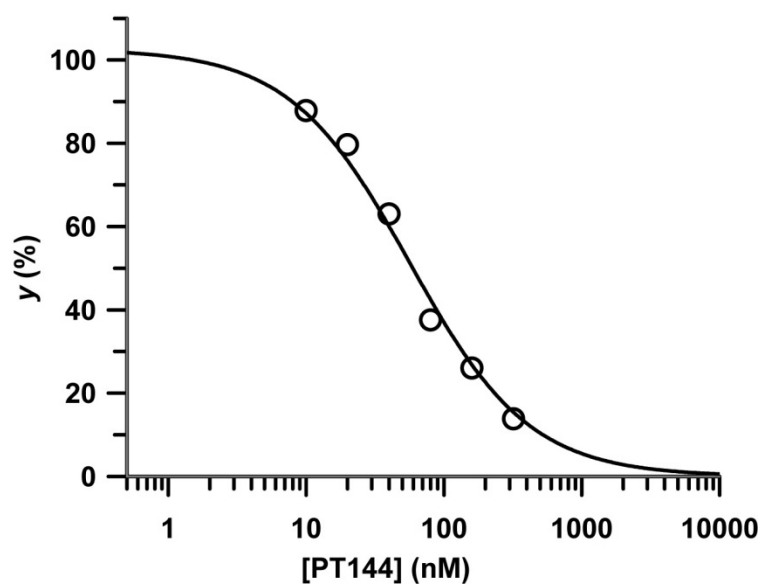


Figure 2.6. The semilog concentration-response plot of PT144 titration.

Organic Synthesis

The synthesis of some final compounds and necessary intermediates is described in this section. The other compounds were synthesized by other lab members and Sai Advantium Pharma Ltd., India (**Table 2.6**). All commercially available chemicals and solvents were used without further purification. All new compounds gave satisfactory spectroscopic and/or analytical data. ^1H and ^{13}C NMR spectra were recorded at 300, 400, or 500 MHz, and chemical shifts are reported in parts per million (δ) downfield from the internal standard tetramethylsilane (TMS). Mass spectra were obtained using electrospray (ES) ionization techniques.

Table 2.6. Contributors for synthesis of the diaryl ethers.

Compound	Synthesis performed by
PT066	Avinash Khanna
PT084	Avinash Khanna
PT089	Pan Pan
PT090	Pan Pan
PT094	Avinash Khanna
PT100	Avinash Khanna
PT144	Nimali Weerasooriya and Pan Pan
PT158	Nimali Weerasooriya and Pan Pan

Table 2.6. Contributors for synthesis of the diaryl ethers.

Compound	Synthesis performed by
PT160	Pan Pan
PT162	Pan Pan
PT181	Pan Pan
PT182	Pan Pan
PT183	Pan Pan
PT184	Pan Pan
PT440	Pan Pan
PT441	Pan Pan

4-Chloro-2-methoxy-1-phenoxybenzene (40)

Reagents 2-iodobenzene (1.5 g, 7.35 mmol), vanillin (1.1 g, 7.35 mmol), Cs_2CO_3 (10.5 g, 32.3 mmol), $(\text{CuOTf})_2 \cdot \text{PhH}$ (185.0 mg, 0.37 mmol, 5.0 mol % Cu), and 1-naphthoic acid (5.56 g, 32.3 mmol) were dissolved in ethyl acetate (1 mL) and toluene (75 mL) and placed in an oven-dried 100 mL two-necked round-bottomed flask. Molecular sieves 4 Å (1.8 g) were added into the flask which was flushed with nitrogen gas, and then the flask was sealed with a septum and heated to 120 °C under nitrogen. After stirring for 24 hr, the flask was cooled to rt, CH_2Cl_2 (100 mL) was added and the organic phase was obtained by filtration. This solution was washed with 5% NaOH. The aqueous layer was then extracted with CH_2Cl_2 and the combined organic layers were washed with brine, dried over Mg_2SO_4 and concentrated under vacuum to give the crude product, which was

then purified by flash chromatography on silica gel (5% ethyl acetate/hexane) to give pure **40** as pale yellow crystals. Yield 76%; ^1H NMR (400 MHz, CDCl_3): δ 7.30-7.23 (m, 2H), 7.04 (t, $J = 7.2$ Hz, 1H), 6.96 (d, $J = 1.2$ Hz, 2H), 6.90 (dd, $J = 8.8, 1.2$ Hz, 2H), 6.87 (d, $J = 1.2$ Hz, 1H), 3.80 (s, 3H); ^{13}C NMR (100 MHz, CDCl_3): δ 157.48, 151.83, 143.73, 129.51, 122.69, 121.62, 120.80, 117.08, 113.36, 56.20 ppm.

4-Benzyl-2-methoxy-1-phenoxybenzene (41)

A solution of benzyl magnesium chloride in THF (2.0 M, 0.6 mL, 1.2 mmol) was added dropwise to a solution of ZnCl_2 in THF (1.0 M, 1.2 mL, 1.2 mmol), and NMP (15 mL) was added after 20 min, followed by $\text{Pd}[\text{P}(\text{t-Bu})_3]_2$ (10.2 mg, 0.02 mmol) and **40** (234.7 mg, 1.0 mmol). The reaction was stirred at 130°C for 48 hr. When TLC showed that the reaction was complete, the mixture was washed with Et_2O (20 mL, 3X), and the organic layer was subsequently washed with water (50mL, 2X). Purification by flash chromatography (ethyl acetate/petroleum ether 2%) gave the pure compound **41** as white crystals. Yield 79%; ^1H NMR (300 MHz, CDCl_3): δ 7.39-7.25 (m, 7H), 7.07 (tt, $J = 7.5, 2.0$ Hz, 1H), 7.01-6.94 (m, 3H), 6.87 (d, $J = 1.8$ Hz, 1H), 6.79 (dd, $J = 8.1, 2.1$ Hz, 1H), 4.03 (s, 2H), 3.81 (s, 3H) ppm; ESI-MS (m/z): calcd for $\text{C}_{20}\text{H}_{18}\text{O}_2$ $[\text{M}+\text{H}]^+$ 291.1; found, 291.2.

4-Cyclohexyl-2-methoxy-1-phenoxybenzene (42)

The compound was synthesized by the same procedure described in the synthesis of **41**, using a solution of cyclohexyl magnesium chloride in THF (2.0M).

Purification by flash chromatography (ethyl acetate/petroleum ether 2%) gave the pure compound **42** as a colorless oil. Yield 74%; ESI-MS (*m/z*): calcd for C₁₉H₂₂O₂ [M+H]⁺ 283.2; found, 283.1.

4-(Benzyloxy)-3-methoxybenzaldehyde (43)

Vaniline (10 g, 65.7 mmol), benzyl bromide (12.4 g, 72.3 mmol), and KOH (4.1 g, 72.3 mmol) were dissolved in methanol/water (50%, 150 mL) and heated to reflux for about 1 hr. When TLC showed that the reaction was complete, the solution was extracted with water (100 mL) and CH₂Cl₂ (200 mL). The organic layer was dried with MgSO₄ and concentrated to give the crude product. Purification by flash chromatography (ethyl acetate/petroleum ether 8%) gave **43** as white crystals. Yield 91%; ¹H NMR (400 MHz, CDCl₃): δ 9.81 (s, 1H), 7.42-7.29 (m, 7H), 6.96 (d, *J* = 6.3 Hz, 1H), 5.22 (s, 2H), 3.92 (s, 3H) ppm; ¹³C NMR (100 MHz, CDCl₃): δ 191.12, 153.83, 150.31, 136.23, 130.54, 128.93, 128.41, 127.41, 126.75, 112.63, 109.62, 71.09, 56.28 ppm; HRMS (*m/z*): calcd for C₁₅H₁₄O₃ [M+H]⁺ 243.1021; found, 243.1022.

(4-(Benzyloxy)-3-methoxyphenyl)(phenyl)methanol (44)

A solution of **43** (2.4 g, 10.0 mmol) in CH₂Cl₂ (150 mL) was cooled to 0 °C, and a solution of phenyl magnesium chloride in THF (2.0 M, 5.0 mL, 10.0 mmol) was added dropwise into the flask. The reaction was stirred for approximately 1 hr, while the ice bath gradually melted to rt. When TLC (ethyl acetate/petroleum ether 15%) showed that the reaction was complete, the solution was poured into

sat. NaHCO₃ solution (200 mL) and extracted with CH₂Cl₂ (100 mL, 3X). The organic layers were combined and dried over MgSO₄. Purification by flash chromatography (ethyl acetate/petroleum ether 10%) gave **44** as pale yellow crystals. Yield 92%; ¹H NMR (300 MHz, CDCl₃): δ 7.44-7.26 (m, 10H), 6.95 (s, 1H), 6.82 (t, *J* = 8.1 Hz, 2H), 5.78 (d, *J* = 3.0 Hz, 1H), 5.14 (s, 2H), 3.86 (s, 3H), 2.27 (d, *J* = 3.0 Hz, 1H) ppm; ESI-MS (*m/z*): calcd for C₂₁H₂₀O₃ [M-OH]⁺ 303.1; found, 303.1.

(4-(Benzyloxy)-3-methoxyphenyl)(phenyl)methyl acetate (45)

A solution of **44** (1.6 g, 5.0 mmol) in anhydrous pyridine (50 mL) was cooled to 0 °C, and acetic anhydride (561.5 mg, 0.5 mL, 5.5 mmol) was added dropwise to the solution. The reaction was stirred for approximately 1.5 hr, and when TLC (ethyl acetate/petroleum ether 10%) showed that the reaction was complete, the solution was poured into sat. NaHCO₃ solution (100 mL) and extracted with CH₂Cl₂ (60 mL, 3X). The organic layers were combined and dried over MgSO₄. Purification by flash chromatography (ethyl acetate/petroleum ether 8%) gave **45** as pale yellow crystals. Yield 96%; ESI-MS (*m/z*): calcd for C₂₃H₂₂O₄ [M-OAc]⁺ 303.2; found, 303.1.

4-Benzyl-2-methoxyphenol (46)

Compound **48** (1.5 g) was dissolved in EtOH (50 mL), and palladium charcoal (75.0 mg) was added to the solution. The mixture was sealed under vacuum, flushed with hydrogen gas, and stirred at rt for 6 hr. After TLC (ethyl

acetate/petroleum ether 10%) demonstrated that the reaction was complete, the mixture was filtered through Celite 545, and the filtrate was evaporated to give the crude product, which was used in the next step without further purification. ESI-MS (m/z): calcd for $C_{14}H_{14}O_2$ $[M-H]^-$ 213.1; found, 213.1.

O-((4-(benzyloxy)-3-methoxyphenyl)(phenyl)methyl) O-phenyl carbonothioate (47)

A solution of **44** (1.6 g, 5.0 mmol) in anhydrous CH_2Cl_2 (100 mL) and pyridine (20 mL) was cooled to 0 °C on an ice bath, and phenyl carbonochloridothioate (949.3 mg, 5.5 mmol) was added to the solution. The ice bath was removed, and the reaction was stirred at rt for approximately 4 hr. When TLC (ethyl acetate/petroleum ether 10%) demonstrated that the reaction was complete, the solution was poured into sat. $NaHCO_3$ solution (300 mL) and extracted with CH_2Cl_2 (100 mL, 3X). The organic layers were combined and dried over $MgSO_4$. Purification by flash chromatography (ethyl acetate/petroleum ether 8%) gave pure **47** as a bright yellow solid. Yield 91%; ESI-MS (m/z): calcd for $C_{28}H_{24}O_4S$ $[M-OCSOPh]^+$ 303.1; found, 303.1.

4-Benzyl-1-(benzyloxy)-2-methoxybenzene (48)

Compound **47** (1.8 g, 4.0 mmol), $(n-Bu)_3SnH$ (1.6 mL, 1.7 g, 6.0 mmol), and AIBN (131.4 mg, 0.8 mmol) were dissolved in toluene (100 mL), and the mixture was heated to 115 °C to reflux for 24 hr. When TLC (ethyl acetate/petroleum ether 5%) showed completion of the reaction, the mixture was cooled to rt and

washed with water (200 mL) and ethyl acetate (100 mL). The organic layer was dried over MgSO₄ and evaporated to give the crude compound. Purification by flash chromatography (ethyl acetate/petroleum ether 4%) gave pure **48** as white crystals. Yield 86%; ESI-MS (*m/z*): calcd for C₂₁H₂₀O₂ [M+H]⁺ 305.2; found, 305.1.

4-Benzyl-2-methoxy-1-(*o*-tolylloxy)benzene (49)

The compound was synthesized using the Buchwald reaction described in the synthesis of **40**, with compound **46** and 2-iodotoluene. The crude product was used in the next step without further purification. ESI-MS (*m/z*): calcd for C₂₁H₂₀O₂ [M+H]⁺ 305.2; found, 305.1.

4-Benzyl-1-(2-chlorophenoxy)-2-methoxybenzene (50)

The compound was synthesized using the Buchwald reaction described in the synthesis of **40**, with compound **46** and 1-chloro-2-iodobenzene. The crude product was used in the next step without further purification. ESI-MS (*m/z*): calcd for C₂₀H₁₇ClO₂ [M+H]⁺ 325.1; found, 325.0.

3-Methoxy-4-(2-methyl-4-nitrophenoxy)benzaldehyde (51)

Vanillin (152.1 mg, 1.0 mmol), 2-fluoro-5-nitrotoluene (155.1 mg, 1.0 mmol), K₂CO₃ (345.5 mg, 2.5 mmol), and 18-crown-6 (10.5 mg) were placed under vacuum in a sealed flask and the flushed with nitrogen gas three times, after which DMF (50 mL) was added to the flask to dissolve the solid material. The reaction mixture was heated to 110 °C and stirred for approximately 3 hr. When

TLC (ethyl acetate/petroleum ether 20%) showed completion of the reaction, the reaction was cooled to rt and washed with water (100 mL) and CH₂Cl₂ (100 mL) three times. The organic layers were combined and evaporated to give the crude product, which was then used in the next step without further purification.

***N*-(3-methoxy-4-(2-methyl-4-nitrophenoxy)benzyl)butan-1-amine (52)**

Acetic acid (0.057 mL, 1.0 mmol) was added dropwise to a solution of **51** (287.3 mg, 1.0 mmol), NaBH₃CN (31.4 mg, 0.50 mmol), and *n*-butylamine (0.15 mL, 1.5 mmol) in THF (25 mL). The reaction was stirred at rt for 2 hr. When TLC (ethyl acetate/petroleum ether 20%) showed completion, the reaction was neutralized with sat. NaHCO₃ solution and washed with water (50 mL) and ethyl acetate (50 mL). The organic layer was dried over MgSO₄ and evaporated to give the crude product. Purification by flash chromatography (ethyl acetate/petroleum ether 10%) gave pure compound **52** as a yellow solid. Yield, 77%; ¹H NMR (400 MHz, CDCl₃): δ 8.10 (d, *J* = 2.4 Hz, 1H), 7.90 (dd, *J* = 9.2, 3.2 Hz, 1H), 7.14 (d, *J* = 2.0 Hz, 1H), 7.01 (d, *J* = 8.0 Hz, 1H), 6.90 (dd, *J* = 8.0, 2.0 Hz, 1H), 6.53 (d, *J* = 9.2 Hz, 1H), 5.23 (br, 1H), 4.25-4.08 (m, 2H), 3.78 (s, 3H), 2.41 (s, 3H), 2.01 (s, 2H), 1.66-1.57 (m, 2H), 1.25-1.18 (m, 2H), 0.86 (t, *J* = 7.2 Hz, 3H) ppm; ¹³C NMR (100 MHz, CDCl₃): δ 161.48, 152.05, 143.98, 142.58, 131.40, 128.66, 126.78, 123.21, 123.01, 122.38, 114.66, 114.25, 57.73, 56.37, 51.97, 30.87, 20.19, 16.54, 13.72 ppm;

1-(3-Methoxy-4-(2-methyl-4-nitrophenoxy)benzyl)piperidine (53)

Compound **53** was obtained using the reductive amination described in the synthesis of compound **52**, using piperidine. Purification by flash chromatography (ethyl acetate/petroleum ether 10%) gave **53** as a yellow solid. Yield, 79%; ^1H NMR (300 MHz, CDCl_3): δ 8.11 (dd, $J = 3.0, 0.9$ Hz, 1H), 7.93 (dd, $J = 9.0, 2.7$ Hz, 1H), 7.06 (d, $J = 1.8$ Hz, 1H), 6.97 (d, $J = 8.1$ Hz, 1H), 6.91 (dd, $J = 8.1, 2.1$ Hz, 1H), 6.56 (d, $J = 9.0$ Hz, 1H), 3.78 (s, 3H), 3.50 (s, 2H), 2.64-2.56 (m, 4H), 2.45 (s, 3H), 1.69-1.50 (m, 4H), 1.48-1.42 (m, 2H) ppm;

3-Methoxy-4-(2-methyl-4-nitrophenoxy)phenyl formate (55)

A solution of compound **51** (2.9 g, 10.0 mmol) and *m*-CPBA (1.7 g, 10.0 mmol) in CH_2Cl_2 (100 mL) was stirred at rt overnight. When TLC (ethyl acetate/petroleum ether 10%) demonstrated that the reaction was complete, the mixture was washed with sat. NaHCO_3 (100 mL) and then water (100 mL). The organic layer was dried over MgSO_4 and evaporated to give the crude product, which was then used in the next step without further purification; ESI-MS (m/z): calcd for $\text{C}_{15}\text{H}_{13}\text{NO}_6$ $[\text{M}+\text{H}]^+$ 304.1; found, 303.0.

3-Methoxy-4-(2-methyl-4-nitrophenoxy)phenol (56)

Compound **55** (3.0 g, 10 mmol) was dissolved in MeOH (80 mL), and sat. K_2CO_3 (40 mL) was added to the solution. The mixture was heated to reflux for 1hr. When TLC (ethyl acetate/petroleum ether 20%) demonstrated that the reaction was complete, the mixture was evaporated to remove MeOH, and the residue was extracted with CH_2Cl_2 (50 mL, 2X). Purification by flash

chromatography (ethyl acetate/petroleum ether 10%) gave pure compound **56** as a bright yellow solid; Yield 80%; ^1H NMR (300 MHz, CDCl_3): δ 8.10 (dd, $J = 3.0, 0.6$ Hz, 1H), 7.92 (ddd, $J = 9.3, 3.0, 0.6$ Hz, 1H), 6.93 (d, $J = 8.7$ Hz, 1H), 6.57 (d, $J = 2.7$ Hz, 1H), 6.52 (d, $J = 9.0$ Hz, 1H), 6.44 (dd, $J = 8.7, 3.0$ Hz, 1H), 5.31 (br, 1H), 3.73 (s, 3H), 2.44 (s, 3H) ppm; ^{13}C NMR (100 MHz, CDCl_3): δ 162.61, 154.47, 152.56, 141.97, 136.8, 128.01, 126.68, 123.31, 123.24, 113.19, 107.36, 101.44, 56.06, 16.54 ppm; ESI-MS (m/z): calcd for $\text{C}_{14}\text{H}_{13}\text{NO}_5$ $[\text{M}+\text{H}]^+$ 276.1; found, 276.0.

2-Methoxy-1-(2-methyl-4-nitrophenoxy)-4-(2-nitrophenoxy)benzene (57)

A solution of **56** (275.3 mg, 1.0 mmol), 1-fluoro-2-nitrobenzene (141.1 mg, 1.0 mmol), K_2CO_3 (345.5 mg, 2.5 mmol), and 18-crown-6 (10.5 mg) in DMF (50 mL) was heated to 110 °C under nitrogen and stirred for approximately 3 hr. When TLC (ethyl acetate/petroleum ether 20%) demonstrated that the reaction was complete, the reaction was cooled to rt and washed with water (100 mL) and CH_2Cl_2 (100 mL) three times. The organic layers were combined and evaporated to give the crude product. Purification by flash chromatography (ethyl acetate/petroleum ether 8%) gave pure compound **57** as a yellow solid; Yield 85%; ^1H NMR (400 MHz, CDCl_3): δ 8.10 (d, $J = 2.4$ Hz, 1H), 7.97-7.92 (m, 2H), 7.54 (td, $J = 7.2, 1.6$ Hz, 1H), 7.25-7.21 (m, 1H), 7.08 (d, $J = 8.4$ Hz, 1H), 7.02 (d, $J = 8.8$ Hz, 1H), 6.78 (d, $J = 2.4$ Hz, 1H), 6.59-6.54 (m, 2H), 3.72 (s, 3H), 2.43 (s, 3H) ppm; ^{13}C NMR (100 MHz, CDCl_3): δ 161.91, 154.18, 152.87, 150.50, 142.37,

141.62, 139.86, 134.48, 128.30, 126.78, 126.39, 126.08, 123.88, 123.30, 120.82, 113.58, 110.20, 105.15, 56.27, 16.55 ppm;

5-Benzyl-2-phenoxyphenol (PT089)

¹H NMR (300 MHz, CDCl₃): δ 7.38-7.31 (m, 4H), 7.27-7.24 (m, 3H), 7.13 (tt, *J* = 7.5, 1.2 Hz, 1H), 7.03 (dd, *J* = 8.4, 1.2 Hz, 2H), 6.92 (d, *J* = 2.1 Hz, 1H), 6.84 (d, *J* = 8.1 Hz, 1H), 6.70 (dd, *J* = 8.4, 2.1 Hz, 1H), 5.56 (s, 1H), 3.96 (s, 2H) ppm; ¹³C NMR (100 MHz, CDCl₃): δ 156.96, 147.35, 141.51, 140.85, 138.14, 129.80, 128.89, 128.47, 126.14, 123.38, 120.94, 118.99, 117.69, 116.63, 41.43 ppm; ESI-MS (*m/z*): calcd for C₁₉H₁₆O₂ [M-H]⁻ 275.1; found, 275.1.

5-Cyclohexyl-2-phenoxyphenol (PT090)

ESI-MS (*m/z*): calcd for C₁₈H₂₀O₂ [M-H]⁻ 267.2; found, 267.1.

5-Benzyl-2-(*o*-tolylloxy)phenol (PT144)

A solution of boron tribromide in CH₂Cl₂ (1.0 M, 1.8 mL, 1.8 mmol) was added dropwise to a solution of **49** (182.6 mg, 0.6 mmol) in dry CH₂Cl₂ (50 mL) at -78 °C. The reaction mixture was stirred under nitrogen for 1 hr, and then the cooling bath was removed. When TLC (ethyl acetate/petroleum ether 5%) demonstrated that the reaction was complete, the reaction was quenched with MeOH (10 mL) and then poured into a sat. NaHCO₃ solution (100 mL). The mixture was extracted with CH₂Cl₂ (50 mL, 3X), and the organic layers were combined and dried over MgSO₄. Purification by flash chromatography (ethyl

acetate/petroleum ether 3%) gave pure **PT144** as white crystals. Yield 88%; ESI-MS (*m/z*): calcd for C₂₀H₁₈O₂ [M-H]⁻ 289.1; found, 289.1.

5-Benzyl-2-(2-chlorophenoxy)phenol (PT158)

The compound was obtained using the demethylation reaction described in the synthesis of **PT144**, using compound **50**. Purification by flash chromatography (ethyl acetate/petroleum ether 4%) gave pure **PT158** as light yellow crystals. Yield 85%; ESI-MS (*m/z*): calcd for C₁₉H₁₅ClO₂ [M-H]⁻ 309.1; found, 309.0.

5-((Butylamino)methyl)-2-(2-methyl-4-nitrophenoxy)phenol (PT182)

A solution of compound **52** (150.0 mg) in AcOH (10 mL) and HBr (44% w/w, 5 mL) was heated to 120 °C and refluxed overnight. When TLC (MeOH/CH₂Cl₂ 5%) demonstrated that the reaction was complete, the mixture was cooled to rt and poured into iced sat. NaHCO₃ (50 mL). The solution was extracted with ethyl acetate (50 mL, 3X), and the organic layers were combined and dried over MgSO₄. Purification by flash chromatography (MeOH/CH₂Cl₂ 5%) gave pure **PT182** as a dark yellow oil. Yield 69%; ¹H NMR (400 MHz, CDCl₃): δ 8.09 (d, *J* = 2.0 Hz, 1H), 7.92 (dd, *J* = 8.8, 2.4 Hz, 1H), 7.11 (d, *J* = 2.0 Hz, 1H), 6.88 (d, *J* = 8.4 Hz, 1H), 6.83 (dd, *J* = 8.0, 2.0 Hz, 1H), 6.71 (d, *J* = 9.2 Hz, 1H), 4.57 (br, 1H), 4.11 (dd, *J* = 13.6, 4.0 Hz, 2H), 2.78-2.71 (m, 2H), 2.38 (s, 3H), 1.66-1.55 (m, 2H), 1.27-1.18 (m, 2H), 0.84 (t, *J* = 7.2 Hz, 3H) ppm; ¹³C NMR (100 MHz, CDCl₃): δ

160.45, 148.54, 143.07, 130.91, 129.54, 127.15, 123.53, 123.32, 122.54, 120.95, 118.69, 115.63, 57.58, 52.38, 27.73, 20.13, 16.58, 13.70 ppm;

2-(2-Methyl-4-nitrophenoxy)-5-(piperidin-1-ylmethyl)phenol (PT183)

A solution of compound **53** (150.0 mg) in AcOH (10 mL) and HBr (44% w/w, 5 mL) was heated to 120 °C and refluxed overnight. When TLC (MeOH/CH₂Cl₂ 10%) demonstrated that the reaction was complete, the mixture was cooled to rt and poured into iced sat. NaHCO₃ (50 mL). The solution was extracted with ethyl acetate (50 mL, 3X), and the organic layers were combined and dried over MgSO₄. Purification by flash chromatography (MeOH/CH₂Cl₂ 7%) gave pure **PT183** as a dark yellow oil. Yield 72%; ¹H NMR (300 MHz, CDCl₃): δ 8.09 (d, *J* = 2.4 Hz, 1H), 7.90 (dd, *J* = 9.3, 2.7 Hz, 1H), 7.37 (br, 1H), 6.89 (d, *J* = 8.4 Hz, 1H), 6.81 (d, *J* = 7.8 Hz, 1H), 6.65 (d, *J* = 9.3 Hz, 1H), 3.71 (s, 2H), 2.72 (br, 4H), 2.40 (s, 3H), 1.75-1.50 (m, 4H), 1.25 (t, *J* = 8.7 Hz, 2H) ppm; ¹³C NMR (100 MHz, CDCl₃): δ 160.99, 148.90, 142.48, 142.42, 130.93, 128.72, 126.58, 123.08, 122.29, 121.15, 119.42, 114.67, 61.82, 53.71, 23.92, 23.05, 16.35 ppm; HRMS (*m/z*): calcd for C₁₉H₂₂N₂O₄ [M+H]⁺ 343.1658; found, 343.1661.

2-(4-amino-2-methylphenoxy)-5-(piperidin-1-ylmethyl)phenol (PT184)

A solution of **PT183** (300 mg), activated zinc powder (400 mg), and NH₄Cl (300 mg) in MeOH (100 mL) was heated to reflux for 30 min. When TLC (MeOH/CH₂Cl₂ 5%) demonstrated that the reaction was complete, the mixture was cooled to rt and filtered through Celite 545. Purification by flash

chromatography (MeOH/CH₂Cl₂ 5%) gave pure **PT184** as a dark yellow solid. Yield 66%; ESI-MS (*m/z*): calcd for C₁₉H₂₄N₂O₂ [M+H]⁺ 313.2; found, 313.3.

2-(2-Methyl-4-nitrophenoxy)-5-(2-nitrophenoxy)phenol (PT440)

The compound was obtained using the demethylation reaction described in the synthesis of **PT144**, with compound **49** as the starting material. Purification by flash chromatography (ethyl acetate/petroleum ether 10%) gave the pure product as a yellow solid; Yield 82%; ¹H NMR (400 MHz, CDCl₃): δ 8.11 (d, *J* = 2.4 Hz, 1H), 7.98 (dd, *J* = 8.8, 3.2 Hz, 1H), 7.94 (dd, *J* = 8.4, 1.6 Hz, 1H), 7.54 (td, *J* = 8.0, 1.6 Hz, 1H), 7.23 (td, *J* = 8.0, 1.2 Hz, 1H), 7.10 (dd, *J* = 8.4, 1.2 Hz, 1H), 6.87 (d, *J* = 8.8 Hz, 1H), 6.78 (d, *J* = 8.8 Hz, 1H), 6.76 (d, *J* = 2.8 Hz, 1H), 6.57 (dd, *J* = 8.8, 2.8 Hz, 1H), 5.57 (br, 1H), 2.43 (s, 3H) ppm; ¹³C NMR (100 MHz, CDCl₃): δ 160.60, 154.09, 150.25, 148.83, 143.26, 141.75, 138.65, 134.54, 129.38, 127.13, 126.06, 124.08, 123.54, 121.22, 115.41, 111.48, 108.08, 107.98, 16.53 ppm;

2-(4-Amino-2-methylphenoxy)-5-(2-aminophenoxy)phenol (PT441)

The compound was obtained using a Clemmensen reduction described in the synthesis of **PT184** with compound **PT440** as the starting material. Purification by flash chromatography (ethyl acetate/petroleum ether 12%) gave pure **PT441** as a brown solid; Yield 74%;

Chapter 3. SAR Studies Focused on the B-Ring of the Diaryl Ethers that Target InhA.

The diaryl ethers directly bind to InhA and potently inhibit both the enzyme activity and bacteria growth. Previous SAR studies showed that hydrophobic substituents on the A-ring are favored in the active site. Modifications were also introduced to the B-ring, resulting in more polar derivatives. However, only **PT070** showed improved binding affinity to InhA and inhibitory activity against *M. tuberculosis*, compared to the parent compounds. To further understand the SAR of the B-ring of diaryl ethers and obtain higher *in vitro* activity, B-ring modified diaryl ethers with more complex structures were synthesized, and their activity was tested with both enzyme and cell based assays.

Background

The Lipinski's Rules

Previously, our group reported a series of diaryl ether compounds that directly inhibit InhA [112]. A representative inhibitor **PT004 (Figure 3.2)** has an IC₅₀ value of 11 nM and an MIC value of 2.1 µg/mL, which are comparable to rifampicin and ethambutol [113]. However, the compound does not show any antimicrobial activity in the short-term model of *M. tuberculosis* infected mice.

An empirical description of structural factors that favor *in vivo* efficacy was summarized by Christopher Lipinski at Pfizer Global Research and Development, after data collection and statistical analysis of thousands of synthetic small-molecule drugs [114]. These rules are known as the “Lipinski’s Rule of Five”, which suggest that drugs should have the following “drug-like properties”:

- 1) No more than 5 hydrogen bond donors.
- 2) No more than 10 hydrogen bond acceptors.
- 3) A molecular weight less than 500 Da.
- 4) A ClogP value lower than 5.

Examination of the structure of **PT004** indicates that this compound meets all Lipinski criteria except ClogP, which has a value of 6.47 and indicates poor drug-like properties. Thus, the first step to improve the *in vivo* efficacy of diaryl ethers is to lower the ClogP values of the diaryl ethers while retaining enzyme binding affinity and MIC values. For this purpose, many modifications were introduced to

the B-ring of the diaryl ethers and their IC_{50} and MIC values were determined (**Table 3.1**) [104]. The results showed that bulky substituents are not tolerated on the B-ring. Even with small substituents, none of these derivatives showed better IC_{50} and MIC values than the parent compound **PT004**. Surprisingly, **PT070** (**Figure 3.2**), with an *ortho* methyl group on the B-ring, had a similar MIC value and a 430-fold higher binding affinity than **PT004** [109]. However, its ClogP (6.8) is even higher than the parent compound. Overall, the *in vitro* activity of the diaryl ethers still needs to be improved, and detailed SAR information for future inhibitor design is not completely clear yet.

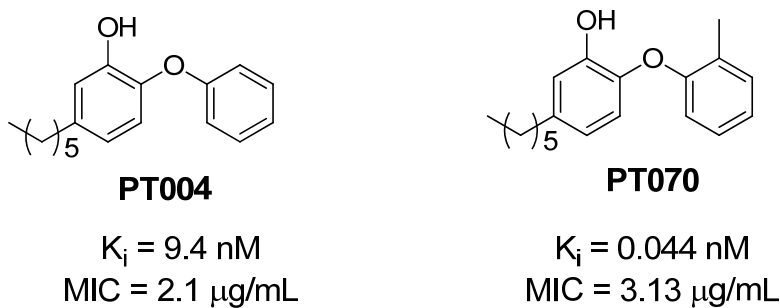


Figure 3.1. The InhA inhibitor PT004 and PT070.

Table 3.1. B-ring modified diaryl ether inhibitors.

Compound	Structure	IC ₅₀ (nM)	MIC (µg/ml)
PT010		100 ± 20	12.50
PT011		48 ± 6	12.50
PT009		90 ± 10	25.0 ± 0
PT013		62 ± 5	3.13
PT014		1090 ± 90	100 ± 0
PT015		55 ± 6	12.50
PT016		1550 ± 460	> 200
PT017		5600 ± 770	100
PT018		1300 ± 200	50.0 ± 0
PT019		2360 ± 200	100.00
PT020		580 ± 40	130 ± 58
PT021		1930 ± 90	> 200
PT028		3220 ± 550	> 200
PT029		1220 ± 60	> 200
PT030		130 ± 34	> 200
PT076		1315 ± 256	
PT067		306 ± 46	> 100
PT040		11,500 ± 1160	50
PT077		236 ± 31	3.13
PT073		160 ± 16	3.13
PT041		8200 ± 98	100.0 ± 0
PT042		650 ± 60	6.25 ± 0

Reproduced from [104].

Design of B-ring Modifications

To continue the search for InhA inhibitors with lower ClogP values and better or higher *in vitro* activity, we need to understand the SAR on the B-ring of the diaryl ether compounds. In this chapter, two questions are addressed:

- 1) What is the role of the methyl group on the B-ring of **PT070** in improving the binding affinity? Will modifications on other positions of the B-ring give better affinity?
- 2) Compared to benzene, will other aromatic rings lower ClogP values and improve *in vitro* activity?

It is postulated that the methyl group of **PT070** provides a higher steric hindrance between the A-ring and the B-ring, which limits the freedom of rotation about the ether bond. This restraint reduces the entropy change during binding of the inhibitor to the enzyme and stabilizes the hydrophobic contacts between the B-ring and Ala198, Met199, Ile202, and Val203 in the substrate binding loop, resulting in high binding affinity. In addition, the *ortho* methyl group on the B-ring may directly interact with Ala198, which also favors inhibitor binding (**Figure 3.2**) [109]. To confirm the importance of steric hindrance, groups with different sizes were attached to the B-ring. In addition, two *ortho* groups were introduced onto the B-ring to further restrict rotation (**Figure 3.3**). To separate the effect of the methyl group as a van der Waals interaction partner from the effect of steric hindrance, substituents with various electrostatic properties, and hydrogen bond

donors and acceptors were chosen to test the necessity of the van der Waals interaction (**Figure 3.3**).

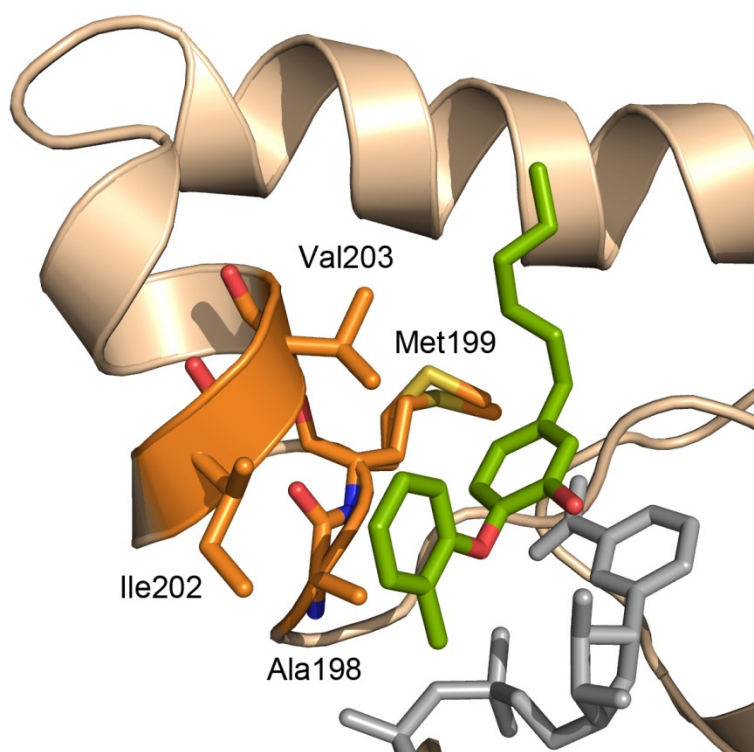


Figure 3.2. Residues interacting with PT070.

In the presence of NAD^+ (gray), **PT070** (green) interacts with Ala198, Met199, Ile202, and Val203 in the active site. The figure was made from 2x22.pdb [109] with PyMol [102].

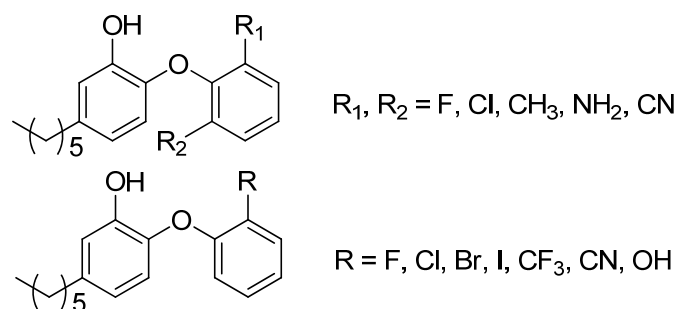


Figure 3.3. PT070 analogs with various groups on the B-ring.

To answer the second question about incorporation of heterocycle B-rings in diaryl ethers, analogs with pyridyl and pyrimidinyl B-rings were designed. Although previous SAR showed that *para* and *meta*-N are well tolerated in pyridyl B-rings, substituted pyridyl B-rings have not been tested yet. Analogs with 1' substituted pyridyl B-rings were designed for three reasons: 1) to combine the SAR of **PT070** and **PT077** for a better binding affinity; 2) to compare 2'-N and 4'-N B-rings; and 3) to lower ClogP values of the diaryl ethers (**Figure 3.4**).

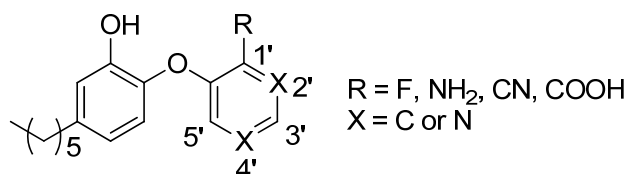


Figure 3.4. Diaryl ethers with heterocyclic B-rings.

A codrug, also known as a mutual prodrug, is a combination of two drugs that have different targets and are chemically linked together to improve drug-like properties [115]. A codrug would bind to both targets, with or without releasing the original two active drugs by metabolic cleavage of the linker between them. Two pyridyl B-ring analogs were designed to mimic the structures of isoniazid and pyrazinamide and should have better MIC values.

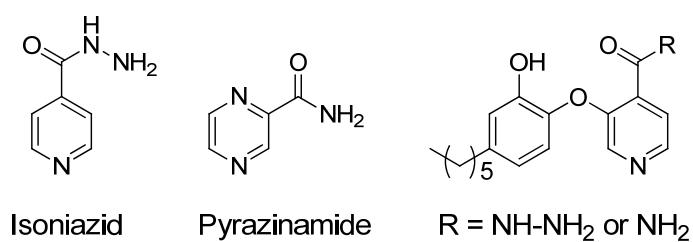
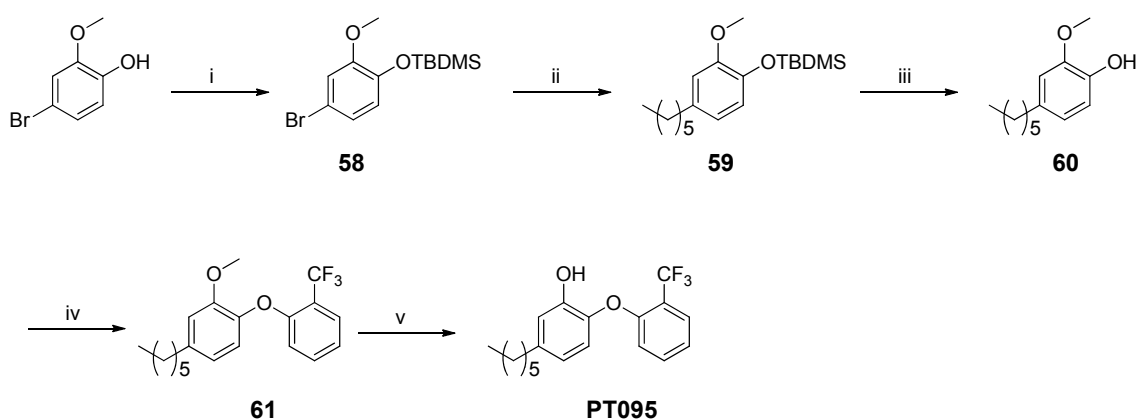


Figure 3.5. A design of codrugs mimicking isoniazid and pyrazinamide.

Synthesis Strategies for B-ring Modified Diaryl Ethers

The previous approaches to the preparation of the diaryl ethers involved a Buchwald-Hartwig cross-coupling to link the A-ring and the B-ring, the attachment of an alkyl group using the Negishi coupling, and the final demethylation step [86, 104]. Compound **PT095** was synthesized using similar conditions (**Scheme 3.1**).

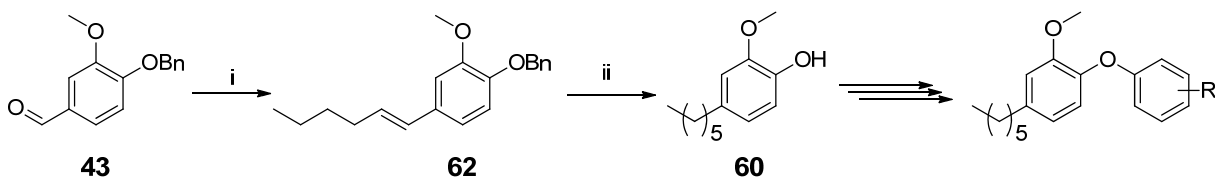


Scheme 3.1. The synthesis of **PT095**.

Reagents and conditions: i) TBDMSCl, imidazole, CH_2Cl_2 , 0 °C, 3 hr, 95%; ii) *n*- $\text{C}_6\text{H}_{13}\text{MgCl}$, ZnCl_2 , 2% $\text{Pd}(\text{P}(t\text{-Bu})_3)_2$, THF/NMP, 130 °C, 48 hr, 74%; iii) AcCl , MeOH, 0 °C, 4 hr, 92%; iv) $(\text{CuOTf})_2 \cdot \text{PhH}$, Cs_2CO_3 , ArCO_2H , EtOAc, toluene, 110 °C, 24 hr, 75%; v) BBr_3 , CH_2Cl_2 , -78 °C to rt, 3hr, 88%.

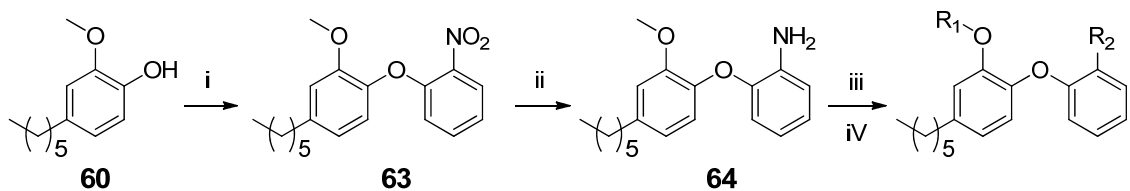
Besides two reactants, the Buchwald coupling reaction employs three catalysts or additives, including the expensive copper complex $(\text{CuOTf})_2 \cdot \text{PhH}$, and a mixture of two solvents to keep the solution homogeneous. Obviously, reaction setup is complicated, the cost is high, and it takes 12-26 hours to reach complete conversion. Moreover, the B-ring reactant is limited to phenyl bromides and iodides. The reaction gives very low yields or does not happen at all when

heterocycles are used as B-ring reactants [116]. There are also similar issues for the Negishi coupling: expensive, unstable catalyst, complex setup, and long reaction time [117].



Scheme 3.2. Synthesis of compound 60.

Reagents and conditions: i) BnBr, KOH (5% aq), MeOH, reflux, 2 hr, 91%; (ii) *n*-C₅H₁₁PPh₃Br, *n*-BuLi, CH₂Cl₂, -78 °C to rt, 3 hr, 82%; (iii) H₂, Pd/C, EtOH, 6 hr, 89%.



65: R ₁ = Me, R ₂ = Cl	PT091: R ₁ = H, R ₂ = Cl
66: R ₁ = Me, R ₂ = Br	PT092: R ₁ = H, R ₂ = Br
67: R ₁ = Me, R ₂ = I	PT096: R ₁ = H, R ₂ = I
68: R ₁ = Me, R ₂ = CN	PT119: R ₁ = H, R ₂ = CN

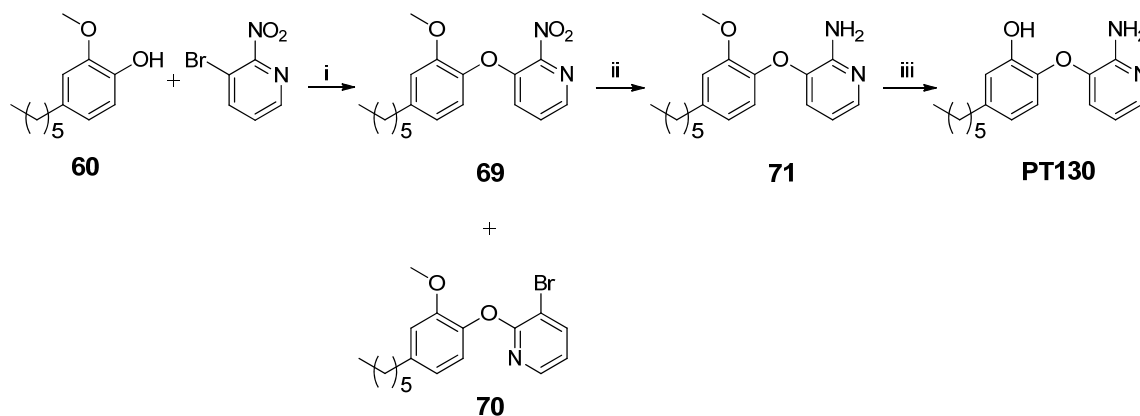
Scheme 3.3. Synthesis of compound PT091, PT092, PT096, and PT119.

Reagents and conditions: i) K₂CO₃, 1-fluoro-2-nitrobenzene, 18-crown-6, DMF, 110 °C, 2 hr, 86%; ii) H₂, Pd/C, EtOH, 6 hr, 90%; or Zn, NH₄Cl, MeOH, reflux, 0.5 hr, 78%; iii) NaNO₂, AcOH, H₂O, 0 °C, 30 min; iv) BBr₃, CH₂Cl₂, -78 °C to rt, 3 hr.

Consequently, a new scheme was established to make the key intermediate **60**, which facilitated synthesis for most of the analogs. Starting from compound **43** (Scheme 2.2), a Wittig reaction was used to introduce a hexyl group on the A-

ring, resulting in compound **62**. The following hydrogenation reduced the double bond and simultaneously removed the protecting group to give compound **60** (Scheme 3.2).

Once compound **60** was obtained, 1-fluoro-2-nitrobenzene was coupled to the phenol to provide the intermediate **63**, which was then reduced to the amino intermediate **64**. Diazotization of aniline **64** and substitution with various inorganic anions gave compounds **65-68**. Finally, demethylation with BBr_3 gave the corresponding final compounds **PT091**, **PT092**, **PT096**, and **PT119** (Scheme 3.3). This method avoids the use of complex Buchwald and Negishi coupling reactions, and facilitates diversity-oriented synthesis for B-ring analogs of **PT070**. In addition, large scale synthesis of compound **60** becomes possible for *in vivo* efficacy evaluation in animal models.



Scheme 3.4. Synthesis of compound **PT130**.

Reagents and conditions: i) K_2CO_3 , 18-crown-6, DMF, 110°C , 2 hr, 46%; ii) Zn, NH_4Cl , MeOH, reflux, 0.5 hr, 77%; iii) BBr_3 , CH_2Cl_2 , -78°C to rt, 3 hr, 79%.

A similar method was used to synthesize **PT130**, with 3-bromo-2-nitropyridine as the starting material. The coupling reaction gave a mixture of compound **69** and **70** at a ratio about 1:1, resulting in a low yield. Compound **69** was separated by column chromatography and used in the following steps (**Scheme 2.4**). Clemmensen reduction was used to reduce **69** to **71**, while a similar method was used with phenyl B-rings were achieved with hydrogenation. In fact, both reactions worked for phenyl B-rings; hydrogenation was preferred because it gave a higher yield than the Clemmensen reduction, although it requires a longer reaction time (**Scheme 3.3**). For the synthesis of **PT130**, Clemmensen reduction was used because the pyridine ring may coordinate to palladium charcoal and deactivate the catalyst.

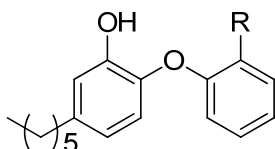
Results and Discussion

Analogs with Mono B-ring Substituents

Lead compound **PT004** [86], **PT010** [104], **PT013** [104], and **PT070** [109] have been reported in previous SAR studies. Compared to **PT004**, **PT070** showed significantly improved binding affinity, which was thought to result from reduced freedom of rotation about the ether bond together with increased hydrophobic contacts between the B-ring and Ala198, Met199, Ile202, and Val203 in the substrate binding loop. Introduction of an *ortho* methyl group on the B-ring also resulted in an additional interaction between the methyl group and Ala198. Interestingly, the amino substituted analog (**PT013**) had similar IC₅₀ and MIC values compared to **PT070**, which questions the importance of van der Waals interactions between the methyl and Ala198. Consequently, to understand the role of the methyl group in increased binding affinity and improved *in vitro* activity, analogs with various *ortho* substituents were synthesized and evaluated (**Table 3.2**).

IC₅₀ values were first determined with 100 nM InhA. Since the lowest IC₅₀ value that can be measured is half the enzyme concentration, compounds with IC₅₀ values around 50 nM were evaluated at lower InhA concentrations. Most analogs are tight-binding inhibitors, with IC₅₀ values in a narrow range (< 60 nM). To compare their binding affinities more accurately, K_i values of selected compounds were also measured.

Table 3.2. Derivatives with *ortho* substituent groups on the B-ring.



Compound	R	IC ₅₀ (nM)	MIC (µg/mL)	K _i (nM)
	PT004^a	-H	11 ± 1 ^d	2.1
PT010^b	-NO ₂	182 ± 2.0 ^e	12.50	N.D. ^g
PT013^b	-NH ₂	61.9 ± 4.5 ^e	3.13	N.D. ^g
PT070^c	-CH ₃	50.7 ± 4 ^e	3.13	0.044 ± 0.005
PT091	-Cl	49.5 ± 2.2 ^e	1.56	0.96 ± 0.14
PT092	-Br	10.0 ± 0.8 ^f	3.125	0.20 ± 0.05
PT095	-CF ₃	29.7 ± 1.2 ^f	50.00	N.D. ^g
PT096	-I	44.6 ± 7.5 ^e	25	3.72 ± 5.13
PT113	-F	12.1 ± 4.8 ^f	1.56	0.09 ± 0.02
PT114	-OH	48 ± 3 ^e	12.5	15.9 ± 3.7
PT119	-CN	235.6 ± 10.0 ^e	2.5	2.14 ± 0.35

a Data taken from [86].

b Data taken from [104].

c Data taken from [109].

d IC₅₀ value was determined with enzyme concentration of 1 nM.

e IC₅₀ value was determined with enzyme concentration of 100 nM.

f IC₅₀ value was determined with enzyme concentration of 20 nM.

g N.D. = Not determined.

The results indicated that the methyl group is like appropriate size for efficiently binding. Previously, we proposed that B-ring substituents should generally be small in order to be accommodated in the InhA active site [104], and this observation is confirmed by current data. Indeed, the binding affinity is even more sensitive to substituent size than we originally recognized. In particular, introduction of -CF₃ or -CN groups into the B-ring resulted in 50-100 folds weaker binding affinities.

The introduction of polar groups such as -OH (**PT114**) or -NH₂ (**PT013**) resulted in higher K_i and IC₅₀ values, which indicates that hydrophobic interactions between the *ortho* group and protein are critical. On the other hand, halogens, which act as hydrogen bonding acceptors while preserving van der Waals interactions, are well tolerated. They showed similar binding and inhibitory activities compared to the parent compounds, which implies that both van der Waals contact and hydrogen bonds favors binding to the active site. A group that balances both interactions can give similar or better activities (**PT113**). Among the B-ring substituents, a correlation between the binding affinity and electronegativity was not observed, suggesting that electronegativity is not a major factor affecting in binding.

These results confirmed that an *ortho* substituent is necessary for high affinity binding, and that this group should be small (containing one or two heavy atoms) and not a hydrogen bond donor. **PT013** has a MIC value for *M. tuberculosis* 4

folds lower than **PT114**, which, we speculate, could be a result of improved cell permeability caused by the amino group.

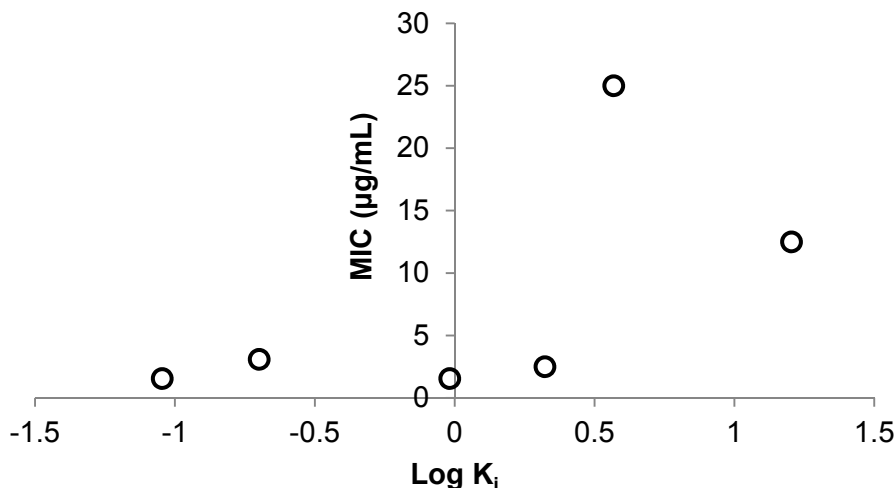


Figure 3.6. The correlation between MIC and K_i values.

The semilog plot of MIC against K_i , made from data in **Table 3.2**, shows that enzyme binding affinity and cell growth inhibition are generally correlated.

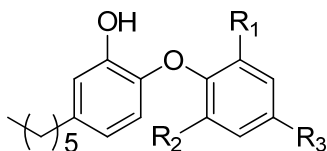
Finally, MIC and K_i values of selected compounds were shown in a semilog plot to confirm that they are correlated to each other (**Figure 3.6**). The correlation is expected for inhibitors that target the same enzyme, because both MIC and K_i values are mainly determined by the free energy of binding. Interestingly, MIC values seem to remain above 2 $\mu\text{g/mL}$ even when K_i values decreased by 200 fold from 9 nM to 0.04 nM. One possible reason is that MIC measurement could be affected by many cofactors, such as cell uptake, solubility, and compound stability, therefore, a lower limit of MIC for this series of compounds implies an effect of cell uptake or penetration for compounds sharing this scaffold. On the

other hand, more accurate measurement of MIC values of **PT070** and **PT113** may be helpful either to a better correlation or to confirm the limit of MIC values for these compounds. In addition, determination of the K_i value of **PT095** would also give a better correlation by extend the range of data points.

Analogs with di-Substituted B-rings

Given that restricting rotation about the ether linkage is an efficient approach to improving the binding affinity, a series of di-*ortho* substituted B-rings, which are more conformational restricted, were synthesized. An *ortho, para* di-substituted B-ring analog **PT107** was also synthesized to test the tolerance of di-substitution (**Table 3.3**).

Table 3.3. Derivatives with di-substituted B-ring.



Compound	R			IC ₅₀ (nM)	MIC (µg/mL)	K _i (nM)
	R ₁	R ₂	R ₃			
PT004^a	-H	-H	-H	11 ± 1 ^a	2.1 ± 0.9	9.4 ± 0.5
PT070^b	-CH ₃	-H	-H	50.7 ± 4	3.125	0.044 ± 0.005
PT099	-CH ₃	-NO ₂	-H	N/A ^b	>100	N.D. ^c
PT107	-CH ₃	-H	-NO ₂	50±5	6.25	0.13 ± 0.03
PT108	-CH ₃	-CH ₃	-H	1570 ± 200	100	N.D. ^c
PT109	-Cl	-Cl	-H	86 ± 6	25	N.D. ^c
PT110	-CH ₃	-NH ₂	-H	N/A ^b	>100	N.D. ^c
PT111	-F	-CN	-H	100±9	25	N.D. ^c
PT131	-C(NH)NH ₂	-F	-H	N/A ^b	N.D. ^c	N.D. ^c
PT133	-F	-Cl	-H	79.7 ± 24.4	25	N.D. ^c

^a Data taken from [86].

^b Data taken from [109].

^c IC₅₀ value was determined with enzyme concentration of 1 nM.

^d No significant inhibitory activity at 2000 nM.

^e N.D. = Not determined due to poor IC₅₀ values.

Unfortunately, none of the derivatives (**Table 3.3**) gave better activity than their parent compounds (**Table 3.2**). To rationalize these results the docked structure of the di-chloro analogue **PT109** was compared with the corresponding structure of the mono-chloro compound **PT091** bound to InhA (**Figure 3.7**). This analysis demonstrated that **PT109** has a higher Grid score, van der Waals, and internal energy than **PT091**, which explains its weak binding affinity (**Table 3.4**). The extra steric hindrance resulted in unfavorable van der Waals interactions and thus lowered its binding affinity.

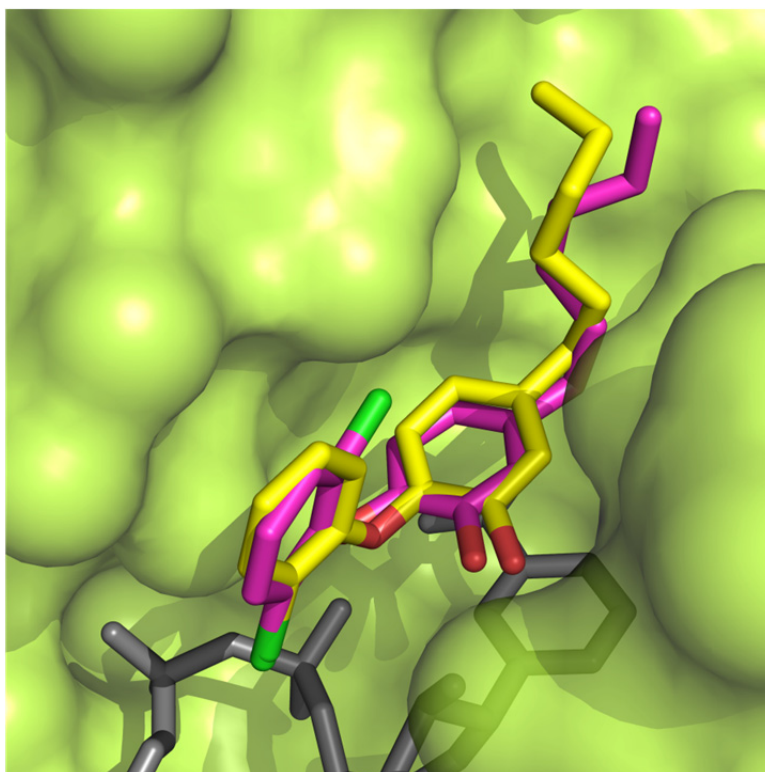


Figure 3.7. PT091 and PT109 docked into the active site of InhA.

PT091 (yellow) and **PT109** (magenta) were docked into the InhA active site (lime) with NAD⁺ cofactor (gray). The figure was generated with PyMol [102].

Table 3.4. Docking results of PT091 and PT109 with InhA.

Compound	Grid Score	Grid_vdw	Grid_es	Internal
PT091	-73.26	-70.23	-3.03	10.24
PT109	-54.53	-52.43	-2.10	20.29

Notably, among all *ortho* di-substituted analogs, halogens on the B-ring gave the best activity (**PT109** and **PT111**), which is consistent with the observation of mono-substituted B-rings.

The analog with an *ortho*, *para* di-substituted B-ring (**PT107**) has an IC₅₀ value 4 folds higher than **PT070** and a comparable MIC value. The result implies that small *para* groups on the B-ring are well tolerated, which is consistent with previous data (**Table 3.1**).

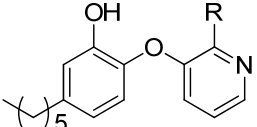
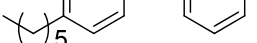
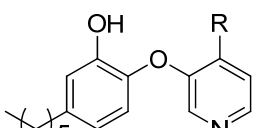
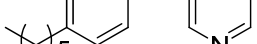
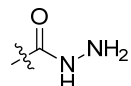
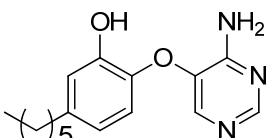
Analogues with Heterocyclic B-rings

In order to lower the ClogP values of the diaryl ethers we also explored analogues with heterocyclic B-rings [104]. Previous SAR studies showed that introduction of an *ortho* nitrogen atom into the B-ring reduced activity significantly, while *para* and *meta* nitrogen atoms were well tolerated (**Table 3.1**). However, the position of the *meta* nitrogen is ambiguous for an unsubstituted B-ring. To differentiate 2' and 4' nitrogen (**Figure 3.5**), the B-ring of the diaryl ethers were modified to include 1' substituted pyridines and pyrimidines (**Table 3.5**). Based on the SAR of *ortho* substituted phenyl B-rings, -F, -CN, and -NH₂

were attached to the 1'-carbon of the B-ring, representing small hydrogen bonding acceptors, medium hydrogen bonding acceptors, and small hydrogen bonding donors, respectively.

The results showed similar SAR to phenyl B-rings: **PT161** with *ortho* fluorine showed the lowest IC₅₀ and MIC values, followed by -CN (**PT164**), while -NH₂ (**PT130**) is the least active 2'-N analog. Interestingly, all 2'-N analogs are much more potent than 4'-N analogs (**PT112**, **PT115**, **PT137**, and **PT139**). In addition, the presence of both 2'- and 4'-N in the B-ring gave slightly higher IC₅₀ and MIC values than the corresponding 2'-N analogue (**PT134**). The X-ray crystallographic structure of **PT070** bound to InhA (2x23.pdb) [109] was used to identify potential differences in the interactions of 2'- and 4'-N analogs with the enzyme. This analysis revealed that although the 2'- and 4'-N atoms have similar hydrophobic contacts with Ile202 and Met161, 2'-N could have additional hydrogen bonding with the backbone amide of Phe97, thus stabilizing the bound inhibitor (**Figure 3.8**). Thus, van der Waals interaction is favorable at 4' of the B-ring, and hydrogen bonding is more favorable at 2' of the B-ring.

Table 3.5. Derivatives with heterocycle B-rings.

Compound	R	IC ₅₀ (nM) ^a	MIC (µg/mL)	
	PT077	-H	190 ± 12	3.13
PT130		-NH ₂	157.0 ± 18.9	0.78
PT164		-CN	308 ± 4.2	<0.39
PT161	-F	40 ± 20	0.3125	
PT112	-NH ₂	69000 ± 700	50	
PT115	-CN	890.6 ± 105.8	12.5	
PT116		-COOH	N/A ^b	25
PT137		-CONH ₂	N/A ^b	>100
PT139		N/A ^b	6.25	
PT134			238.8 ± 46.8	3.125

^a IC₅₀ value was determined with enzyme concentration of 100 nM.

^b N/A = No significant activity observed at 2000 nM.

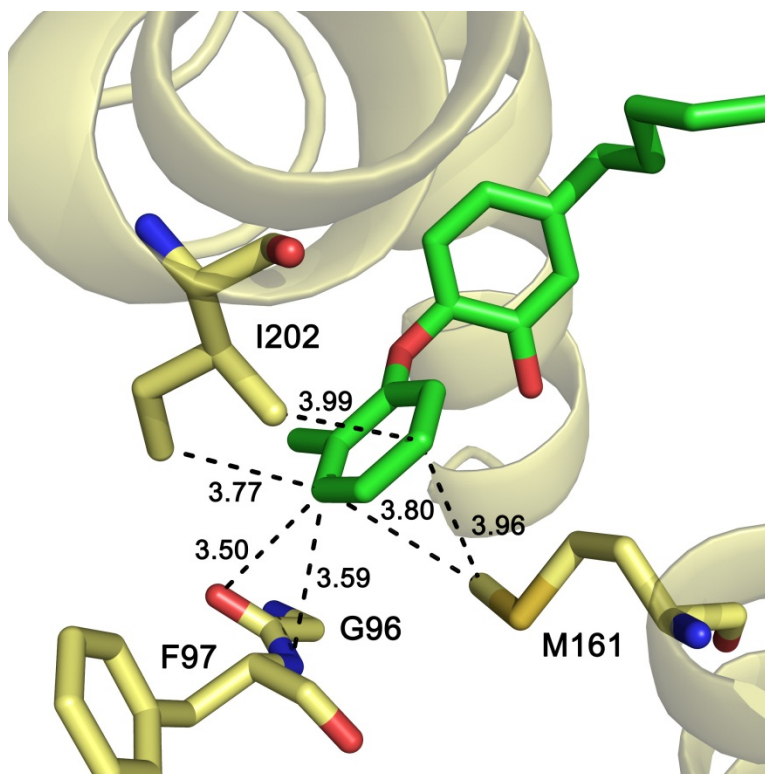


Figure 3.8. Analysis of interactions around the B-ring of PT070.

Possible hydrophobic and hydrogen bonding interactions within 4 Å of the 2'- and 4'- positions of the B-ring. The figure was made from the crystallographic structure of **PT070** (green) bound to InhA.(2x23.pdb) [109] with PyMol [102].

The poor MIC values for the 4'-N pyridyl compounds is consistent with the relatively weak affinity of these inhibitors for InhA, while the 2'-N pyridyl compounds gave much lower MIC values than **PT070**. Considering both the ClogP values and antibacterial activity, the pyridinyl B-ring is a better scaffold than a phenyl B-ring.

Using B-rings that mimicked pyrazinamide and isoniazid, compound **PT137** and **PT139** were synthesized to test the possibility of codrugs incorporating diaryl

ether scaffolds. However, the compounds did not show significant activity against InhA *in vitro*, which is reasonable because the amide or hydrazide may be too large for the compounds to bind to InhA, while isoniazid and pyrazinamide need activation by intracellular enzymes. Further tests found that **PT137** had no activity against *M. tuberculosis* growth, which indicates that this design is not successful, probably because the structure is not the same as either pyrazinamide or isoniazid and cannot be activated by endogenous enzymes. **PT139** has an MIC value of 6.25 $\mu\text{g/mL}$, which is acceptable but not impressive compared to the top diaryl ethers. Although the codrug **PT139** becomes active inside of the cell, the data indicated that the diaryl ether codrugs do not have synergistic activity, so it may not be a promising strategy.

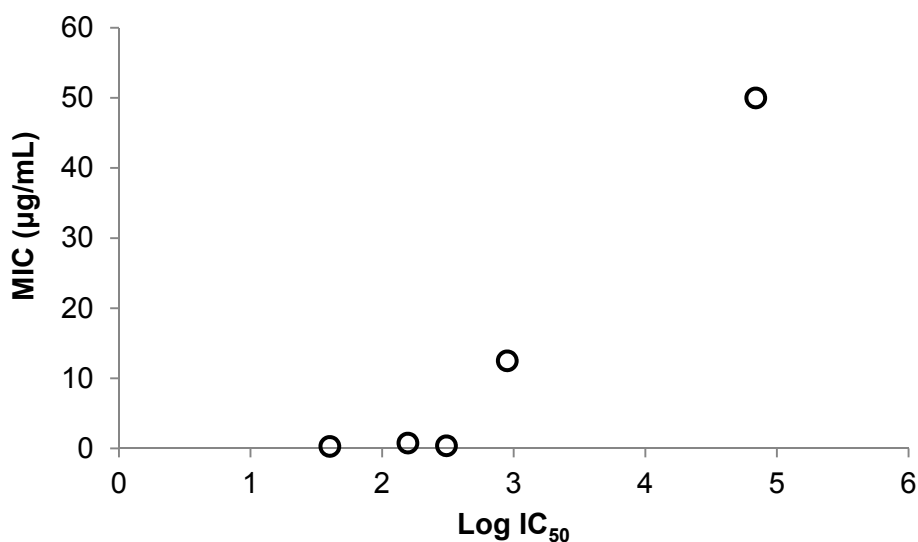


Figure 3.9. MIC and K_i values of the pyridyl diaryl ethers.

The semilog plot of MIC and IC_{50} values for selected compounds in **Table 2.5**. The data showed the correlation between MIC and IC_{50} values and a plateau of MIC.

MIC and IC₅₀ values of selected compound with pyridyl B-rings were showed in a semilog plot to show the correlation between MIC and IC₅₀ values (**Figure 3.9**). Similar to the diaryl ethers with phenyl B-rings (**Figure 3.6**), the data showed a general correlation between MIC and IC₅₀ values, which confirms that they target InhA to inhibit cell grow. Furthermore, a lower limit of MIC around 0.3 µg/mL was also found for this series of compounds, which could be determined by cell permeability. We noticed that the phenyl and pyridyl diaryl ethers showed the MIC plateau around 2 and 0.3 µg/mL, respectively, which implies an effect of cell penetration because it is usually scaffold specific. More accurate measurement of MIC values for **PT130**, **PT161**, and **PT164** would be helpful to examine this hypothesis.

Activities against Nonreplicating M. tuberculosis.

The mode of action indicates that isoniazid is active only against replicating *M. tuberculosis* [118], because both the KatG enzyme and the fatty acid biosynthesis keep a low activity in nonreplicating *M. tuberculosis*. Low-oxygen-recovery assays (LORA) [119] were performed for the diaryl ethers to find if they lose the activities against nonreplicating *M. tuberculosis* (**Table 3.6**). **PT070**, **PT091**, and **PT119** showed MIC values that are much lower than isoniazid and comparable to moxifloxacin, but the activities are poorer than rifampicin and streptomycin.

Table 3.6. Activities of InhA inhibitors against nonreplicating *M. tuberculosis*.

Compound	MIC ($\mu\text{g/ml}$)
PT070	47.2
PT091	24.1
PT119	38.5
PT130	> 50 (56% ^b)
PT166 ^a	> 50 (79% ^b)
Rifampicin	0.40
Isoniazid	> 128 (66% ^b)
Moxifloxacin	43.3
Streptomycin	0.68

^a The compound will be discussed in Chapter 4.

^b Inhibition percentage at 50 $\mu\text{g/ml}$.

General Binding Model for InhA

The work on the A-ring and B-ring modifications revealed some SAR for the diaryl ethers binding to InhA. For future design of more potent inhibitors, this work was extended a little to include other InhA inhibitors by literature search. The X-ray crystallographic structures InhA complexes with two triclosan molecules [88], **PT003** [86], C16-NAC [101], compound **20** [103], **Genz-10850** [88], compound **72** [87], and **73** [90] (**Figure 3.10**) were superimposed (**Figure 3.11**). Comparison of the structural data enables a common binding mode for InhA inhibitors to be elucidated [120].

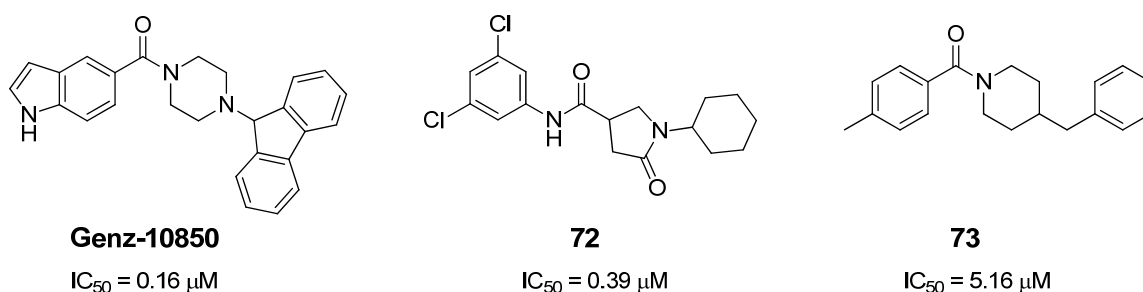


Figure 3.10. Structures of InhA inhibitors

InhA inhibitors **Genz-10850** [88] and compound **72** [87] and **73** [90].

Of key importance for inhibitor binding is the formation of a hydrogen bonding network between a polar group on the inhibitor, Tyr158, and the 2'-hydroxyl on the nicotinamide ribose. Inhibitors with hydrogen bonding (HB) functionalities such as hydroxyl or carbonyl groups participate in this network [77, 88, 94, 121, 122]. In addition, since the natural substrates for InhA are significantly longer

than for other FabI enzymes (24-56 carbons in length, [123]), the substrate binding loop in InhA is also larger, thereby enabling inhibitors with bulky hydrophobic groups such as fluorene to bind. Extensive hydrophobic contacts in this area include Met103, Gly104, Phe149, Ala157, Ala198, Met199, Ile202, Ile215, and Leu218 [88, 124, 125]. Finally, a third binding area can be identified close to the hydrogen bonding group in the inhibitor. This binding pocket is relatively constrained in size (size limited) and is also exposed to solvent as well as being close to polar groups such as the cofactor phosphodiester bridge and non-polar groups in the substrate binding loop (e.g. Ala198). Not surprisingly then, the SAR data shows that enzyme inhibition is highly sensitive to the chemical nature and size of the inhibitor substituent at this position, and groups that are small and that can also participate in both polar and non-polar contacts are preferred.

This information may be used for future studies to optimize inhibitor affinity whilst at the same time engineering the compounds to reduce metabolic liabilities, improve compound ADME and enhance bioactivity.

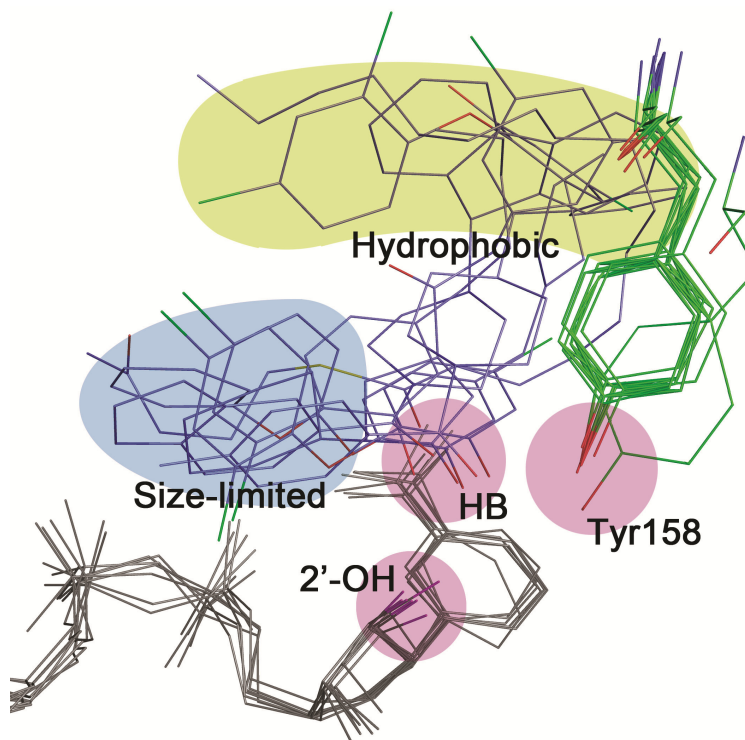


Figure 3.11. Common binding mode for InhA inhibitors.

Seven structures have been overlaid in which InhA is in complex with: two triclosan molecules (1p45.pdb), **PT003** (2b36.pdb), C16-NAC (1bvr.pdb), compound **20** (3fng.pdb), **Genz-10850** (1p44.pdb), compound **72** (2h7m.pdb), and **73** (2nsd.pdb). Key areas of interaction are highlighted and include groups involved in the hydrogen bond (HB) network (pink), the hydrophobic pocket (yellow), and the region surrounded by both polar and nonpolar groups (size-limited, slate).

Summary

Twenty one compounds were synthesized based on the diaryl ether scaffold, with a hexyl-substituted A-ring and various modifications to the B-ring. All the compounds were tested for enzyme inhibition and cell based antibacterial activity.

The activity of the diaryl ether compounds is highly sensitive to the group size of *ortho* substituents on the B-ring. Once the group has more than two heavy atoms, the activity will be considerably depressed. In addition, while van der Waals interactions are impartial, non-hydrogen bonding donors also favor the enzyme-inhibitor complex formation.

Introduction of groups to both *ortho* positions resulted in a loss of activity which, according to docking studies, led to high internal energy, and unfavored the van der Waals interactions with the enzyme. The *ortho*, *para* di-substituted compound **PT107** showed similar activity to that of the parent compound, suggesting that small *para* groups on the B-ring are well tolerated.

Pyridyl B-rings showed similar SAR as the diphenyl ethers. In addition, we were able to distinguish 2'-N and 4'-N pyridyl B-ring analogs by introducing 1' substituents on the B-ring. The 2'-N pyridyl B-rings resulted in higher activity than the 4'-N. Compared to diphenyl ethers, lower MIC values can also be due to the improvement in drug-like properties. Codrugs mimicking pyrazinamide and isoniazid did not show promising MIC values, which gives this drug design a low priority in future studies.

Organic Synthesis

Synthesis of final compounds **PT091**, **PT092**, **PT095**, **PT096**, **PT119**, **PT130**, and necessary intermediates is described in this section. Other compounds were synthesized by our postdoctoral scientist Dr. Gopal B. Reddy and Sai Advantium Pharma Ltd., India (**Table 3.7**). All commercially available chemicals and solvents were used without further purification. All new compounds gave satisfactory spectroscopic and/or analytical data. ^1H and ^{13}C NMR spectra were recorded at 300 or 400 MHz, and chemical shifts are reported in parts per million (δ) downfield from the internal standard tetramethylsilane (TMS). Mass spectra were obtained using electrospray (ES) ionization techniques. General procedures of aromatic nucleophilic substitution, diazotization, and demethylation are given below.

Table 3.7. Contributors for synthesis of the diaryl ethers.

Compound	Synthesis performed by
PT091	Pan Pan
PT092	Sai Advantium Pharma Ltd. and Pan Pan
PT095	Pan Pan
PT096	Pan Pan
PT099	Sai Advantium Pharma Ltd.
PT107	Sai Advantium Pharma Ltd.

Table 3.7. Contributors for synthesis of the diaryl ethers.

Compound	Synthesis performed by
PT108	Sai Advantium Pharma Ltd.
PT109	Sai Advantium Pharma Ltd.
PT110	Sai Advantium Pharma Ltd.
PT111	Sai Advantium Pharma Ltd.
PT112	Sai Advantium Pharma Ltd.
PT113	Sai Advantium Pharma Ltd.
PT114	Sai Advantium Pharma Ltd. and Dr. Gopal B. Reddy
PT115	Sai Advantium Pharma Ltd.
PT116	Sai Advantium Pharma Ltd.
PT119	Pan Pan
PT130	Sai Advantium Pharma Ltd. and Pan Pan
PT131	Sai Advantium Pharma Ltd.
PT133	Sai Advantium Pharma Ltd.
PT134	Sai Advantium Pharma Ltd.
PT137	Sai Advantium Pharma Ltd.
PT139	Sai Advantium Pharma Ltd.
PT161	Dr. Gopal B. Reddy
PT164	Dr. Gopal B. Reddy

The general procedure for the aromatic substitution reaction

A solution of a phenol (1.03 mmol), a nitrobenzene (1.03 mmol), K_2CO_3 (1.03 mmol), and a catalytic amount of 18-crown-6 ether in DMF (3 mL) was heated to 110 °C for 3 hr. After TLC showed completion, the reaction mixture was diluted with water (20 mL) and extracted with ethyl acetate (20 mL, 2X). The organic layer was washed with brine, dried over anhydrous sodium sulfate, and concentrated under reduced pressure. The crude product was purified by column chromatography to afford substituted nitrobenzene in various yields.

The general procedure of diazotization

The reactant aniline (1 mmol) was dissolved in AcOH (10 mL) and water (100 mL) and cooled to -10 °C. $NaNO_2$ (103.9 mg, 1.5 mmol) was added slowly, followed by corresponding halides (1.5 mmol) after 30 min. The ice bath was removed, and the reaction was stirred for approximately 2 hr. The reaction mixture was extracted with CH_2Cl_2 (250 mL) and H_2O (150 mL). The organic layer was dried over $MgSO_4$ and concentrated to give the crude product.

The general procedure of demethylation

The reactant methoxybenzene (0.627 mmol) was dissolved in dry CH_2Cl_2 (50 mL), and BBr_3 (0.94 mL, 2M in CH_2Cl_2 , 1.88 mmol) was added dropwise at -40°C. The reaction was gradually warmed to rt and stirred for 3 hr. When TLC showed completion, the reaction was cooled to -40°C and quenched with MeOH. The solution was concentrated to give the crude product.

(4-Bromo-2-methoxyphenoxy)(tert-butyl)dimethylsilane (58)

A solution of 4-bromo-2-methoxyphenol (2.0 g, 10.0 mmol) and imidazole (0.68 g, 10.0 mmol) in CH₂Cl₂ (50 mL) was cooled to 0 °C, and TBDMSCI (1.5 g, 10.0 mmol) was added into the solution. The reaction was stirred at 0 °C for 3 hr. When TLC (ethyl acetate/petroleum ether 5%) showed completion, the reaction was washed with sat. NaHCO₃ (50 mL) and sat. CuSO₄ (50mL, 2X). The organic layer was dried over MgSO₄ and evaporated to give the crude product, which was used in the next step without further purification; Yield 95%.

***Tert*-butyl(4-hexyl-2-methoxyphenoxy)dimethylsilane (59)**

A solution of benzyl magnesium chloride in THF (2.0 M, 0.6 mL, 1.2 mmol) was dropwise added to a solution of ZnCl₂ in THF (1.0M, 1.2 mL, 1.2mmol), and NMP (15 mL) was added after 20 minutes, followed by Pd[P(t-Bu)₃]₂ (10.2 mg, 0.02 mmol) and **58** (317.3 mg, 1.0 mmol). The reaction was stirred at 130°C for 48 hr. When TLC (ethyl acetate/petroleum ether 5%) showed completion of the reaction, the mixture was washed by Et₂O (20 mL, 3X), and the organic layer was wash by water (50mL, 2X). Purification by flash chromatography (ethyl acetate/petroleum ether 4%) gave the pure compound **59** as a colorless liquid; Yield 74%.

4-Hexyl-2-methoxyphenol (**60**)

Activated palladium on carbon (40 mg) was added into a solution of **62** (800 mg) in ethanol (100 mL). The reaction was stirred under hydrogen for 6 hr and then filtered. The filtrate was evaporated to give the crude product. Purification by flash chromatography (ethyl acetate/petroleum ether 5%) gave pure **60** as a colorless liquid; Yield 89%; ^1H NMR (400 MHz, CDCl_3): δ 6.80 (d, $J = 6.0$ Hz, 1H), 6.65-6.63 (m, 2H), 5.42 (s, 1H), 3.85 (s, 3H), 2.50 (t, $J = 5.7$ Hz, 2H), 1.56-1.54 (m, 2H), 1.30-1.27 (m, 6H), 0.86 (t, $J = 5.1$ Hz, 3H); ^{13}C NMR (100 MHz, CDCl_3) ppm: δ 146.47, 143.68, 135.15, 121.09, 114.26, 111.13, 56.06, 35.87, 31.98, 31.95, 29.17, 22.82, 14.29 ppm; ESI-MS (m/z): calcd for $\text{C}_{13}\text{H}_{20}\text{O}_2$ $[\text{M}+\text{H}]^+$ 209, found 209; $[\text{M}-1]^-$ 207, found 207.

4-Hexyl-2-methoxy-1-(2-(trifluoromethyl)phenoxy)benzene (**61**)

Reagents 1-iodo-2-(trifluoromethyl)benzene (2.0 g, 7.35 mmol), vanillin (1.1 g, 7.35 mmol), Cs_2CO_3 (10.5 g, 32.3 mmol), $(\text{CuOTf})_2\cdot\text{PhH}$ (185.0 mg, 0.37 mmol, 5.0 mol % Cu), and 1-naphthoic acid (5.56 g, 32.3 mmol) were dissolved in ethyl acetate (1 mL) and toluene (75 mL) in an oven-dried 50 mL two-necked round-bottomed flask. Molecular sieves 4 Å (1.8 g) were added into the flask while nitrogen gas is flushing, and then the flask was sealed with a septum and heated to 120 °C under nitrogen. After 24 hr stirring, upon cooling to rt, CH_2Cl_2 was added and the organic phase was obtained by filtration. This solution was washed with 5% NaOH. The aqueous layer was then extracted with CH_2Cl_2 and the combined organic layers were washed with brine, dried over Mg_2SO_4 and

concentrated under vacuum to give the crude product, which was then purified by flash chromatography on silica gel (4% ethyl acetate/hexane) to give pure **61** as a light yellow liquid. Yield 75%; ESI-MS (m/z): calcd for $C_{20}H_{23}F_3O_2$ $[M+H]^+$ 353.2; found, 353.2.

1-(Benzyloxy)-4-(hex-1-en-1-yl)-2-methoxybenzene (**62**)

A solution of *n*-BuLi (2.0 M, 2.45 mL, 4.9 mmol) in cyclohexane was added dropwise to a solution of *n*-pentyl-triphenylphosphonium bromide (2.0 g, 4.9 mmol) in dry CH_2Cl_2 (100 mL) at $-78\text{ }^\circ\text{C}$. After 30 min, a solution of **43** (1.0 g, 4.1 mmol) in dry CH_2Cl_2 (50 mL) was added dropwise into the reaction mixture. The cooling bath was removed after 30 min, and the reaction was stirred for another 1.5 hr. When TLC showed completion, the reaction was quenched with HCl (10%, 5 mL) and extracted with water (300 mL). The aqueous layer was washed with CH_2Cl_2 (150 mL 3X). The organic layers were combined, dried over $MgSO_4$, and evaporated to give the crude product. Purification by flash chromatography (ethyl acetate/petroleum ether 5%) gave pure **62** as a white crystal; Yield 82%; 1H NMR (400MHz, $CDCl_3$): δ 7.27-7.43 (m, 5H), 6.91 (s, 1H), 6.79 (s, 1H), 6.29 (d, J = 11.7 Hz, 2H), 6.08 (td, J = 11.7, 5.1 Hz, 1H), 5.13 (s, 2H), 3.89 (s, 3H), 2.18 (dd, J = 5.1, 4.8 Hz, 2H), 1.46-1.29 (m, 4H), 0.91 (t, J = 5.4 Hz, 3H) ppm; ^{13}C NMR (100 MHz, $CDCl_3$): δ 149.98, 147.56, 137.49, 131.98, 129.73, 129.52, 28.72, 127.98, 127.48, 118.90, 114.47, 109.46, 71.36, 57.16, 32.87, 31.86, 22.48, 14.17 ppm. HRMS (m/z): calcd for $C_{20}H_{24}O_2$ $[M+H]^+$ 297.1855; found, 297.1855.

4-Hexyl-2-methoxy-1-(2-nitrophenoxy)benzene (63)

The solution of **60** (800 mg, 3.8 mmol), 1-fluoro-2-nitrobenzene (536.2 mg, 3.8 mmol), and 18-crown-6 (50.2 mg, 0.19 mmol) in 40 mL dry DMF was heated to 120°C under flushing nitrogen and stirred for 2 hr. The reaction was cooled to rt and extracted with water (200 mL) and CH₂Cl₂ (200 mL). The organic layer was dried with MgSO₄ and evaporated to give the crude product. Purification with flash chromatography (ethyl acetate/petroleum ether = 5%) gave pure **63** as a light yellow oil; Yield 86%; ¹H NMR (300 MHz, CDCl₃): δ 7.94 (dd, *J* = 8.4, 1.5 Hz, 1H), 7.40 (td, *J* = 7.5, 1.8 Hz, 1H), 7.08 (td, *J* = 7.5, 1.5 Hz, 1H), 6.99 (d, *J* = 7.8 Hz, 1H), 6.81 (dd, *J* = 8.4, 1.2 Hz, 1H), 6.80 (dd, *J* = 8.1, 1.8 Hz, 1H), 6.76 (d, *J* = 2.1 Hz, 1H), 3.77 (s, 3H), 2.61 (s, *J* = 7.8 Hz, 2H), 1.62 (m, 2H), 1.32 (m, 2H), 0.89 (t, *J* = 6.9 Hz, 3H) ppm; ¹³C NMR (100 MHz, CDCl₃): δ 152.29, 151.27, 141.80, 141.31, 134.07, 125.80, 121.89, 121.23, 118.08, 113.64, 56.23, 36.06, 31.89, 31.75, 29.15, 22.80, 14.27 ppm; HRMS (*m/z*): calcd for C₁₉H₂₃NO₄ [M+H]⁺ 330.1705; found, 330.1703.

2-(4-Hexyl-2-methoxyphenoxy)aniline (64)

Activated palladium on carbon (25 mg) was added into a solution of **63** (500 mg) in EtOH (50 mL). The reaction was stirred under hydrogen for 6 hr and then filtered. The crude product was obtained by evaporation and used in the next step without further purification. ¹H NMR (400 MHz, CDCl₃): δ 6.88 (td, *J* = 5.7, 1.2 Hz, 1H), 6.78-6.75 (m, 3H), 6.72 (dd, *J* = 6.0 Hz, 1.2 Hz, 1H), 6.65 (dd, *J* = 5.1, 1.5 Hz, 1H), 6.62 (dd, *J* = 6.0, 1.2 Hz, 1H), 3.86 (s, 2H), 3.84 (s, 3H), 2.55 (t,

$J = 6.0$ Hz, 2H), 1.59-1.56 (m, 2H), 1.32-1.28 (m, 6H), 0.87 (t, $J = 5.4$ Hz, 3H) ppm; ^{13}C NMR (100 MHz, CDCl_3): δ 150.53, 144.90, 143.48, 139.24, 138.07, 124.03, 120.84, 119.07, 118.71, 118.36, 116.35, 113.07, 56.92, 35.97, 31.93, 31.46, 29.21, 22.82, 14.29 ppm; HRMS (m/z): calcd for $\text{C}_{19}\text{H}_{25}\text{NO}_2$ $[\text{M}+\text{H}]^+$ 300.1964; found, 300.1963.

1-(2-Chlorophenoxy)-4-hexyl-2-methoxybenzene (65)

The compound was obtained using the general procedure of diazotization, with compound **64** and CuCl . The crude product **65** was used in the next step without purification.

1-(2-Bromophenoxy)-4-hexyl-2-methoxybenzene (66)

The compound was obtained using the general procedure of diazotization, with compound **64** and CuBr . Purification with flash chromatography (ethyl acetate/petroleum ether 5%) gave pure **66**; Yield 65%; ^1H NMR (300 MHz, CDCl_3): δ 7.26 (dd, $J = 6.9, 1.5$ Hz, 1H), 7.18 (dd, $J = 4.8, 1.5$ Hz, 1H), 6.96-6.64 (m, 5H), 3.82 (s, 3H), 2.60 (t, $J = 7.5$ Hz, 2H), 1.65-1.60 (m, 2H), 1.33-1.22 (m, 6H), 0.90 (t, $J = 6.3$ Hz, 3H); MS: $[\text{M}+\text{H}]^+$ 363, 365, found 363, 365.

4-Hexyl-1-(2-iodophenoxy)-2-methoxybenzene (67)

The compound was obtained using the general procedure of diazotization, with compound **64** and CuI . The crude product **67** was used in the next step without purification.

2-(4-Hexyl-2-methoxyphenoxy)benzonitrile (68)

The compound was obtained using the general procedure of diazotization, with compound **64** and CuCN. The crude product **68** was used in the next step without purification.

3-(4-Hexyl-2-methoxyphenoxy)-2-nitropyridine (69)

A solution of **60** (800 mg, 3.8 mmol), 3-bromo-2-nitrobenzene (771.4 mg, 3.8 mmol), and 18-crown-6 (50.2 mg, 0.19 mmol) in dry DMF (40 mL) was heated to 120 °C under flushing nitrogen and stirred for 2 hr. After TLC showed completion, the reaction was cooled to rt and extracted with water (200 mL) and CH₂Cl₂ (200 mL). The organic layer was dried with MgSO₄ and evaporated to give the crude product. Purification with flash chromatography (ethyl acetate/petroleum ether 10%) gave pure **69** as a light yellow oil; Yield 86%; ¹H NMR (400MHz, CDCl₃): δ 7.98 (d, 1H), 7.82 (d, 1H), 6.98 (d, 1H), 6.78-6.72 (m, 3H), 6.60 (d, 1H), 3.64 (s, 3H), 2.58-2.52 (t, 2H), 1.64-1.44 (m, 2H), 1.38-1.22 (m, 6H), 0.94-0.82 (t, 3H) ppm; ¹³C NMR (100 MHz, CDCl₃): δ 156.13, 151.83, 150.90, 141.89, 139.31, 135.28, 133.96, 122.40, 120.77, 117.78, 113.10, 55.90, 35.94, 31.69, 31.29, 29.01, 22.59, 14.06 ppm; HRMS (*m/z*): calcd for C₁₈H₂₂N₂O₄ [M+H]⁺ 311.1658; found, 311.1652.

3-(4-Hexyl-2-methoxyphenoxy) pyridin-2-amine (71)

Activated zinc powder (0.203 g, 3.1 mmol) and NH₄Cl (0.166 g, 3.1 mmol) were added to a solution of **69** (0.128 g, 0.38 mmol) in MeOH (5 mL), and the

mixture was refluxed at 75 °C for 30 min. After TLC showed completion, the reaction mixture was filtered and washed first with water (40 mL) then with CH₂Cl₂ (40 mL). The organic layer was washed with brine, dried over MgSO₄, and concentrated under reduced pressure to give **71** (0.09 g, 77%). The crude compound was used for the next step without further purification.

2-(2-Chlorophenoxy)-5-hexylphenol (PT091)

The compound was obtained using the general procedure of demethylation with compound **65**. Purification with flash chromatography (ethyl acetate/petroleum ether 5%) gave pure **PT091** as a light yellow oil; Yield 83%; ¹H NMR (400 MHz, CDCl₃): δ 7.45 (dd, *J* = 7.9, 1.6 Hz, 1H), 7.20 (td, *J* = 8.0, 1.0 Hz, 1H), 7.07 (td, *J* = 7.9, 1.5 Hz, 1H), 6.96 (dd, *J* = 8.0, 1.5 Hz, 1H), 6.88 (d, *J* = 2.0 Hz, 1H), 6.71 (d, *J* = 8.2 Hz, 1H), 6.64 (dd, *J* = 8.2, 2.0 Hz, 1H), 5.50 (br, 1H), 2.55 (t, *J* = 7.9 Hz, 2H), 1.61-1.58 (m, 2H), 1.37-1.26 (m, 6H), 0.89 (t, *J* = 9.0 Hz, 1H) ppm; ¹³C NMR (100 MHz, CDCl₃): δ 152.49, 167.73, 141.06, 140.28, 130.80, 127.96, 124.91, 124.59, 120.46, 119.22, 118.01, 116.25, 35.47, 31.72, 31.35, 28.94, 22.62, 14.11 ppm.

2-(2-Bromophenoxy)-5-hexylphenol (PT092)

The compound was obtained using the general procedure of demethylation with compound **66**. Purification with flash chromatography (ethyl acetate/petroleum ether 5%) gave pure **PT092** as a light yellow oil; Yield 88%.

5-Hexyl-2-(2-(trifluoromethyl)phenoxy)phenol (PT095)

The compound was obtained using the general procedure of demethylation with compound **61**. Purification with flash chromatography (ethyl acetate/petroleum ether 5%) gave pure **PT095** as a light yellow oil; Yield 90%; ¹H NMR (300MHz, CDCl₃): δ 7.67 (dd, *J* = 7.8, 1.5 Hz, 1H), 7.44 (td, *J* = 7.8, 1.2 Hz, 1H), 7.16 (tt, *J* = 8.1, 0.9 Hz, 1H), 6.93 (d, *J* = 8.4 Hz, 1H), 6.90 (d, *J* = 2.1 Hz, 1H), 6.86 (d, *J* = 8.4 Hz, 1H), 6.69 (dd, *J* = 8.1, 1.8 Hz, 1H), 5.43 (s, 1H), 2.57 (t, *J* = 7.8 Hz, 2H), 1.64-1.56 (m, 2H), 1.37-1.28 (m, 6H), 0.90 (m, 3H) ppm; HRMS (*m/z*): calcd for C₁₉H₂₁F₃O₂ [M+Na]⁺ 361.1391; found, 361.1396.

5-Hexyl-2-(2-iodophenoxy)phenol (PT096)

The compound was obtained using the general procedure of demethylation with compound **67**. Purification with flash chromatography (ethyl acetate/petroleum ether 5%) gave pure **PT096** as a light yellow oil; Yield 85%; HRMS (*m/z*): calcd for C₁₈H₂₁IO₂ [M+Na]⁺ 419.0484; found, 419.0479.

2-(4-Hexyl-2-hydroxyphenoxy)benzonitrile (PT119)

The compound was obtained using the general procedure of demethylation with compound **68**. Purification with flash chromatography (ethyl acetate/petroleum ether 5%) gave pure **PT119** as a white solid; Yield 88%; HRMS (*m/z*): calcd for C₁₉H₂₁NO₂ [M+H]⁺ 296.1651; found, 196.1647.

2-((2-Aminopyridin-3-yl)oxy)-5-hexylphenol (PT130)

The compound was obtained using the general procedure of demethylation with compound **71**. Purification with flash chromatography (ethyl acetate/petroleum ether 10%) gave pure **PT130** as a white solid; Yield 84%; ^1H NMR (400 MHz, DMSO): δ 9.37 (s, 1H), 7.60 (d, 1H), 6.83 (d, 1H), 6.77 (d, 1H), 6.66-6.62 (dd, 2H), 6.45-6.42 (m, 1H), 5.82 (s, 2H), 2.50-2.46 (t, 2H), 1.53-1.52 (m, 2H), 1.34-1.24 (m, 6H), 0.86-0.84 (t, 3H) ppm; HRMS (m/z): calcd for $\text{C}_{17}\text{H}_{22}\text{N}_2\text{O}_2$ $[\text{M}+\text{H}]^+$ 287.1760; found, 287.1758.

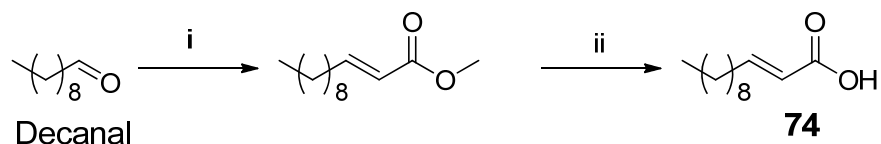
Enzyme Activity Assays

All kinetic experiments were performed on a Cary 300 Bio (Varian) spectrometer at 25 °C in 30 mM PIPES buffer (pH 6.8) containing 150 mM NaCl, 1.0 mM EDTA, and 8% glycerol (v/v). Initial velocities were measured by monitoring the oxidation of NADH to NAD^+ at 340 nm ($\epsilon = 6,300 \text{ M}^{-1} \text{ cm}^{-1}$). IC_{50} values were determined using the same method described in Chapter 2 at an InhA concentration of 20, 50, or 100 nM. However, IC_{50} values neither give any mechanistic information, nor indicate the real binding affinity of inhibitors. Therefore, K_i values were determined for selected tight-binding inhibitors.

The equilibrium dissociation constant of enzyme inhibition (K_i) is a thermodynamic parameter that quantifies the binding affinity of inhibitors to enzymes. K_i values were measured with two different methods, according to whether they are slow-onset inhibitors. More details of slow-onset inhibition will be discussed in Chapter 5.

Preparation of trans-2-Dodecenoyl-CoA (DD-CoA)

(*E*)-methyl dodec-2-enoic acid (**74**) was synthesized following reported methods (**Scheme 3.5**) [126]. Briefly, 5% KOH was added dropwise into a solution of (carbomethoxymethyl)triphenylphosphonium bromide (12 g, 0.029 mol) in H₂O (180 mL), until the solution becomes slightly basic. The resulting fine white precipitate of the ylide was vacuum filtered and dissolved in 100 mL of CH₂Cl₂. Decanal (4.2 mL, 0.022 mol) was added into this solution. The mixture was refluxed for 3 hr and then distilled under vacuum. The residua was saponified in a mixture of 5% KOH (100 mL) and EtOH (100 mL) by refluxing for 1 hr. After removal of EtOH by rotatory evaporation, the solution was washed with 100 mL CH₂Cl₂ for three times and acidified with concentrated HCl. The acidic solution was extracted with 100 mL CH₂Cl₂ for three times and evaporated to give a mixture of (*Z*) and (*E*)-methyl dodec-2-enoic acid (13:87). Purification with flash chromatography (ethyl acetate/petroleum ether 10%) gave pure **74** as a light yellow liquid at an overall yield of 64%; ¹H NMR (300MHz, CDCl₃) δ 7.08 (dt, *J* = 15.6, 6.9 Hz, 1H), 5.82 (dt, *J* = 15.6, 1.2 Hz, 1H), 2.23 (qd, *J* = 7.2, 1.5 Hz, 2H), 1.2-1.5 (br, 14H), 0.88 (t, *J* = 7.2 Hz, 3H); ESI-MS (*m/z*) calcd for C₁₂H₂₃O₂ [M-H]⁻ 197; found, 197.



Scheme 3.5. Synthesis of (E)-methyl dodec-2-enoic acid (74).

Reagents and conditions: i) $\text{CH}_3\text{OCOCH}=\text{PPh}_3$, CH_2Cl_2 , reflux, 3 hr; ii) 5% KOH aq, EtOH, reflux, 1 hr, 64%.

DD-CoA was synthesized from **74** using the mixed anhydride method as described previously [127]. Briefly, 0.882 mL (4.08 mmol) of **74** was dissolved in 10 mL of anhydrous diethyl ether with 0.568 mL (4.08 mmol) of triethylamine. Following the addition of 0.39 mL (4.08 mmol) of ethyl chloroformate, salt crystals formed and the solution was stirred at rt overnight. The mixed anhydride was then filtered and added dropwise to a solution of CoA in 50 mM Na_2CO_3 (pH 8), ethanol, and ethyl acetate (1:1:1) while being stirred at rt. The reaction was kept at rt for 45-75 min, and DD-CoA was purified by HPLC (Shimadzu) using a C-18 semipreparative column. Chromatography was performed with a 20 mM ammonium acetate aqueous solution containing 1.75% acetonitrile as buffer A and acetonitrile as buffer B over 60 min at a flow rate of 4 mL/min. Elution was monitored at 260 nm and 280 nm using a SPD-10A UV-vis detector. Fractions containing DD-CoA were pooled (retention time: 16.5 min) and lyophilized. To completely remove ammonium acetate, the product was dissolved in ddH₂O and lyophilized twice more. ESI-MS (m/z) calcd for $\text{C}_{33}\text{H}_{54}\text{N}_7\text{O}_{17}\text{P}_3\text{S}$ [M-H]⁻ 946.2; found, 946.2.

Measurement of K_i Values

K_i values of rapidly reversible inhibitors were measured by Dr. Nina Liu. Briefly, inhibition constants (K_i) were calculated by determining the k_{cat} and K_M values at several fixed inhibitor concentrations using the same assay conditions to those described above. The inhibition data were analyzed using the standard equation for uncompetitive inhibition. For compounds with K_i values in the low nanomolar range, initial velocities were determined at a fixed substrate concentration. Since triclosan and its analogs are known to inhibit InhA in an uncompetitive manner [111], the data were fit to **Equation 3.1** using a value of $K_M = 29 \mu\text{M}$.

$$v_i/v_0 = (K_M + S)/(K_M + S[1 + [I]/K_i]) \quad \text{Equation 3.1}$$

In Equation **3.1**, v_i and v_0 are the initial velocities in the presence and absence of the inhibitor. K_i is the inhibition constant for the inhibitor binding to InhA-NAD⁺ complex. The substrate concentration was fixed at 15 μM , and the inhibitor concentration was varied from 3.5 to 1200 nM. Data fitting was performed using Grafit 4.0 (Erithacus Software Ltd.).

Preincubation Inhibition Assays for Slow-onset Inhibitors



Figure 3.12. A two-step slow-onset mechanism.

A two-step mechanism of slow-onset inhibition. K_i is the inhibition constant of the first rapid equilibrium step. K_i^* is the inhibition constant of the final complex.

For slow-onset inhibitors, their true binding affinity to InhA is defined by the dissociation constant of the final enzyme-inhibitor complex (K_i^* , **Figure 3.10**). Preincubation inhibition assays were performed to determine apparent K_i^* values as described previously [128]. Briefly, InhA (10 nM) was preincubated in the presence of fixed concentration of DMSO (2%, V/V), NAD^+ (10-200 μ M), NADH (250 μ M) and inhibitor (0-1000 nM) for 5 hr at 4 °C. Then the mixture was warmed to rt, and the reaction was initiated by adding DD-CoA (22 μ M). **Equation 3.2** was used to estimate the apparent inhibition constant K_i^{app} .

$$v_s = v_0 / (1 + [I] / K_i^{app}) \quad \text{Equation 3.2}$$

In **Equation 3.2**, v_s and v_0 are the initial velocity in the presence and absence of inhibitor, respectively, and $[I]$ is the inhibitor concentration.

Chapter 4. Synthesis, Activity, and Drug-like Properties of 4-Pyranone and 4-Pyridone Inhibitors.

Although the diaryl ethers are potent InhA inhibitors, and medicinal chemistry efforts focused on the B-ring have improved their MIC values by 10 folds, the *in vivo* efficacy of these compounds is relatively low due to their poor pharmacokinetics, especially the metabolic instability of the phenol group on the A-ring. In contrast, the 4-pyranones and 4-pyridones have more appropriate drug-like properties, and have been used extensively as key pharmacophores in drug development. These heterocycles provide an opportunity to improve the drug-like properties of the diaryl ethers by replacing the A-ring with these pharmacophores. Nonetheless, synthesis of 4-pyranones and 4-pyridones is not straight forward because of the A-rings are limited to commercially available building blocks. The first synthesis of the 4-pyranones was accomplished by our collaborator, and the scheme was later optimized by our group. 4-Pyridone derivatives with various B-ring modifications were designed to study the SAR of this new scaffold. Unlike the diaryl ethers, the 4-pyridones prefer NADH for binding to InhA, which is presumably determined by interactions between the heterocyclic A-ring and the cofactor. Finally, pharmacokinetic studies showed that **PT166** has an AUC value that is 5 folds higher than the corresponding diphenyl ether **PT119**.

Background

Although the diphenyl ethers showed promising *in vitro* activities against InhA and *M. tuberculosis*, low *in vivo* efficacy has prevented these InhA inhibitors from advancing along the drug discovery pipeline. The early diphenyl ethers violated Lipinski's Rules due to their lipophilicity (ClogP > 5). Subsequent medicinal chemistry efforts on the B-ring resulted in new compounds with higher potency against *M. tuberculosis* (MIC = 0.3 µg/mL) and lower ClogP values (4.9). However, instead of only ClogP, pharmacokinetic properties should be considered as comprehensive criteria for the further development of the diaryl ethers.

Pharmacokinetics in Drug Development

In modern drug discovery, pharmacokinetics commonly refers to drug absorption, distribution, metabolism, and excretion (ADME). Absorption is the process by which a drug proceeds from the site of administration to the systemic circulation. Distribution is the movement of drug molecules from the systemic circulation to extravascular sites. Metabolism describes the enzymatic breakdown of a drug to metabolites that are subsequently cleared from the body, and excretion describes passive or active transport of intact drug molecules into the urine and/or bile [129]. Pharmacokinetics is one of the most important factors that determine the results of drug development. It is reported that 40% of drug candidates fail in clinical trials because of poor pharmacokinetic properties [130].

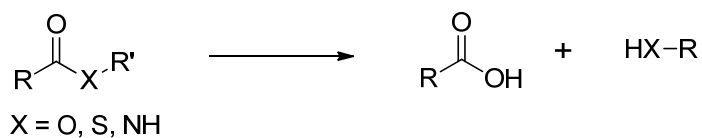
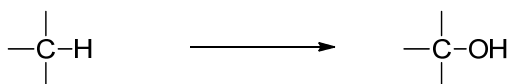
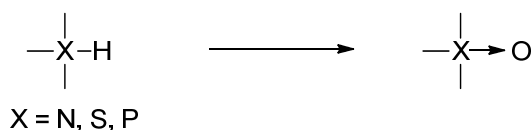
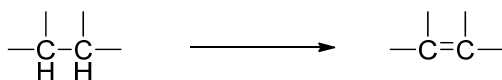
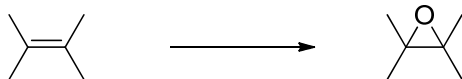
Hydrolysis**Carbon hydroxylation****Heteroatom hydroxylation****Dehydrogenation****Epoxidation**

Figure 4.1. Enzyme catalyzed reactions in Phase I metabolism.

Absorption of a drug is mainly determined by physicochemical properties, such as solubility, charge, molecular weight, polar surface area, hydrogen bonding, and lipophilicity, which are well described and advised by Lipinski's Rules [131]. The distribution process is controlled by the passive diffusion across lipid membranes, the presence of carrier-mediated active transport processes

involving the xenobiotic, and the protein binding in the blood and tissues [132]. Estimation of distribution usually involves mathematical modeling based on experimental data, and thus is difficult to predict in the early stage during lead optimization. Similar to distribution, models for drug excretion are normally established after preclinical trials [133].

Metabolic stability is an important contributor to the pharmacokinetic profile [134], and it can be tested with the liver matrix because the liver has most enzymes involved in metabolism and is the main site for drug biotransformation. Enzyme catalyzed metabolism can be divided into two categories, Phase I and Phase II. Phase I metabolic reactions are functional reactions, which mainly include hydrolysis, reduction, and oxidation (**Figure 4.1**). Phase II reactions are usually conjugations that add polar moieties to either the parent compound or its Phase I metabolites. Sulfotransferases and UDP-glucuronosyltransferases catalyze most Phase II reactions, and the resulted metabolites are readily excreted due to their high polarity (**Figure 4.2**).

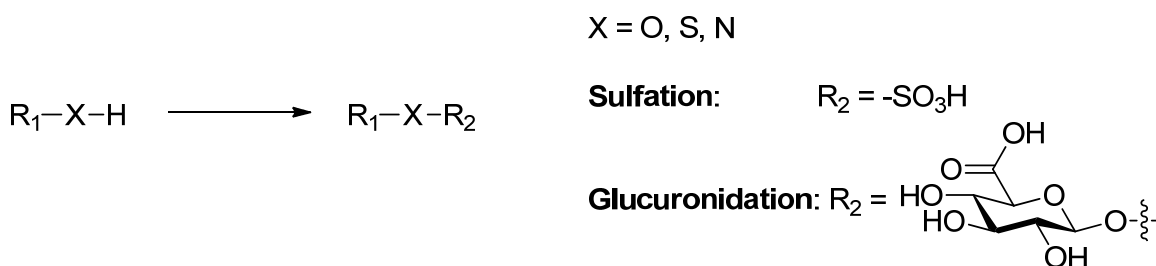


Figure 4.2. Reactions in Phase II metabolism.

4-Pyranones and 4-Pyridones as Important Pharmacophores

An obvious drawback of the diphenyl ether scaffold is the potential metabolic instability of the phenol A-ring. Studies with guinea pigs [135] and human liver fractions [136] showed that triclosan is metabolized primarily to glucuronide *in vivo*. Pharmacokinetic studies of **PT004** with mouse and human liver microsomes revealed that Phase II O-glucuronidation is the primary eliminator of the active compound, while Phase I metabolism is only a minimal contributor [137]. This study also indicated that delivery of **PT004** via intraperitoneal injection (IP) improved the bioavailability (F), plasma half-life ($t_{1/2}$), and area under the curve (AUC), compared to oral administration (PO) (**Table 4.1**).

Table 4.1. Pharmacokinetic parameters for PT004 in male C57/BL6 mice.

	Route and dosage			
	IV 20 mg/kg	PO 50 mg/KG	PO 200 mg/kg	IP 200 mg/kg
AUC (mg hr/L)	0.675	0.046	0.61	3.3
AUC/MIC (mg hr/L)	4.22	0.29	3.81	20.63
$t_{1/2}$ (hr)	1.62	0.54	2.08	3.04
T_{max} (hr)	1	0.5	0.5	1
C_{max} (μmol/L)	0.75	0.2	0.54	1.41
F (%)		2.69	8.94	48.56

^a The AUC/MIC values were calculated based on MIC values against *Francisella tularensis* (*F. tularensis*).

Reproduced from [137].

Although certain administration routes could lead to improved pharmacokinetics of the diaryl ethers, the discovery of phenol UDP-glucuronosyltransferases in bovine alveolar macrophages and bronchial epithelial cells implies that the diaryl ethers may still be metabolized even with direct delivery to the lung [138].

4-Pyranones and 4-pyridones are polar aromatic heterocycles that do not have hydroxyl groups and thus are more stable and more soluble than phenols under physiological conditions (**Figure 4.3**). Because of these properties, they have been incorporated into various drugs [139-142]. It has been reported that some 4-pyranone derivatives showed antimicrobial activity against *Staphylococcus aureus* (*S. aureus*) and *B. subtilis* (MIC = 1 µg/mL), but their target is not yet clear [143] (**Figure 4.3**).

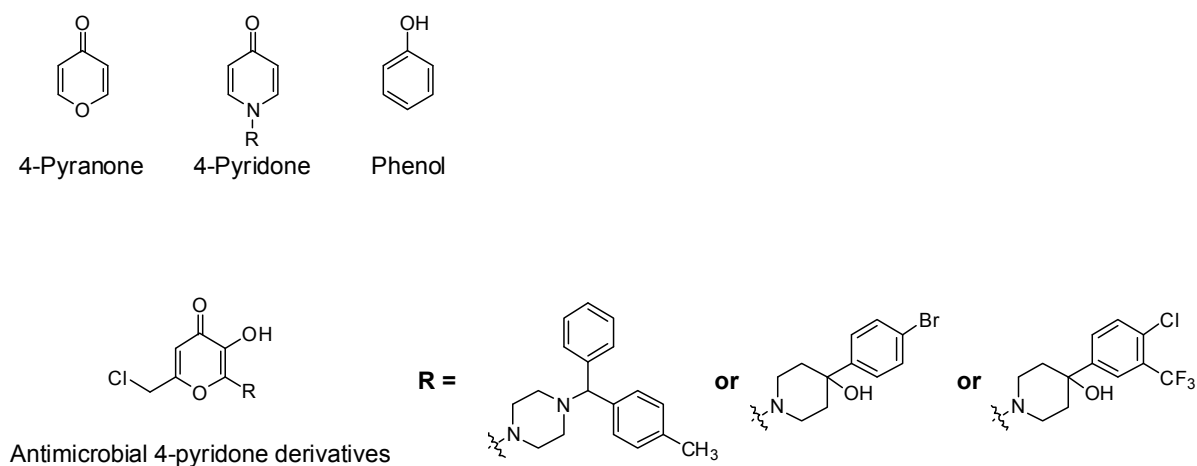
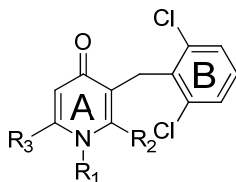


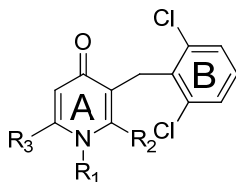
Figure 4.3. Structures of the 4-pyranone, 4-pyridone, and phenol.

Table 4.2. Modifications on 1-N of 4-pyridone FabI inhibitors.



	Compound			IC ₅₀ (μM)		MIC (μg/mL)	
	R ₁	R ₂	R ₃	ecFabI	saFabI	<i>E. coli</i>	<i>S. aureus</i>
81		-CH ₃	H	1.8	1.6	>64	8
82		-CH ₃	H	0.34	0.34	32	0.25
83		-CH ₃	H	0.40	0.35	32	1
84	-H	-CH ₃	H	120			>64
85	-CH ₃	-CH ₃	H	11			>128
86	<i>n</i> -C ₄ H ₉	-CH ₃	H	0.31			2
87	<i>n</i> -C ₁₀ H ₂₁	-CH ₃	H	0.22			32
88	-(CH ₂) ₅ OH	-CH ₃	H	1.8			8
89	-(CH ₂) ₄ COOH	-CH ₃	H	110			
90		-CH ₃	H	0.47			2
91		-CH ₃	H	1.8			16
92		-CH ₃	H	0.30			>128

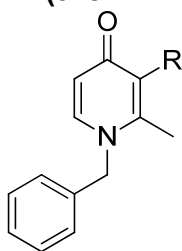
Table 4.2. Modifications on 1-N of 4-pyridone FabI inhibitors.

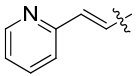
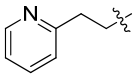
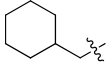


Compound	IC ₅₀ (μM)			MIC (μg/mL)			
	R ₁	R ₂	R ₃	ecFabI	saFabI	<i>E. coli</i>	<i>S. aureus</i>
93		-CH ₃	H	22			>128
94		-CH ₃	H	0.29			1
95		-CH ₃	H	2.5			32
96		-CH ₃	H	8.4			32
97		-CH ₃	H	0.22			0.25
98		-CH ₃	H	0.30			0.5
99	-Bn	-CH ₂ CH ₃	H	0.78			8
100		<i>n</i> -C ₄ H ₉	H	4.5			32
101		-CH ₃	<i>n</i> -Bu	0.38			8
102		-CH ₃		0.29			2

Reproduced from [144, 145].

Table 4.3. Modifications on 3-C (the B-ring) of 4-pyridione derivatives.



Compound	R	IC ₅₀ (μM) for ecFabl	MIC (μg/mL) for <i>S. aureus</i>
103	-Bn	20	64
104	2-Cl-Bn	4.2	64
105	2,6- <i>di</i> -Cl-Bn	0.30	0.5
106	2,4- <i>di</i> -Cl-Bn	2.0	32
107	2,4,6- <i>tri</i> -Cl-Bn	1.5	8
108	2-Cl-6-F-Bn	0.39	2
109	2,6- <i>di</i> -F-Bn	2.7	4
110	2,6- <i>di</i> -Me-Bn	4.3	16
111	-Ph	2.9	
112		>100	
113		>100	
114	Vinyl	>100	
115	<i>n</i> -Bu	61	>128
116		0.40	32

Reproduced from [145].

Hoshiko *et al.* reported three 4-pyridone FabI inhibitors that are active against *E. coli*, *S. aureus*, and methicillin-resistant *S. aureus* (MRSA) [144]. Consequently, medicinal chemistry was performed on both rings of these FabI inhibitors, resulting in new derivatives that have comparable activities to triclosan [145] (**Table 4.2** and **Table 4.3**). Interestingly, these data indicate that this series of compounds and the diaryl ethers have similar SAR. The activity is sensitive to the size of the B-ring, while halogens on the B-ring gave lower IC₅₀ and MIC values than other groups. The A-ring prefers hydrophobic substituents with certain sizes and shapes. Although the crystallographic structures of these compounds are not available, these SAR data implies that they bind to InhA with similar interactions comparable to the diaryl ethers. Furthermore, FabI-FabK dual inhibitors were also synthesized incorporating structures of 4-pyridone FabI inhibitors and phenylimidazole FabK inhibitors [146]. In addition, the 2-pyridone FabI inhibitor CG400549 showed a MIC value of 0.5 µg/mL against *S. aureus* [147, 148], and the drug just entered the Phase II clinical trial.

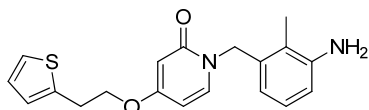


Figure 4.4. The 2-pyridone FabI inhibitor CG400549 [147].

Design of InhA Inhibitors with 4-Pyranone and 4-Pyridone A-Rings

The success of the 2-pyridone FabI inhibitors inspired us to design new InhA inhibitors with 4-pyranone and 4-pyridone A-rings. The design is based on three hypotheses:

- 1) Due to their structural similarity to phenol, the 4-pyranone and 4-pyridone A-rings will have similar interactions with the active site, such as hydrogen bonding, π - π stacking, and hydrophobic contacts, and thus will bind to InhA with comparable affinities as the respective diaryl ether inhibitors.
- 2) InhA inhibitors with 4-pyranone and 4-pyridone A-rings will be more stable *in vivo*, because these heterocycles resist glucuronidation, the predominant metabolism pathway of the diaryl ethers.
- 3) Using the SAR knowledge of the diaryl ethers, modifications will be introduced on the B-ring of the new scaffolds and will result in inhibitors that are highly potent both *in vitro* and *in vivo*.

First, 4-pyranone and 4-pyridone inhibitors with chloromethyl and hexyl groups were synthesized to examine the effect of the A-ring substituents. After we optimized the length of the A-ring substituent, phenyl and pyridyl B-rings were incorporated into these compounds to find the best combination of the A-ring and B-ring (**Figure 4.5**). Finally, inhibitors with promising *in vitro* activities were synthesized in large scale, and pharmacokinetic studies were performed to evaluate the effect of the new scaffolds on their ADME properties.

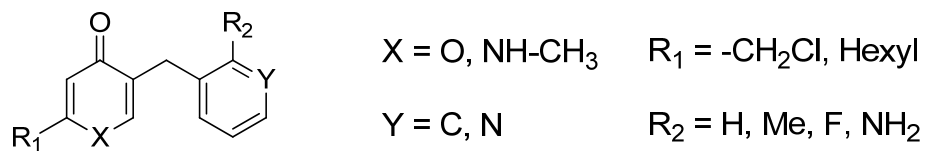
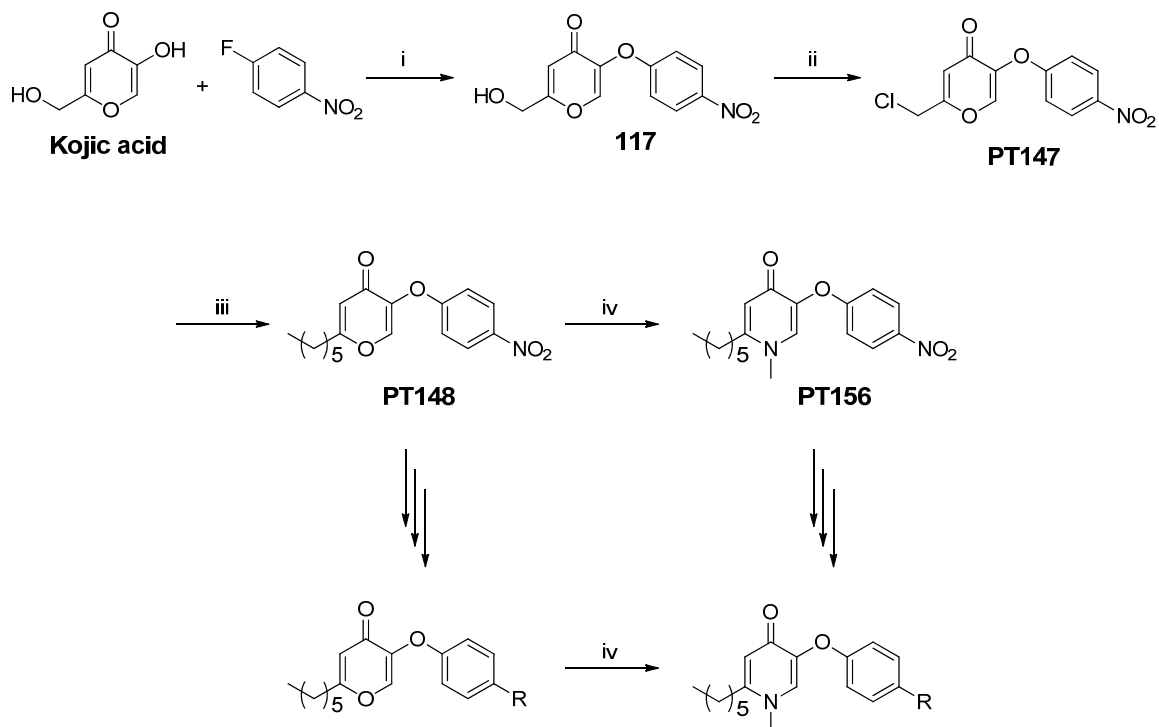


Figure 4.5. The design of InhA inhibitors with 4-pyranone and 4-pyridone A-rings.

Synthetic Strategies for the 4-Pyranones and 4-Pyridones



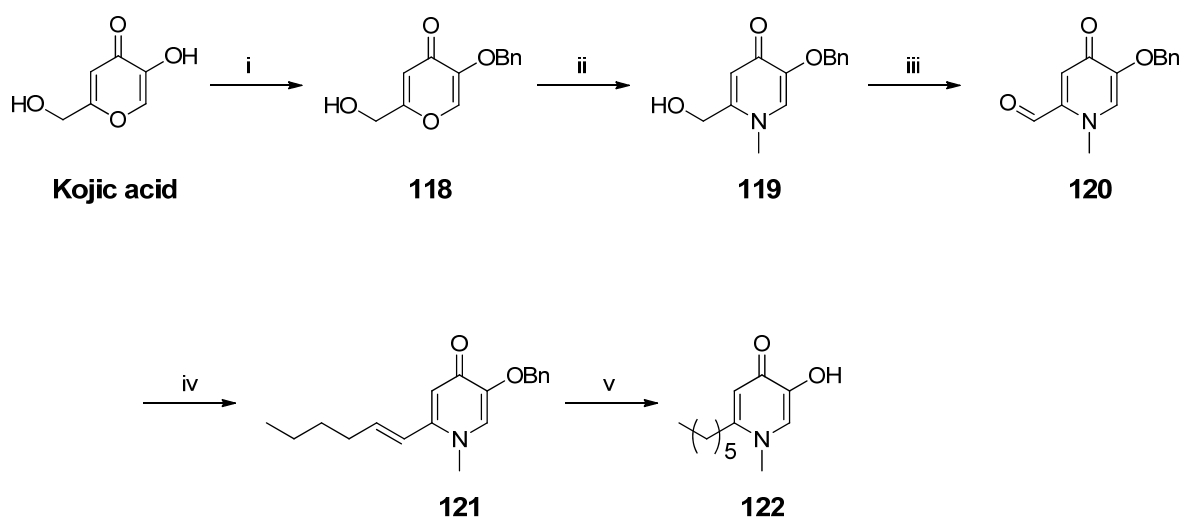
Scheme 4.1. An example of the synthesis of the first 4-pyranones and 4-pyridones.

Reagents and conditions: i) NaH, DMF, 100°C, 3 hr; ii) SOCl₂, DMF, 0°C to rt, 4 hr; iii) *n*-C₅H₉MgBr, Li₂CuCl₄, THF, rt; iv) MeNH₂, H₂O, 80°C, 8 hr.

The synthesis of the first 4-pyranones and 4-pyridones was conducted by our collaborator, Sai Advantium Pharma Ltd., using kojic acid as the starting material (**Scheme 4.1**). The intermediate **117** was obtained through a S_NAr reaction with NaH as the base, and it was subsequently chlorinated to give **PT147**. The following Cu(I)-catalyzed alkylation introduced a pentyl group to give **PT148** [149], which was converted into 4-pyridone **PT156** through a replacement reaction with

methylamine. Compounds **PT148** and **PT156** were used to generate other derivatives through conversions of the nitro group.

The activity data showed that the 4-pyridones showed higher inhibition than the 4-pyranones, and so our synthetic efforts have focused on the 4-pyridones. To obtain analogs, a new scheme was adapted from previous synthesis of the diaryl ethers, in which the intermediate **122** was first synthesized (**Scheme 4.2**).

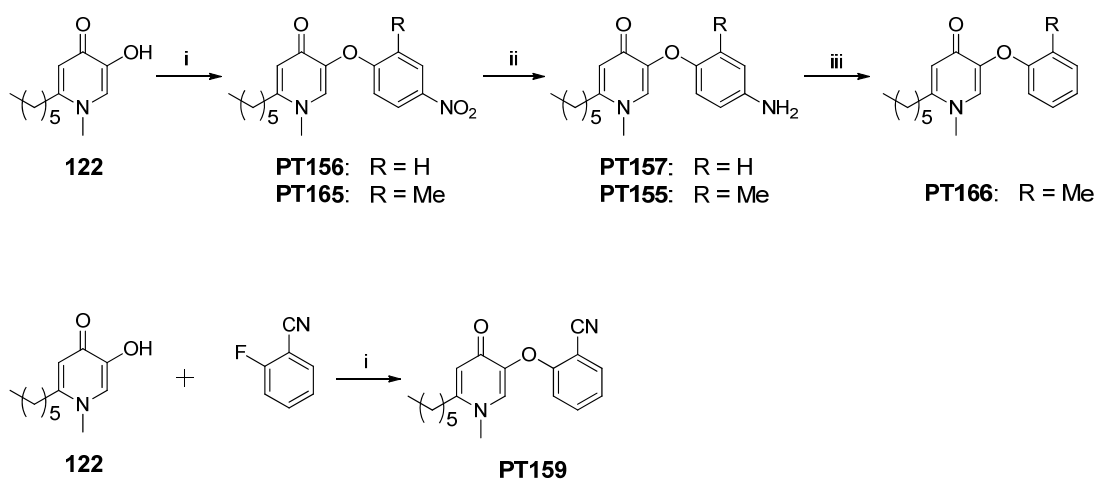


Scheme 4.2. Synthesis of the intermediate **122**.

Reagents and conditions: i) BnBr, KOH (5%), MeOH, H₂O, reflux, 1 hr, 86%; ii) MeNH₂, MeOH, rt, 12 hr, 74%; iii) MnO₂, CHCl₃, reflux, 16 hr, 83% ; iv) *n*-C₅H₉PPh₃, *n*-BuLi, Toluene, CH₂Cl₂, rt, 4 hr, 88%; v) HCl, H₂, Pd-C, EtOH, 6 hr, 52%.

Kojic acid was benzylated to give compound **118**, which was converted into 4-pyridone with a milder condition and a higher yield compared to the previous scheme. Oxidation of **119** was attempted with pyridinium chlorochromate (PCC), Parikh–Doering reaction (SO₃•Py), and MnO₂, but only MnO₂ gave the desired compound **120**. A Wittig reaction with pentenyl ylide then gave compound **121**,

which was hydrogenated to compound **122** by removing the benzyl group and reducing the double bond simultaneously. In this reaction, 3 equivalents of HCl is necessary to prevent the tertiary amine from coordinating to the palladium charcoal.



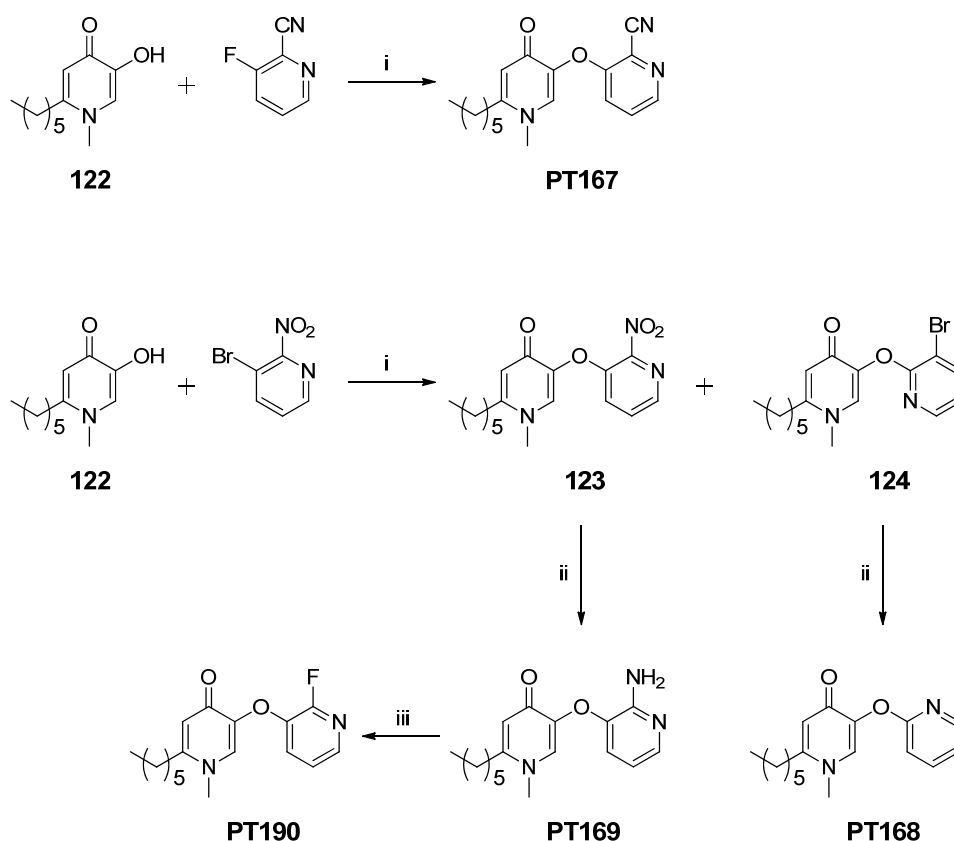
Scheme 4.3. Synthesis of the 4-pyridones with phenyl B-rings.

Reagents and conditions: i) K_2CO_3 , DMF, 18-crown-6, $110^\circ C$, 3 hr; ii) Zn, NH_4Cl , MeOH, reflux, 1 hr; iii) $t-BuNO_2$, DMF, $65^\circ C$, 1 hr, 62%.

Once compound **122** was obtained, various B-rings were coupled to the A-ring to produce 4-pyridone derivatives. Compound **PT156** and **PT165** were synthesized with corresponding phenyl fluoride and were converted to **PT157** and **PT155** using a Clemmensen reduction. Deamination of **PT155** using $t-BuNO_2$ [106] gave compound **PT166**, an analog of **PT070**. Compound **PT159** was readily prepared from compound **122** and 2-fluorobenzonitrile.

Similar strategies were used to synthesize 4-pyridones with pyridyl B-rings (**Scheme 4.4**). Compound **122** was attached to 3-fluoropyridinonitrile to give compound **PT167**. The same reaction conditions with 3-bromo-2-nitropyridine,

however, gave a mixture of compound **123** and **124**, which were separated by flash chromatography. Clemmensen reduction of **123** and **124** resulted in **PT168** and **PT169**, respectively, both of which were purified by flash chromatography, while fluorination of **PT169** through a Balz-Schiemann reaction (HBF_4) did not give **PT190**. This compound was later synthesized from **PT169** using diazotization with NaNO_2 and fluorination with Olah's reagent ($\text{HF}\cdot\text{Py}$).



Scheme 4.4. Synthesis of the 4-pyridones with pyridyl B-rings.

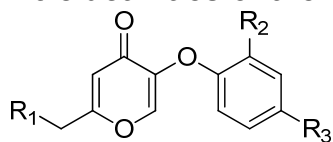
Reagents and conditions: i) K_2CO_3 , DMF, 18-crown-6, 110°C , 3 hr; ii) Zn, NH_4Cl , MeOH, reflux, 1 hr; iii) $\text{HF}\cdot\text{Py}$, NaNO_2 , -78°C to rt, overnight.

Results and discussion

SAR of 4-Pyranone Inhibitors

Six 4-pyranone derivatives were synthesized, and their IC₅₀ and MIC values were evaluated to examine the SAR of the 4-pyranone scaffold (**Table 4.4**). Comparison of inhibitors with a chloromethyl group (**PT147** and **PT149**) and a hexyl group (**PT148** and **PT150**) on the A-ring showed that the hexyl group gave higher binding affinity. An *ortho* methyl group on the B-ring improved the binding affinity 5 fold (**PT148** and **PT150**). Inhibitors with *meta* nitro and amino groups on the B-ring had similar *in vitro* activities (**PT150** and **PT154**), while an *o*-toluanyl B-ring with no substituent resulted in the highest inhibition to InhA(**PT153**). The A-ring SAR of the 4-pyranones is similar to that of the diaryl ethers, indicating that a hexyl group is important for high binding affinity. The effect of the *ortho* methyl on the B-ring is also similar to the diaryl ethers, but the SAR of other groups has not been fully explored.

Table 4.4. *In vitro* activities of the 4-pyranones.



	Compound			IC ₅₀ (nM)	MIC (μg/mL)
	R ₁	R ₂	R ₃		
PT147	-Cl	-H	-NO ₂	N/A ^a	50
PT149	-Cl	-CH ₃	-NO ₂	N/A ^a	N.D. ^b
PT148	<i>n</i> -C ₅ H ₉	-H	-NO ₂	2885 ± 344	50
PT150	<i>n</i> -C ₅ H ₉	-CH ₃	-NO ₂	575 ± 57	>100
PT154	<i>n</i> -C ₅ H ₉	-CH ₃	-NH ₂	471 ± 142	100
PT153	<i>n</i> -C ₅ H ₉	-CH ₃	-H	169 ± 24	50

^a No significant inhibition was observed at 1 μM.

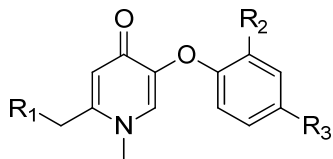
^b Not determined.

SAR of 4-Pyridone Inhibitors

4-Pyridone compounds were synthesized with similar B-rings to the 4-pyranones. Based on the SAR of 4-pyranones, a derivative with an unsubstituted *o*-toluenyl B-ring was synthesized. In addition, an analog of **PT119** with an *ortho* cyano group on the B-ring was also obtained to explore more on the SAR of the B-ring (**Table 4.5**). The results were consistent with those obtained for the 4-pyranones: a hexyl group on the A-ring gave higher binding affinity than a chloromethyl group, an *ortho* methyl group significantly improved *in vivo* activities, and a *meta* nitro and amino group decreased activities by similar levels. Introduction of an *ortho* cyano group on the B-ring of the 4-pyridones (**PT159**) has the same effect as that observed for the diaryl ethers (**PT119**): the binding affinity was decreased. **PT119** showed a 50-fold weaker binding affinity but the same MIC value as **PT070**, while **PT159** showed a 30-fold higher IC₅₀ value and a 20-fold higher MIC value compared to **PT166**. The poor MIC value of **PT159** can be explained by its weak binding affinity to InhA.

Notably, with the same substituents and B-rings, the 4-pyridones always show better *in vitro* activities than the 4-pyranones, and **PT166** showed comparable IC₅₀ and MIC values to the top diaryl ether inhibitors. These results suggest that the 4-pyridone is a better scaffold than the 4-pyranone, presumably because the electron-rich oxygen atom in the 4-pyranone ring is not favorable in the hydrophobic binding site, while the nitrogen atom of the 4-pyridone ring is covered by a nonpolar methyl group and thus tolerated.

Table 4.5. *In vitro* activities of the 4-pyridones.



	Compound			IC ₅₀ (nM) ^a	MIC (µg/mL)
	R ₁	R ₂	R ₃		
PT151	-Cl	-H	-NO ₂	N/A ^b	N.D. ^c
PT152	-Cl	-CH ₃	-NO ₂	2252 ± 148	12.5
PT156	<i>n</i> -C ₅ H ₉	-H	-NO ₂	407 ± 37	50
PT157	<i>n</i> -C ₅ H ₉	-H	-NH ₂	424 ± 132	50
PT165	<i>n</i> -C ₅ H ₉	-CH ₃	-NO ₂	N.D. ^c	N.D. ^c
PT155	<i>n</i> -C ₅ H ₉	-CH ₃	-NH ₂	107 ± 16	6.25
PT166	<i>n</i> -C ₅ H ₉	-CH ₃	-H	28.6 ± 4.7	3.13
PT159	<i>n</i> -C ₅ H ₉	-CN	-H	629 ± 19	50

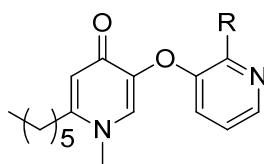
a Values were determined at an enzyme concentration of 50 nM.

b No significant inhibition was observed at 1 µM.

c Not determined.

Because the 4-pyridone is a promising scaffold, further modifications were performed on the B-ring to clarify the SAR of this series of compounds. Based on the SAR of the diaryl ethers, we synthesized 4-pyridones with substituted or unsubstituted pyridyl B-rings (**Table 4.6**).

Table 4.6. 4-Pyridones derivatives with pyridyl B-rings.



Compound	IC ₅₀ (nM) ^a	MIC (μg/mL)
PT159	629 ± 19	50
R		
PT169	379 ± 41	12.5
PT167	979 ± 152	100
PT190	641 ± 55	25
PT168	1778 ± 315	50

^a Values were determined at an enzyme concentration of 50 nM.

Compared to **PT159**, its pyridyl analog **PT167** has a slightly higher IC_{50} value and a similar MIC value. In the case of the diaryl ethers, replacement of the phenyl B-ring with a pyridine also resulted in higher IC_{50} value but a 5-fold lower MIC value (**Figure 4.6**). These differential effects of the pyridyl B-ring on MIC values may be because of changes in cell permeability. Although the ClogP value was reduced by 1.1 units in both cases of the diaryl ethers and the 4-pyridones, its impact on cell permeability of the diaryl ethers would be more significant because of high lipophilicity of the scaffold. Whereas for the 4-pyridones, a decrease of 1.1 units in ClogP values is not speculated to improve the cell permeability because the parent compound **PT159**, with a small ClogP value, should already fairly penetrate cell membrane.

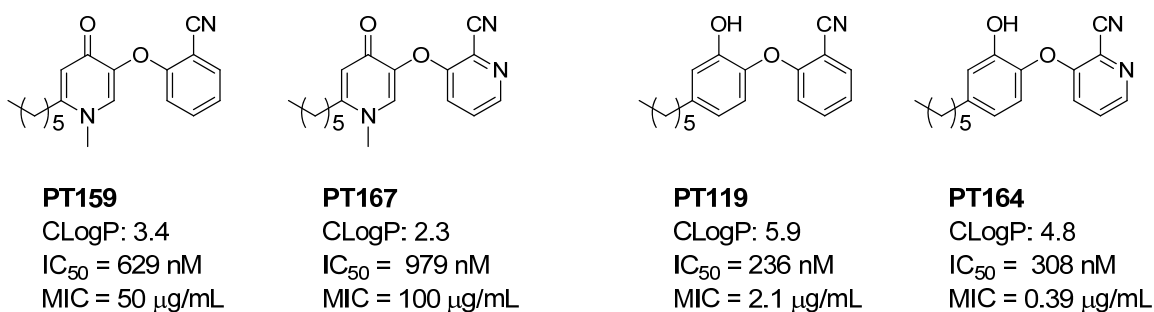


Figure 4.6. Comparison of the phenyl and pyridyl B-ring.

Smaller groups on the B-ring (**PT169** and **PT190**) resulted in smaller IC_{50} and MIC values, which is consistent with the SAR of the diaryl ethers. However, the 4-pyridone scaffold prefers an amino group over a fluorine atom—**PT190** has IC_{50} and MIC value about two times that of **PT169**. To understand the SAR, the X-ray crystallographic structures of **PT070** [109] and **PT155** were used for a search of interactions within 5 Å of the *ortho* methyl on the B-ring of **PT155**

(Figure 4.7). The crystallographic structure of **PT155** was provided by Dr. Hui-Jiun Li.

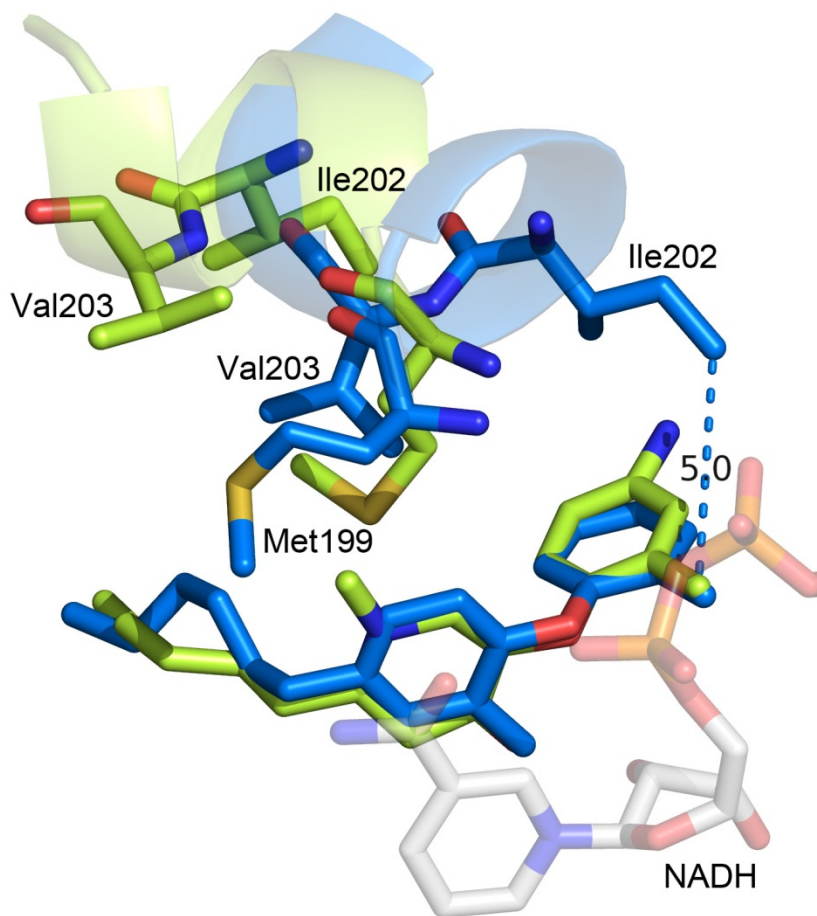


Figure 4.7. PT070 and PT155 bound to InhA.

Overlaid X-ray crystallographic structures of **PT070** (blue, 2x23.pdb) [109] and **PT155** (green) bound to the active site of InhA.

The results showed that the diaryl ethers and the 4-pyridones bind to different conformations of the substrate binding loop. The methyl group on the A-ring of the 4-pyridones resulted in displacement of Met199 because of the van der Waals contact conflict, which then caused changes in the conformation of the

substrate binding loop. As a result, Ile202 moved away from the inhibitor and no longer interacts with the *ortho* methyl group. Without the hydrophobic contact of Ile202, polar, electron donating groups are more tolerated at the *ortho* position on the B-ring. In addition, a hydrogen bonding donor, such as an amino group, could be more favorable because of hydrogen bonding between the *ortho* group and the cofactor NADH.

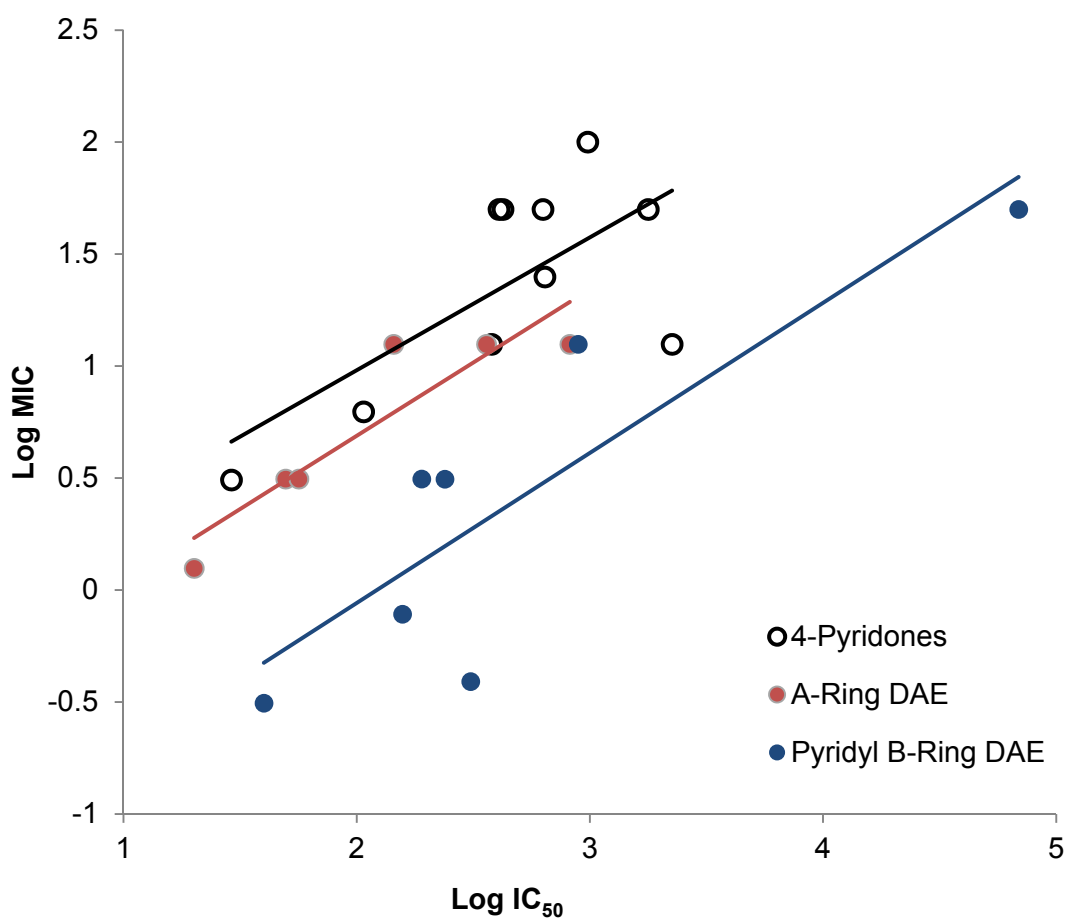


Figure 4.8. The correlation between MIC and IC₅₀ values.

The semilog plot of selected data from **Table 2.3, 2.4, 3.5, 4.5, and 4.6** shows that MIC and IC₅₀ values are correlated.

Comparison of **PT168** with **PT159** and **PT040** with **PT119** showed that a pyridin-2-yl B-ring is much better tolerated in the 4-pyridones than in the diaryl ethers, probably because of the changes in the conformation of the substrate binding loop, as mentioned above.

Finally, MIC and IC₅₀ values of selected compound from **Table 4.5** and **4.6** are showed in a double log plot to confirm that all compound target InhA to inhibit cell growth (**Figure 4.8**). The data were also compared with A-ring modified (**Table 2.3** and **2.4**) and pyridyl B-ring diaryl ethers (**Table 3.5** and **4.5**), showing that both 4-pyridines and diaryl ethers target InhA but the 4-pyridones are generally less potent than the diaryl ethers.

Cofactor Preference for 4-Pyridone Binding to InhA

The diaryl ethers bind preferentially binding to InhA with the cofactor NAD⁺ [86, 111]. Therefore, they are co-crystallized with InhA and NAD⁺ [86, 109], and the presence of NAD⁺ is also confirmed by the dihedral angle 1'-1-6-5 of 179.7° (**Figure 4.9**). However, this angle in the complex of **PT155** bound to InhA is 174.7°, which implies that the cofactor is NADH.

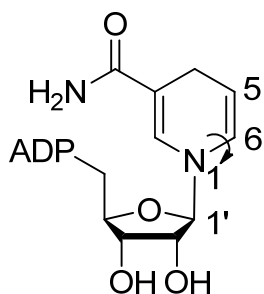


Figure 4.9. The dihedal angle 1'-1-6-5 in the cofactor NAD⁺/NADH.

To test cofactor preference of the 4-pyridones, the melting points (T_m) of InhA with **PT070** and **PT166** were measured using Thermofluor stability assays. The Thermofluor assay determines the T_m of a protein by monitoring fluorescence intensities at a range of temperature. A protein-inhibitor complex usually has lower energy and is more stable than the free enzyme, thus, an increase in the T_m will be observed upon an inhibitor binding to the protein, and the difference in T_m (ΔT_m) reflects the relative binding affinity of the inhibitor (**Figure 4.10**) [150].

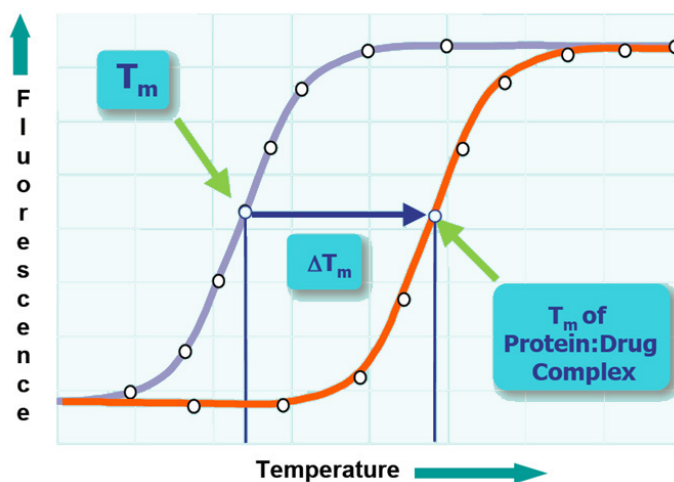


Figure 4.10. Inhibitor binding changes the T_m of a protein. Taken from [151].

The result of **PT070** is consistent with enzyme kinetic assays, where the ΔT_m with NAD^+ is 10 °C higher than that with NADH, indicating a preference of NAD^+ . However, **PT166** prefers binding to InhA with NADH, showing a ΔT_m 8 °C higher than that with NAD^+ (**Table 4.7**). The A-ring of the diaryl ethers interacts with the nicotinamide ring through π - π stacking. This interaction is kept for the 4-pyridone ring, while an additional hydrogen bonding between the nitrogen atom in the A-ring and the amide of the nicotinamide also becomes favorable. As a result, NADH, with a non-aromatic nicotinamide ring, has an amide closer to the A-ring nitrogen and thus stronger hydrogen bonding to the 4-pyridones.

Table 4.7. Thermofluor results of PT070 and PT166.

Ligand	Blank	PT070		PT166	
		+ NADH	+ NAD^+	+ NADH	+ NAD^+
T_m (°C)	46.20 ± 0.90	56.80 ± 1.10	66.6 ± 1.30	61.60 ± 1.60	53.20 ± 1.20
ΔT_m		8.6	18.4	13.4	5.0

Pharmacokinetics

The 4-pyridone inhibitor **PT166** showed promising IC_{50} and MIC values, which are similar to **PT070**, and was therefore selected for pharmacokinetic studies. The diaryl ethers **PT001** and **PT119** were selected for comparison. **MUT37307** is a FabI inhibitor that is highly active against *S. aureus* and already is currently in Phase I clinical trials. Consequently, the pharmacokinetic parameters of **MUT37307** were also measured as a positive control (**Table 4.8**).

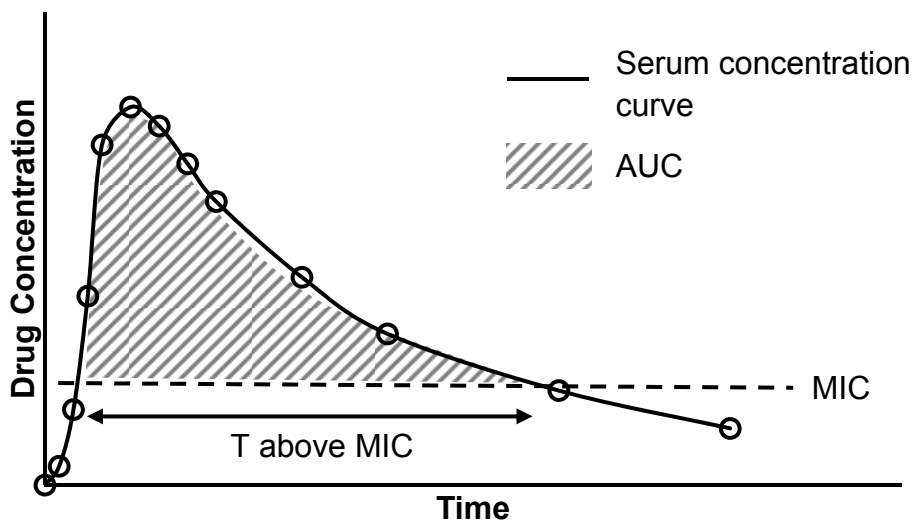
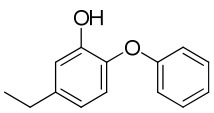
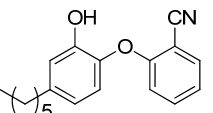
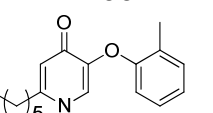
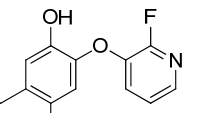


Figure 4.11. AUC and T above MIC.

Area under curve (AUC) is an important pharmacokinetic parameter, which describe the amount of a drug absorbed into the systemic circulation. AUC depends on both the concentration and time of a drug in serum. While T above MIC only indicates the time scale of the drug concentration higher than MIC (**Figure 4.11**).

PT166 showed a short T_{max} , indicating rapid absorption of the compound. It also has improved pharmacokinetic behavior, such as an AUC value 5 fold higher than **PT119** and an AUC/MIC value 4 folds higher than **PT119**. However, compared to **MUT37307**, the AUC/MIC of **PT166** may still need to be improved by 2-3 fold before it shows desired *in vivo* activities.

Table 4.8. Pharmacokinetic parameters for InhA inhibitors.

	PT001 	PT119 	PT166 	MUT37307 
Dosage (IP, mg/kg)	100	100	100	100
T_{1/2} (hr)	5.6	N/A ^a	2.75	2.24
T_{max} (hr)	0.25	5	0.25	0.25
C_{max} (ng/ml)	1564.5	409	45868	3803
T above MIC (hr)	10.0	N/A ^a	8.5	0.5
T above MIC/MIC	7.75	5.52	17	2
AUC₀₋₂₄ (hr µg/ml)	15.5	11.0	53.0	11.62
AUC₀₋₂₄/MIC (hr)	0.97 ^c	4.4 ^c	18 ^c	46 ^b
MIC (µg/ml)	16 ^c	2.5 ^c	3 ^c	0.25 ^b

^a The compound did not show a regular concentration curve.

^b Values were based on inhibition data against *S. aureus*.

^c Values were based on inhibition data against *M. tuberculosis*.

Summary

Because of their ideal pharmacokinetic properties, 4-pyranones and 4-pyridones were incorporated into new scaffolds of InhA inhibitors to improve their *in vivo* activities. Medicinal chemistry studies were performed on the A-ring substituents and the B-rings to understand the SAR of the new scaffolds.

Similar to the diaryl ethers, the 4-pyranones and 4-pyridones prefer longer alkyl chains on the A-ring. A hexyl group gave higher binding affinity than a chloromethyl group. For both 4-pyranones and 4-pyridones, an *ortho* methyl group on the B-ring improved the binding affinity dramatically, while *meta* amino and nitro groups on the B-ring weakens the binding affinity by 3-5 fold. Notably, replacement of 4-pyranone with 4-pyridone always resulted in higher activity, which indicates that the 4-pyridone is a better scaffold.

To further understand the SAR and optimize the *in vitro* activities of the 4-pyridones, derivatives with pyridyl B-rings were synthesized. As observed for the diaryl ethers, the B-ring prefers small substituents as large groups decrease the binding affinity. Surprisingly, the 4-pyridones prefer an *ortho* amino group over a fluorine atom on the B-ring, whereas the diaryl ethers have an opposite preference. The difference can be explained by the conformations of the substrate binding loop upon inhibitor binding. The A-ring methyl group displaced Met199 away from the inhibitor thus causing movement of the loop. As a result, van der Waals interactions from Ile202 are missing in the 4-pyridone bound

active site, and hydrogen bonding interactions between the *ortho* group and the phosphate group of the cofactor become favorable.

The cofactor preference of the 4-pyridones binding to InhA was determined using Thermofluor stability assays. Data showed that the 4-pyridones prefer NADH in the active site, while the diaryl ethers prefer NAD⁺, which is consistent to previous kinetic data. The change in cofactor preference is because the A-ring nitrogen atom also favors hydrogen bonding with the cofactor.

Pharmacokinetic studies of **PT166** showed that the 4-pyridone scaffold improved the pharmacokinetic parameters significantly, compared to the diaryl ethers **PT001** and **PT119**. Although the *in vivo* activity of **PT166** has not been evaluated, from the comparison between **PT166** and **MUT37307** it can be concluded that optimization of pharmacokinetics is the key to higher *in vivo* activities and that the work should be continued for InhA inhibitors.

Experimental Section

Enzyme Activity Assays

IC₅₀ values of the 4-pyranones and the 4-pyridones were performed using the same method described in Chapter 2 at an InhA concentration of 50 nM.

Thermofluor

The Thermofluor stability assay was performed on a Bio-Rad CFX96 Real-Time System following a previously reported method [152], using 30 mM PIPES buffer (pH 6.8) containing 150 mM NaCl and 1.0 mM EDTA. Briefly, a 20 μ L solution of 25 μ M InhA and 10X SYPRO Orange protein gel stain, with or without 50 μ M inhibitor (**PT070** or **PT166**) and 200 μ M cofactor (NADH or NAD⁺), was prepared on a 96-well plate. A thermo cycle was run from 25°C to 90°C. At the end of each 0.20°C increment for 10 min, the fluorescence intensity of the plate was read after 10 min.

Organic Synthesis

The synthesis of the final compounds and necessary intermediates is described in this section. Other compounds were synthesized by Sai Advantium Pharma Ltd., India (**Table 4.9**). All commercially available chemicals and

solvents were used without further purification. All new compounds gave satisfactory spectroscopic and/or analytical data. ¹H and ¹³C NMR spectra were recorded at 300, 400, or 500 MHz, and chemical shifts are reported in parts per million (δ) downfield from the internal standard tetramethylsilane (TMS). Mass spectra were obtained using electrospray (ES) ionization techniques.

Table 4.9. Contributors for synthesis of the 4-pyranones and the 4-pyridones.

Compound	Synthesis performed by
PT147	Sai Advantium Pharma Ltd.
PT148	Sai Advantium Pharma Ltd.
PT149	Sai Advantium Pharma Ltd.
PT150	Sai Advantium Pharma Ltd.
PT151	Sai Advantium Pharma Ltd.
PT152	Sai Advantium Pharma Ltd.
PT153	Sai Advantium Pharma Ltd.
PT154	Sai Advantium Pharma Ltd.
PT155	Sai Advantium Pharma Ltd. and Pan Pan
PT156	Sai Advantium Pharma Ltd. and Pan Pan
PT157	Sai Advantium Pharma Ltd. and Pan Pan
PT159	Pan Pan
PT165	Pan Pan

Table 4.9. Contributors for synthesis of the 4-pyranones and the 4-pyridones.

Compound	Synthesis performed by
PT166	Pan Pan
PT167	Pan Pan
PT168	Pan Pan
PT169	Pan Pan
PT190	Pan Pan

5-(Benzyloxy)-2-(hydroxymethyl)-4H-pyran-4-one (118)

An aqueous solution of KOH (5%, 250 mL) was added to a solution of kojic acid (14.2 g, 0.1 mol) and benzyl bromide (13.1 mL, 18.8g, 0.11 mol) in MeOH (250 mL). The mixture was stirred and heated to 95 °C to reflux for approximately 1 hr. After TLC (10% MeOH/CH₂Cl₂) showed completion of the reaction, the mixture was poured into 500 mL iced water and neutralized with 10% HCl. The solution was extracted with EtOAc (300 mL, 3X), and the organic layers were combined and evaporated to give the crude product. Purification by flash chromatography (MeOH/CH₂Cl₂ 8%) gave the pure compound **118** as white crystals. Yield 86%; ¹H NMR (400 MHz, CD₃OD): δ 8.17 (s, 1H), 7.45 (d, *J* = 7.2 Hz, 2H), 7.41-7.31 (m, 3H), 6.52 (s, 1H), 5.03 (s, 2H), 4.42 (s, 2H) ppm; ¹³C NMR (100 MHz, CD₃OD): δ 175.60, 169.23, 146.89, 141.74, 135.86, 128.21, 128.03, 127.73, 110.67, 71.15, 59.64 ppm; ESI-MS (*m/z*): calcd for C₁₃H₁₂O₄ [M+H]⁺ 233.1; found, 233.1.

5-(Benzyloxy)-2-(hydroxymethyl)-1-methylpyridin-4(1H)-one (119)

A solution of methyl amine (33%, 40 mL) in EtOH was added into a solution of **118** (4.6g, 20 mmol) in MeOH (200 mL). The mixture was stirred overnight in a round bottom flask that was sealed with a rubber septum. The product precipitated as a white solid. When TLC (10% MeOH/CH₂Cl₂) showed completion of the reaction, the reaction was concentrated to approximately 50 mL and cooled in an ice bath. The product **119** was obtained by filtration of the cold mixture. Yield 74%; white crystal; ¹H NMR (400 MHz, DMSO-d₆): δ 7.57 (s, 1H), 7.42-7.32 (m, 5H), 6.23 (s, 1H), 5.55 (s, 1H), 4.99 (s, 2H), 4.37 (s, 2H), 3.58 (s, 3H) ppm; ¹³C NMR (100 MHz, DMSO-d₆): δ 172.07, 149.18, 147.45, 137.70, 129.71, 128.78, 128.44, 128.30, 115.52, 71.05, 59.73, 39.69 ppm.

5-(Benzyloxy)-1-methyl-4-oxo-1,4-dihydropyridine-2-carbaldehyde (120)

A solution of **119** (2.5 g, 10 mmol) and activated MnO₂ (3.4 g, 40 mmol) in CHCl₃ (150 mL) was stirred and heated to 80 °C to reflux overnight. When TLC (10% MeOH/CH₂Cl₂) showed completion of the reaction, the mixture was cooled to rt and filtered through Celite 545 to remove MnO₂. Purification by flash chromatography (MeOH/CH₂Cl₂ 8%) gave the pure compound **120** as light yellow crystals. Yield 83%; ¹H NMR (300 MHz, CD₃OD): δ 9.75 (s, 1H), 7.57 (s, 1H), 7.46 (d, *J* = 7.2 Hz, 2H), 7.38-7.31 (m, 3H), 6.77 (s, 1H), 5.08 (s, 2H), 3.80 (s, 3H) ppm; ¹³C NMR (125 MHz, CD₃OD): δ 172.45, 147.86, 147.75, 136.37, 129.07, 128.12, 127.80, 127.78, 113.73, 93.33, 70.98, 40.46 ppm; ESI-MS (*m/z*): calcd for C₁₄H₁₃NO₃ [M+H]⁺ 244.1; found, 244.1.

(E)-5-(benzyloxy)-2-(hex-1-en-1-yl)-1-methylpyridin-4(1H)-one (121)

A solution of *n*-BuLi (2.0 M in cyclohexane, 3.0 mL, 6.0 mmol) was added dropwise into a solution of *n*-pentyltriphenylphosphonium bromide (2.1 g, 5.5 mmol) in toluene (100 mL). After 30 min, the solution became dark red, and a solution of **120** (1.2 g, 5.0 mmol) in CH₂Cl₂ (100 mL) was added dropwise into the flask. The reaction was stirred at rt for approximately 1 hr. When TLC (MeOH/CH₂Cl₂ 5%) showed completion of the reaction, the reaction was quenched with HCl (10%, 10 mL) and washed with water (200 mL) and CH₂Cl₂ (100 mL). The aqueous layer was then washed with CH₂Cl₂ (50 mL, 2X), and the organic layers were combined and evaporated to give the crude product. Purification by flash chromatography (MeOH/CH₂Cl₂ 4%) gave the pure compound **121** as a white crystal. Yield 88%.

2-Hexyl-5-hydroxy-1-methylpyridin-4(1H)-one (122)

A solution of **121** (594.8 mg, 2.0 mmol), HCl (10%, 2.2 mL, 6.0 mmol), and palladium charcoal (27.5 mg) in EtOH (100 mL) was sealed under vacuum and flushed with hydrogen for at least three times. The reaction mixture was stirred at rt under hydrogen gas for approximately 6 hr. When TLC (MeOH/CH₂Cl₂ 5%) showed completion of the reaction, the mixture was filtered through Celite 545 and concentrated to give the crude product. Purification by flash chromatography (MeOH/CH₂Cl₂ 4%) gave the pure compound **122** as a pale solid. Yield 52%; ¹H

NMR (300 MHz, CDCl₃): δ 7.13 (s, 1H), 6.33 (s, 1H), 5.30 (s, br, 1H), 3.61 (s, 3H), 2.53 (t, *J* = 7.2 Hz, 2H), 1.60 (m, 2H), 1.41-1.24 (m, 6H), 0.89 (t, *J* = 7.2 Hz, 3H) ppm; ¹³C NMR (125 MHz, CDCl₃): δ 173.71, 151.87, 149.61, 124.73, 115.12, 43.38, 35.07, 34.13, 31.47, 30.82, 25.16, 16.66 ppm; ESI-MS (*m/z*): calcd for C₁₂H₁₉NO₂ [M+H]⁺ 210.1; found, 210.1.

2-Hexyl-1-methyl-5-((2-nitropyridin-3-yl)oxy)pyridin-4(1H)-one (123)

Compound **122** (209.3 mg, 1.0 mmol), 3-bromo-2-nitropyridine (203.0 mg, 1.0 mmol), K₂CO₃ (345.5 mg, 2.5 mmol), and 18-crown-6 (10.5 mg) were sealed under vacuum and flushed with nitrogen gas three times, after which DMF (50 mL) was added to the flask to dissolve the solid. The reaction mixture was heated to 110 °C and stirred for approximately 3 hr. When TLC (MeOH/CH₂Cl₂ 5%) showed completion of the reaction, the reaction was cooled to rt and washed with water (100 mL) and CH₂Cl₂ (100 mL) three times. The organic layers were combined and evaporated to give the crude product. Purification by flash chromatography (MeOH/CH₂Cl₂ 2%) gave the pure compound **123** as a yellow oil. Yield 35%; ¹H NMR (400 MHz, CDCl₃): δ 8.34 (dd, *J* = 8.0, 1.6 Hz, 1H), 7.97 (dd, *J* = 4.8, 1.6 Hz, 1H), 7.49 (s, 1H), 7.09 (dd, *J* = 8.0, 3.2 Hz, 1H), 6.34 (s, 1H), 3.59 (s, 3H), 2.49 (t, *J* = 7.2 Hz, 2H), 1.60-1.56 (m, 2H), 1.39-1.27 (m, 6H), 0.86 (t, *J* = 6.4 Hz, 3H) ppm; ¹³C NMR (100MHz, CDCl₃): δ 172.19, 159.03, 151.07, 145.87, 142.91, 135.84, 134.54, 119.72, 118.64, 107.10, 43.38, 35.07, 34.13, 31.47, 30.82, 25.16, 16.66 ppm; ESI-MS (*m/z*): calcd for C₁₇H₂₁N₃O₄ [M+H]⁺ 332.2; found, 332.2.

5-((3-Bromopyridin-2-yl)oxy)-2-hexyl-1-methylpyridin-4(1H)-one (124)

Compound **124** was separated from the reaction mixture of compound **123** as a light yellow oil. Yield 41%; ^1H NMR (300 MHz, CDCl_3): δ 8.27 (dd, $J = 4.8, 2.0$ Hz, 1H), 7.82 (dd, $J = 7.6, 1.6$ Hz, 1H), 7.41 (s, 1H), 6.81 (dd, $J = 8.0, 4.8$ Hz, 1H), 6.35 (s, 1H), 3.57 (s, 3H), 2.49 (t, $J = 7.2$ Hz, 2H), 1.60-1.56 (m, 2H), 1.39-1.27 (m, 6H), 0.86 (t, $J = 6.4$ Hz, 3H) ppm; ^{13}C NMR (100 MHz, CDCl_3): δ 173.71, 151.87, 149.61, 124.73, 115.12, 43.38, 35.07, 34.13, 31.47, 30.82, 25.16, 16.66 ppm; ESI-MS (m/z): calcd for $\text{C}_{17}\text{H}_{21}\text{BrN}_2\text{O}_2$ $[\text{M}+\text{H}]^+$ 365.1; found, 365.1.

5-(4-Amino-2-methylphenoxy)-2-hexyl-1-methylpyridin-4(1H)-one (PT155)

A solution of **PT165** (344.4 mg, 1.0 mmol), activated Zn powder (400 mg), and NH_4Cl (300 mg) in MeOH (30 mL) was heated to 70 °C and refluxed for 1 hr. When TLC (MeOH/ CH_2Cl_2 5%) showed completion of the reaction, the mixture was filtered and evaporated to give the crude product. Purification by flash chromatography (MeOH/ CH_2Cl_2 3%) gave the pure compound **PT155** as a yellow oil. Yield 79%.

2-Hexyl-1-methyl-5-(4-nitrophenoxy)pyridin-4(1H)-one (PT156)

Compound **122** (209.3 mg, 1.0 mmol), 1-fluoro-4-nitrobenzene (141.1 mg, 1.0 mmol), K_2CO_3 (345.5 mg, 2.5 mmol), and 18-crown-6 (10.5 mg) were vacuum in a sealed flask and flushed with nitrogen gas for three times, and then DMF (50 mL) was added into the flask to dissolve the solid. The reaction mixture was heated to 110 °C and stirred for approximately 3 hr. When TLC (MeOH/ CH_2Cl_2

5%) showed that the reaction was completed, the reaction was cooled to rt and washed with water (100 mL) and CH₂Cl₂ (100 mL) three times. The organic layers were combined and evaporated to give the crude product. Purification by flash chromatography (MeOH/CH₂Cl₂ 3%) gave the pure compound **PT156** as a yellow oil. Yield 80%.

5-(4-Aminophenoxy)-2-hexyl-1-methylpyridin-4(1H)-one (PT157)

A solution of **PT156** (330.4 mg, 1.0 mmol), activated Zn powder (400 mg), and NH₄Cl (300 mg) in MeOH (30 mL) was heated to 70 °C and refluxed for 1 hr. When TLC (MeOH/CH₂Cl₂ 5%) showed completion of the reaction, the mixture was filtered and evaporated to give the crude product. Purification by flash chromatography (MeOH/CH₂Cl₂ 3%) gave the pure compound **PT157** as a yellow oil. Yield 82%.

2-((6-Hexyl-1-methyl-4-oxo-1,4-dihydropyridin-3-yl)oxy)benzotrile (PT159)

Compound **122** (209.3 mg, 1.0 mmol), 2-fluorobenzotrile (121.1 mg, 1.0 mmol), K₂CO₃ (345.5 mg, 2.5 mmol), and 18-crown-6 (10.5 mg) were sealed under vacuum and flushed with nitrogen gas three times, after which DMF (50 mL) was added into the flask to dissolve the solid. The reaction mixture was heated to 110 °C and stirred for approximately 3 hr. When TLC (MeOH/CH₂Cl₂ 5%) showed completion of the reaction, the reaction was cooled to rt and washed with water (100 mL) and CH₂Cl₂ (100 mL) three times. The organic layers were

combined and evaporated to give the crude product. Purification by flash chromatography (MeOH/CH₂Cl₂ 3%) gave the pure compound **PT159** as a yellow oil. Yield 86%; ¹H NMR (300 MHz, CDCl₃): δ 7.57-7.52 (m, 2H), 7.40 (td, *J* = 10.8, 2.0 Hz, 1H), 7.02 (td, *J* = 10.4, 1.2 Hz, 1H), 6.78 (d, *J* = 11.2 Hz, 1H), 6.38 (s, 1H), 3.64 (s, 1H), 2.54 (t, *J* = 10.4 Hz, 2H), 1.67-1.57 (m, 2H), 1.45-1.28 (m, 6H), 0.92-0.87 (m, 1H) ppm; ¹³C NMR (100 MHz, CDCl₃): δ 171.80, 159.13, 151.30, 142.20, 135.27, 134.01, 133.24, 122.16, 118.86, 116.32, 115.08, 101.74, 40.75, 31.96, 31.40, 28.75, 27.78, 22.42, 13.92 ppm; ESI-MS (*m/z*): calcd for C₁₉H₂₂N₂O₂ [M+H]⁺ 311.2; found, 311.1.

2-Hexyl-1-methyl-5-(2-methyl-4-nitrophenoxy)pyridin-4(1H)-one (PT165)

Compound **122** (209.3 mg, 1.0 mmol), 2-fluoro-5-nitrotoluene (155.1 mg, 1.0 mmol), K₂CO₃ (345.5 mg, 2.5 mmol), and 18-crown-6 (10.5 mg) were sealed under vacuum and flushed with nitrogen gas for three times, after which DMF (50 mL) was added to dissolve the solid. The reaction mixture was heated to 110 °C and stirred for approximately 3 hr. When TLC (MeOH/CH₂Cl₂ 5%) showed completion of the reaction, the reaction was cooled to rt and washed with water (100 mL) and CH₂Cl₂ (100 mL) three times. The organic layers were combined and evaporated to give the crude product. Purification by flash chromatography (MeOH/CH₂Cl₂ 3%) gave the pure compound **PT165** as a yellow oil. Yield 83%.

2-Hexyl-1-methyl-5-(*o*-tolylloxy)pyridin-4(1H)-one (PT166)

A solution of *t*-BuNO₂ (118.7 mg, 0.137 mL, 1.15 mmol) in DMF (30 mL) was heated to 65 °C under nitrogen, and a solution of **PT155** (314.4 mg, 1.0 mmol) in CH₂Cl₂ (20 mL) was added dropwise into the flask. After being stirred at 65 °C for 30 min, the reaction became dark red. When TLC (MeOH/CH₂Cl₂ 5%) showed completion of the reaction, the mixture was cooled to rt and washed with water (100 mL) and CH₂Cl₂ (100 mL). The organic layer was dried over MgSO₄ and evaporated to give the crude product. Purification by flash chromatography (MeOH/CH₂Cl₂ 3%) gave the pure compound **PT166** as a red oil. Yield 62%.

3-((6-Hexyl-1-methyl-4-oxo-1,4-dihydropyridin-3-yl)oxy)picolinonitrile (PT167)

Compound **122** (209.3 mg, 1.0 mmol), 3-fluoropicolinonitrile (122.1 mg, 1.0 mmol), K₂CO₃ (345.5 mg, 2.5 mmol), and 18-crown-6 (10.5 mg) were sealed under vacuum and flushed with nitrogen gas for three times, after which DMF (50 mL) was added to dissolve the solid. The reaction mixture was heated to 110 °C and stirred for approximately 3 hr. When TLC (MeOH/CH₂Cl₂ 5%) showed completion of the reaction, the reaction was cooled to rt and washed with water (100 mL) and CH₂Cl₂ (100 mL) for three times. The organic layers were combined and evaporated to give the crude product. Purification by flash chromatography (MeOH/CH₂Cl₂ 3%) gave the pure compound **PT167** as a light yellow solid. Yield 75%; ¹H NMR (400 MHz, CDCl₃): δ 8.20 (d, *J* = 4.0 Hz, 1H), 7.60 (s, 1H), 7.30 (dd, *J* = 8.8, 4.4 Hz, 1H), 7.09 (d, *J* = 8.4 Hz, 1H), 6.31 (s, 1H),

3.60 (s, 3H), 2.50 (t, $J = 8.0$ Hz, 2H), 1.58-1.52 (m, 2H), 1.35-1.24 (m, 6H), 0.83 (t, $J = 7.2$ Hz, 3H) ppm; ^{13}C NMR (100 MHz, CDCl_3): δ 171.32, 156.99, 152.14, 144.37, 141.40, 135.90, 127.95, 123.40, 122.93, 119.06, 115.35, 41.05, 32.18, 31.59, 28.96, 27.95, 22.73, 14.15 ppm; ESI-MS (m/z): calcd for $\text{C}_{17}\text{H}_{22}\text{N}_2\text{O}_2$ $[\text{M}+\text{H}]^+$ 287.2; found, 287.2.

2-Hexyl-1-methyl-5-(pyridin-2-yloxy)pyridin-4(1H)-one (PT168)

A solution of **124** (365.3 mg, 1.0 mmol), activated Zn powder (400 mg), and NH_4Cl (300 mg) was heated to 70 °C to reflux for 1 hr. When TLC showed completion of the reaction ($\text{MeOH}/\text{CH}_2\text{Cl}_2$ 5%), the mixture was filtered through Celite 545 and evaporated to give the crude product. Purification by flash chromatography ($\text{MeOH}/\text{CH}_2\text{Cl}_2$ 3%) gave the pure compound **PT168** as a dark yellow oil. Yield 71%; ^1H NMR (400 MHz, CDCl_3): δ 8.03 (d, $J = 3.6$ Hz, 1H), 7.59 (td, $J = 7.2, 1.6$ Hz, 1H), 7.48 (s, 1H), 6.94 (d, $J = 8.4$ Hz, 1H), 6.88 (t, $J = 6.0$ Hz, 1H), 6.42 (s, 1H), 3.55 (s, 3H), 2.46 (t, $J = 7.6$ Hz, 2H), 1.56 (q, $J = 7.6$ Hz, 2H), 1.28-1.25 (m, 6H), 0.83 (t, $J = 5.8$ Hz, 3H) ppm; ^{13}C NMR (100 MHz, $\text{DMSO}-d_6$): δ 172.70, 162.90, 151.26, 147.26, 142.75, 139.83, 135.33, 118.78, 118.58, 111.63, 40.92, 32.26, 31.64, 29.03, 27.92, 22.66, 14.18 ppm; ESI-MS (m/z): calcd for $\text{C}_{17}\text{H}_{22}\text{N}_2\text{O}_2$ $[\text{M}+\text{H}]^+$ 287.2; found, 287.2.

5-((2-Aminopyridin-3-yl)oxy)-2-hexyl-1-methylpyridin-4(1H)-one (PT169)

A solution of **123** (331.4 mg, 1.0 mmol), activated Zn powder (400 mg), and NH_4Cl (300 mg) was heated to 70 °C to reflux for 1 hr. When TLC showed

completion of the reaction (MeOH/CH₂Cl₂ 5%), the mixture was filtered through Celite 545 and evaporated to give the crude product. Purification by flash chromatography (MeOH/CH₂Cl₂ 3%) gave the pure compound **PT169** as a dark yellow oil. Yield 68%; ¹H NMR (400 MHz, DMSO-d₆): δ 7.86 (s, 1H), 7.14 (dd, *J* = 4.8, 1.6 Hz, 1H), 6.91 (dd, *J* = 7.6, 1.6 Hz, 1H), 6.72 (dd, *J* = 7.6, 4.8 Hz, 1H), 6.18 (s, 1H), 5.07 (br, 2H), 3.61 (s, 3H), 2.56 (t, *J* = 6.0 Hz, 2H), 1.55-1.49 (m, 2H), 1.36-1.26 (m, 6H), 0.84 (t, *J* = 7.2 Hz, 3H) ppm; ¹³C NMR (100 MHz, DMSO-d₆): δ 171.95, 151.91, 151.45, 142.76, 136.62, 133.36, 132.92, 120.98, 119.75, 117.38, 31.60, 28.96, 17.89, 22.70, 18.66, 14.59, 9.98 ppm; ESI-MS (*m/z*): calcd for C₁₇H₂₃N₃O₂ [M+H]⁺ 302.2; found, 302.2.

5-((2-Fluoropyridin-3-yl)oxy)-2-hexyl-1-methylpyridin-4(1H)-one (PT190)

A solution of **PT169** (152.2 mg, 0.50 mmol) in Olah's reagent (~70% HF in pyridine, 5 mL) was cooled to -78 °C, and NaNO₂ (690.0 mg, 10 mmol) was added slowly into the solution. The mixture was stirred at -78 °C for 10 min, and the cooling bath was replaced with an ice bath. The reaction was stirred at 0 °C for another 30 min and then heated to 55 °C for at least 3 hr. When TLC showed completion of the reaction (MeOH/CH₂Cl₂ 5%), the mixture was poured into saturated NaHCO₃ solution (50 mL) and extracted with CH₂Cl₂ (30 mL, 3X). The organic layers were combined and dried over MgSO₄. Purification by flash chromatography (MeOH/CH₂Cl₂ 3%) gave the pure compound **PT169** as a dark yellow oil. ¹H NMR (400 MHz, CDCl₃): δ 7.79 (dd, *J* = 4.8, 1.6 Hz, 1H), 7.45 (s, 1H), 7.377 (td, *J* = 8.8, 1.6 Hz, 1H), 6.92-6.88 (m, 1H), 6.47 (s, 1H), 3.60 (s, 1H),

2.51 (t, $J = 7.6$ Hz, 1H), 2.22 (td, $J = 7.6, 3.2$ Hz, 1H), 1.62-1.52 (m, 2H), 1.30-1.24 (m, 6H), 0.88-0.83 (m, 3H) ppm; ^{13}C NMR (100 MHz, CDCl_3): δ 177.31, 172.38, 151.66 (d, $J_{\text{F-C}} = 12.2$ Hz), 148.79, 146.21, 142.15, 141.64, 135.13, 124.68, 118.53, 40.92, 34.16, 31.64, 29.07, 24.80, 22.67, 14.18 ppm; ESI-MS (m/z): calcd for $\text{C}_{17}\text{H}_{21}\text{FN}_2\text{O}_2$ $[\text{M}+\text{H}]^+$ 305.2; found, 305.1.

Chapter 5. Mechanism of Slow-Onset Inhibition of InhA.

Although the residence time of a drug on its target is an important criterion for *in vivo* activity, this concept has long been neglected in drug development. The discovery of slow-onset inhibitors of InhA provided a system to study the mechanism of time-dependent enzyme inhibition. Progress curve analysis was used to identify diaryl ethers that were time-dependent inhibitors of InhA. Together with X-ray crystallography, MD simulations, and direct measurements of inhibitor dissociation, the structural changes that characterize time dependent enzyme inhibition have been identified, and the residence time of the compounds on InhA have been correlated with the energy changes during dissociation.

These data support the importance of helix-6 and helix-7 motion in the time-dependent inhibition of InhA. In particular, a steric clash between residues V203 and I215 is important for modulating the energy of the transition state leading to the final enzyme-inhibitor complex. Selective mutations were able to abolish time-dependent inhibition observed in the wild-type enzyme. However, new inhibitors were rationally designed to successfully regain slow-onset inhibition. These novel studies suggest ways in which residence time can be rationally modulated.

Background

On-Target Residence Times: Missing Criteria in Drug Development

Modern drug discovery has become more complicated and challenging, according to statistical data describing the costs and time scales of pharmaceutical research. By the year 2010, the cost to bring a new drug to market is estimated to be \$1.8 billion, and commercialization of a new molecular entity (NME) can take up to 16 years [153, 154]. The total cost of pharmaceutical research and development has risen by more than 10 times since 1980, while annual NME approvals have occurred at almost the same rate over this period (Figure 5.1) [155].

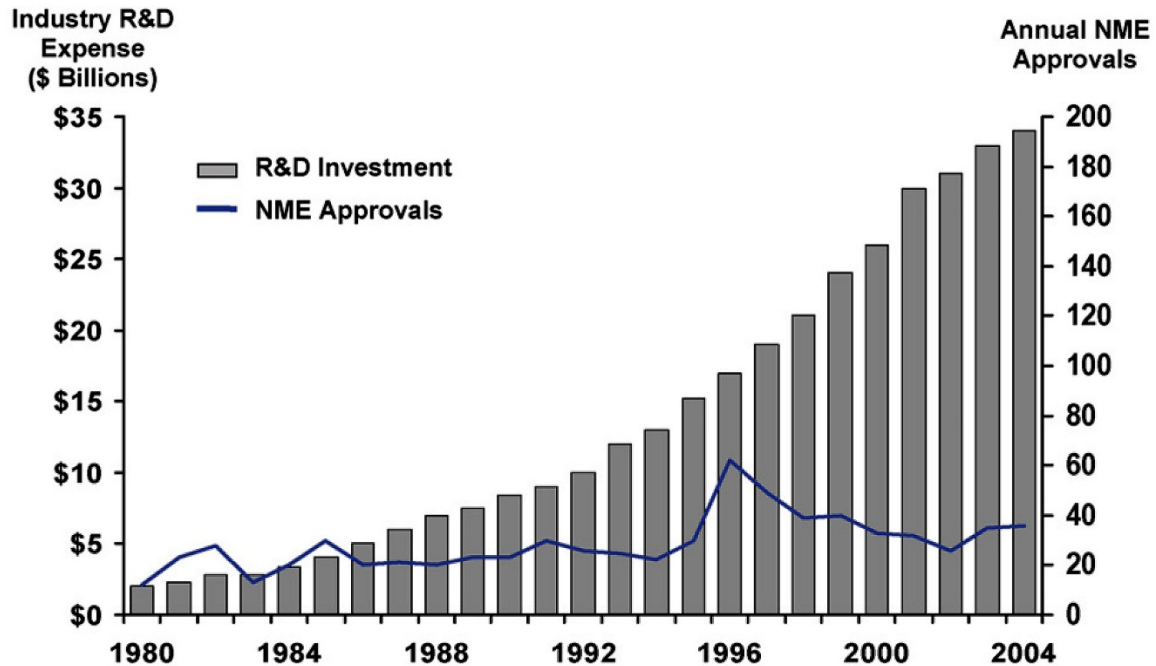


Figure 5.1. The cost of pharmaceutical research.

The cost of pharmaceutical research and number of NME approvals (1980-2004). Taken from [155].

A primary source of attrition in drug discovery stems from lack of efficacy in Phase II clinical trials [156], which implies that the current criteria for lead identification and optimization do not accurately predict the in vivo behavior of drug molecules. In the lead identification and pre-clinical stages, thermodynamic parameters, such as IC50, Ki, and MIC values are used for evaluation purposes. These parameters describe the equilibrium between free and bound drug molecules. Pharmacokinetics is considered in pre-clinical or Phase 0 clinical trials and describes the kinetics of intracellular drug concentration. We believe that the gap in understanding for the in vivo behavior of drugs lies in the kinetics of drug-target binding (Figure 5.2)

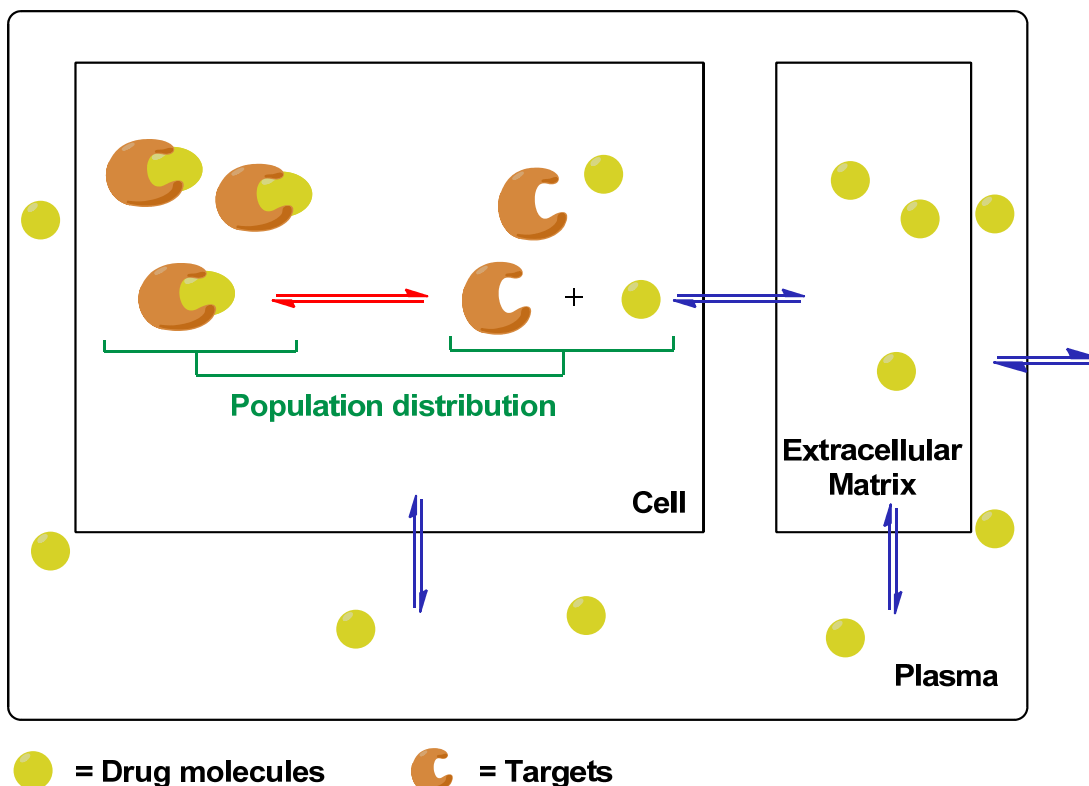


Figure 5.2. Thermodynamic and kinetic parameters.

A schematic view of thermodynamics (green) and kinetics (red) of drug-target complex formation, and pharmacokinetics (blue).

Slow-Onset Inhibition

The kinetics of drug-target complex formation reflects the time frame of drug-target association and dissociation. Slow-onset inhibition is defined as the kinetics of inhibitors that slowly bind to or dissociate from their targets [128]. A two-step slow-onset model has been shown to apply for the inhibition of InhA by the diaryl ethers (**Figure 5.3**), where the inhibitor binds to the enzyme rapidly in the first step to form the initial enzyme-inhibitor complex (EI), which is followed by a slow transition to a more stable complex (EI*).



Figure 5.3. Rapid reversible and slow-onset inhibition.

In this scheme, k_1 and k_2 are forward rate constants for the first and second steps, respectively, while k_{-1} and k_{-2} are the reverse rate constants for the first and second steps, respectively. A convenient metric for quantifying enzyme-inhibitor life-time is the residence time (t_R), which is related to half-life ($t_{1/2}$) and the rate constant of dissociation (k_{off}) [157-159]:

$$t_R = \frac{t_{1/2}}{0.69} = \frac{1}{k_{off}} = \frac{k_{-1} + k_2 + k_{-2}}{k_{-1}k_{-2}} \approx \frac{1}{k_{-2}} \quad \text{Equation 5.1}$$

Because $k_{-2} \gg k_2$ and k_{-1} for most of slow-onset inhibitors, k_{off} can be approximated by k_{-2} in **Equation 5.1** [160]. Many inhibitors have t_R ranging from minutes to days [157, 161] (**Table 5.1**). For InhA, we found that the isoniazid-

NAD adduct [162] and the diaryl ether **PT070** [109] are slow-onset inhibitors that have t_R of 63 and 24 min, respectively.

Table 5.1. Examples of ligand-target complexes that have long residence times.

Enzyme	Inhibitor	k_{on} ($M^{-1}s^{-1}$)	k_{off} (s^{-1})	E-I $t_{1/2}$
Chymotrypsin	Chymostatin	1.2×10^6	3.2×10^{-4}	0.5 hr
Cytidine deaminase	Cytidine phosphinamide analog	8.3×10^3	7.8×10^{-6}	25 hr
Alanine racemase	1-Aminoethyl phosphonate	7	3.2×10^{-7}	25 days
Ribulosebiphosphate carboxylase	2 CABP	7.8×10^4	1.5×10^{-8}	535 days

Table taken from [128].

Residence Times and In Vivo Efficacy

Thermodynamic parameters, such as IC_{50} , K_i or K_d , are used in drug discovery to improve the binding affinity of the drug molecule to the target and thus lower the dose required for efficacy. However, this approach overlooks the fact that the drug concentration usually fluctuates *in vivo*, and can fall below the K_i or K_d value for the target and cause the drug-target complex to dissociate. On the other hand, pharmacokinetic studies monitor the drug concentration at tissue

level. However, in the cases of slow-onset inhibition, drug-target complexes can stay for a long time even after the drug is eliminated from plasma. Under these conditions, the percent saturation of both the target and any off-target protein(s) will vary with time, and neither drug-target binding thermodynamics or pharmacokinetics is adequate to predict the *in vivo* behavior of drug molecules [161].

Consequently, it is more appropriate to include the life-time of the drug-target complex as a key criterion in drug development, although it was never systematically examined in the pharmaceutical industry. Recently, researchers have begun to realize the importance of target binding kinetics in drug safety and efficacy [160, 163-166], and supportive experimental data have been reported [167].

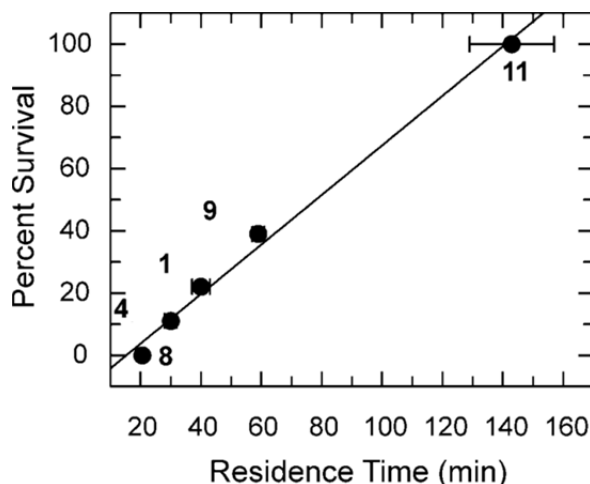


Figure 5.4. Residence time and survival percentage are correlated.

Compound 1, 4, 8, 9, and 11 are inhibitors of ftuFabl that have different t_R . Figure taken from [168].

Previously, we identified inhibitors of the FabI from *Francisella tularensis* (ftuFabI) with activity in an animal model of tularemia (**Figure 5.4**) [168]. Importantly, the *in vivo* efficacy of the ftuFabI inhibitors correlated with their t_R on the enzyme target but not with their K_i values for enzyme inhibition nor their *in vitro* antibacterial activity (MIC). Since K_i and MIC values are determined at constant drug concentrations, the studies with ftuFabI support the importance of drug-target residence time in predicting *in vivo* drug activities.

Mechanisms of Slow-onset Inhibition

In Chapter 1, kinetics and X-ray crystallography was discussed for slow-onset inhibition of ecFabI by triclosan, but the conformational changes from EI to EI* and interactions that trigger this transition are not yet fully understood. We believe that a detailed understanding of the kinetics of drug-target complex formation would improve our ability to predict *in vivo* efficacy when coupled to knowledge of drug pharmacokinetics.

Our SAR studies showed that large groups on the A-ring and *ortho* substituents on the B-ring play important roles in inhibitor binding. Introduction of a methyl group to the B-ring of **PT004** resulted in the first slow-onset diaryl ether inhibitor of InhA (**PT070**, **Figure 5**), which showed a 430-fold increase in binding affinity compared to **PT004**. Comparison of X-ray crystallographic structures of InhA with **PT003**, **PT070**, and triclosan bound to the active site revealed important interactions for slow-onset inhibitors.

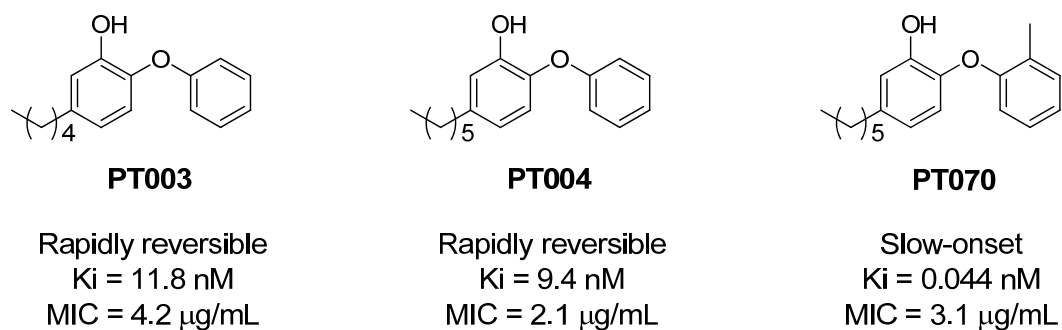


Figure 5.5. The diaryl ethers PT004 and PT070.

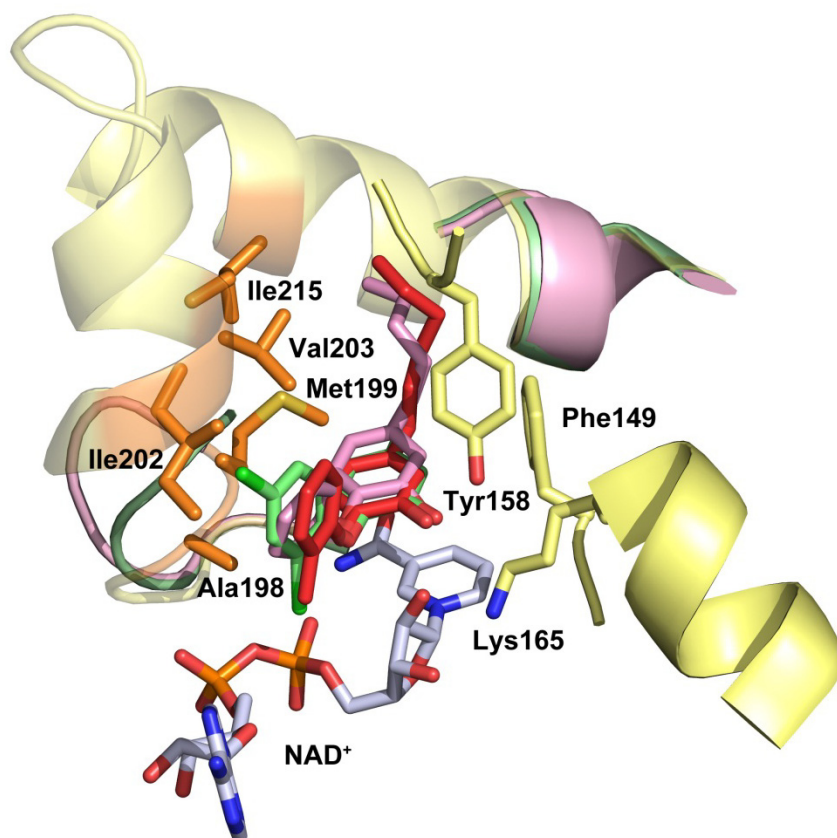


Figure 5.6. The substrate binding loop in the active site.

Overlaid structures of the active site of InhA containing **PT003** (pink, 2b36.pdb) [86], **PT070** (red, 2x23.pdb) [109], and triclosan (green, 2b35.pdb) [86]. The figure was made with PyMol [102].

All the three inhibitors share interactions with Phe149, Tyr158, and Lys165, as mentioned in previous chapters. The substrate binding loop (residues 195-210, helices 6 and 7) is ordered when **PT070** is bound to the active site, while the loop was disordered and missing in the structures of **PT003** and triclosan. Residues within 5 Å of **PT070** have extensive van der Waals contacts with the inhibitor, including Ala198, Met 199, Ile202, Val203, and Ile215. The *ortho* methyl group on the B-ring restricted the conformation of **PT070** and thus stabilized these interactions in the final EI* complex. In addition, the methyl group, on its own, interacts with Ala198 and favors **PT070** binding to InhA [109].

In this chapter, we first identify slow-onset inhibitors of InhA using progress curve analysis, and then determined the t_R values for these compounds. The X-ray crystallographic structures of InhA complexes with these inhibitors revealed that the interaction between Val203 and Ile215 is the main contributor to the energy barrier of the transition state. For inhibitors that have very fast binding steps, t_R values were measured by rapid dilution of concentrated reaction mixtures. Finally, InhA mutants and slow-onset inhibitors of these mutants were used to confirm the proposed mechanism of slow-onset inhibition.

Materials and Methods

X-ray crystallographic data of **PT092** and **PT119** were collected and processed by Dr. Huei-Jiun Li, and computational simulation works were performed by and Cheng-Tsung Lai.

Expression and Purification of InhA.

The plasmid carrying the gene for InhA, the *M. tuberculosis* enoyl-ACP reductase, was obtained from a previous laboratory member Dr. Nina Liu. InhA was expressed in *E. coli* strain BL21 (DE3) pLysS cells. After transformation, a single colony was used to inoculate 10 mL of Luria Broth (LB) media containing 0.2 mg/mL ampicillin in a 50 mL falcon tube, which was then incubated overnight at 37 °C. The overnight culture was then used to inoculate 1 L of LB media containing 0.2 mg/mL ampicillin, which was incubated at 37 °C until the optical density at 600 nm (O.D. 600) increased to approximately 0.8. Protein expression was induced by adding 1 mM isopropyl-1-thio- β -D-galactopyranoside (IPTG) and the culture was then shaken at 25 °C for 16h. Cells were harvested by centrifugation at 5,000 rpm for 20 min at 4 °C. The cell paste was then resuspended in 30 mL of His binding buffer (5 mM imidazole, 0.5 M NaCl, 20 mM Tris HCl, pH 7.9) and lysed by sonication. Cell debris was removed by centrifugation at 33,000 rpm for 60 min at 4 °C. InhA was purified using His affinity chromatography: the supernatant was loaded onto a His-bind column (1.5 cm X 15 cm) containing 4 mL of His-bind resin (Novagen) that had been charged

with 9 mL of charging buffer (50 mM Ni₂SO₄). The column was washed with 60 mL of His-binding buffer and 30 mL of wash buffer (60 mM imidazole, 0.5 M NaCl, 20 mM Tris HCl, pH 7.9). Subsequently, the protein was eluted using a gradient of 20 mL elute buffer (60-500 mM imidazole, 0.5 M NaCl, 20 mM Tris HCl, pH 7.9). Fractions containing InhA were collected, and the imidazole was removed using Sephadex G-25 chromatography (1.5 cm X 55 cm) with piperazine-1,4-bis(2-ethanesulfonic acid) (PIPES) buffer (30 mM PIPES, 150 mM NaCl, 1.0 mM EDTA, pH 8.0) as the buffer. The purity of the protein was shown to be > 95% by 12% SDS-PAGE, which gave an apparent molecular mass of ~28 kDa. The concentration of InhA was determined by measuring the absorption at 280 nm and using an extinction coefficient of 30,440 M⁻¹cm⁻¹, calculated from the primary sequence. The enzyme was concentrated with Centricon-30 (Centricon) concentrators and stored at -80 °C after flash freezing with liquid nitrogen.

Site-Directed Mutagenesis, Expression and Purification of InhA Mutants.

InhA mutants V203A and I215A was prepared using QuikChange site-directed mutagenesis with the primers shown in **Table 5.2**. The sequence of each mutant plasmid was confirmed by DNA sequencing. The expression and purification of each InhA mutant followed the same protocol that is described above for the wild-type InhA protein.

Table 5.2. Nucleotide primers for preparation of InhA mutants.

InhA mutant		Primer
V203A	Forward	5' GAGTGCGATCGCGGGCGGTGCGCTC 3'
	Reversed	5' GAGCGCACCGCCCGCGATCGCACTC 3'
I215A	Forward	5' CCGGCGCCCAGGCGCAGCTGCTCGAG 3'
	Reversed	5' CTCGAGCAGCTGCGCCTGGGCGCCGG 3'

Measurement of K_i Values

Measurement of K_i values was performed using the methods described in Chapter 3.

Progress Curve Analysis

InhA activity was monitored by adding enzyme (5 nM) to assay mixtures containing glycerol (8%, V/V), DMSO (2%, V/V), DD-CoA (300 μ M), NADH (250 μ M) and inhibitor (25-1000 nM). Reactions were monitored until the progress curve became linear, that is, the steady-state had been reached. Here low enzyme concentration and high substrate concentration were used to ensure that substrate depletion was minimized during the assay so that the progress curve in

the absence of inhibitors was approximately linear. Progress curves were analyzed as described previously [128, 168] by fitting data to **Equation 5.2**.

$$A_t = A_0 - v_s t - \frac{(v_i - v_s)(1 - \gamma)}{k_{obs}\gamma} \ln \left[\frac{(1 - \gamma e^{-k_{obs}t})}{1 - \gamma} \right] \quad \text{Equation 5.2}$$

In **Equation 5.2**, $\gamma = \frac{[E]}{[I]} \left(1 - \frac{v_s}{v_i} \right)^2$, and v_i and v_s are the initial velocity and steady-state velocity in the progress curve, and k_{obs} is the observed rate constant for each curve. The values of k_{obs} , v_i , and v_s obtained from **Equation 5.2**, were then fitted to **Equations 5.3** and **5.4**, which describe a two-step inhibition mechanism in which the first rapid binding of inhibitor to enzyme is followed by a second slow step that results in the final EI* complex.

$$k_{obs} = k_{-2} + \frac{k_2[I]}{K_{-1}^{app} + [I]} \quad \text{Equation 5.3}$$

$$\frac{v_i}{v_s} = 1 + \frac{[I]}{K_i^{app}} \quad \text{Equation 5.4}$$

In these equations, K_{-1}^{app} and K_i^{app} are the apparent dissociation constants for the initial enzyme-inhibitor complex (EI) and the final enzyme-inhibitor complex (EI*), respectively.

Rapid Dilution Experiments

A solution of InhA (2.5 μ M), inhibitor (2.5-7.5 μ M), NADH (250 μ M), and NAD⁺ (200 μ M) in 30 mM PIPES buffer (pH 6.8, containing 150 mM NaCl, 1.0 mM EDTA, 2% DMSO and 8% glycerol) was prepared in a total volume of 50 μ L and

incubated at rt for 30-60 min to allow the formation of the final enzyme-inhibitor complex. An aliquot of 1 μL was then taken from the mixture and immediately diluted 500-fold with the same PIPES buffer containing additional 250 μM NADH and 300 μM DD-CoA, and the reaction was initiated simultaneously by mixing the assay solution. The reaction was monitored for at least 60 min at 340 nm using a Cary 300 UV/Vis spectrometer, until the reaction rate became constant. Similar method was used to fit data using **Equation 5.2**.

Organic Synthesis

Compound **PT162** and **PT163** were prepared by Dr. Gopal B. Reddy and Sonam Shah, respectively. Other compounds were mentioned in previous chapters or cited references.

Results and Discussion

The Energy Barrier in the Transition State

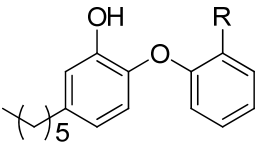
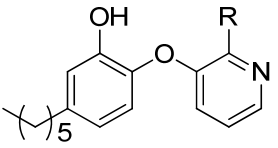
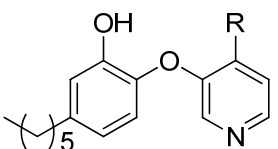
Enzyme kinetics of several diaryl ethers was tested with progress curves analysis, and t_R values were measured for slow-onset inhibitors of InhA (**Table 5.3**). As a result, ten compounds were found to be slow-onset inhibitors. Each inhibitor has an *ortho* substituent on the B-ring and showed higher binding affinity than the rapid reversible inhibitors, which implies that conformation restriction is important for slow-onset inhibition. Small hydrogen bonding acceptors gave longer residence times than small nonpolar groups, while large groups or small hydrogen bonding donors resulted in rapid reversible inhibition. The result is similar to the SAR studies of the binding affinity and indicates that both van der Waals interactions and hydrogen bonding favor slow-onset inhibition.

Compared to **PT070**, compounds **PT113**, **PT091**, and **PT092** all have comparable binding affinities (K_i) to **PT070** with similar or shorter residence times. In contrast, the only analogue with a longer residence time, **PT119** ($t_R = 80$ min), has a binding affinity that is reduced approximately 50-fold compared to **PT070**. In an attempt to rationalize these observations we determined the structures of InhA bound to **PT092** and **PT119** (**Figure 5.7**).

In both complexes of **PT092** and **PT119**, the substrate binding loop of InhA formed an α -helix and adopted a “closed” conformation (EI*), which is consistent with observations of other slow-onset inhibitors [109, 169], whereas rapid reversible inhibitors resulted in a disordered [86] or “open” conformation (EI). The

results support the correlation between slow-onset inhibition and the “closed” conformation of the substrate binding loop reported previously for FabI enzymes [111, 162].

Table 5.3. Enzyme binding kinetics of the diaryl ethers.

Compound		K_i (nM)	Slow-onset	t_R (min)	
	R				
PT004 ^a	-H	9.4 ± 0.5	No	N/A	
PT010 ^b	-NO ₂	N.D. ^d	Yes	27 ± 6	
PT013 ^b	-NH ₂	N.D. ^d	No	N/A	
PT070 ^c	-CH ₃	0.044 ± 0.005	Yes	24 ± 2	
PT091	-Cl		Yes	21 ± 3	
PT092	-Br		Yes	30 ± 3	
PT095	-CF ₃		N.D. ^d	No	N/A
PT096	-I		3.72 ± 5.13	No	N/A
PT113	-F		0.09 ± 0.02	Yes	9 ± 3
PT114	-OH	15.9 ± 3.7	No	N/A ^e	
PT119	-CN	2.14 ± 0.35	Yes	80 ± 12	
PT077 ^b	-H		N.D. ^d	No	N/A
PT130	-NH ₂		Yes	188 ± 26	
PT164	-CN		Yes	N.D. ^d	
PT161	-F		Yes	N.D. ^d	
PT115	-CN		N.D. ^d	Yes	263 ± 73

a Data taken from [86]

b Data taken from [104]

c Data taken from [109]

d Not determined.

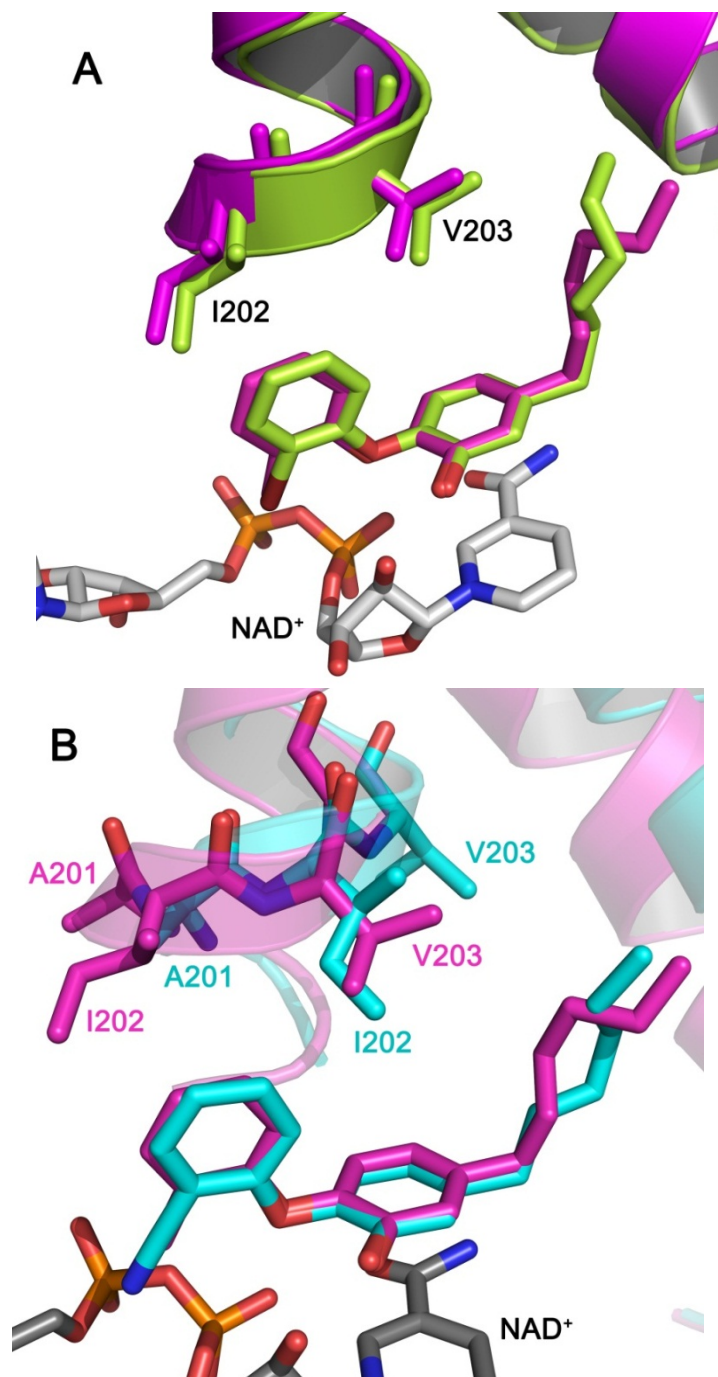


Figure 5.7. X-ray crystallographic structures of PT070, PT092, and PT119 bound to InhA.

A) Overlay of **PT070** (magenta, 2x23.pdb, [109]) and **PT092** (lime) bound to InhA respectively. **B)** Overlay of **PT070** (magenta, 2x23.pdb) and **PT119** (cyan) bound to InhA respectively. Figures were generated with PyMol.[102].

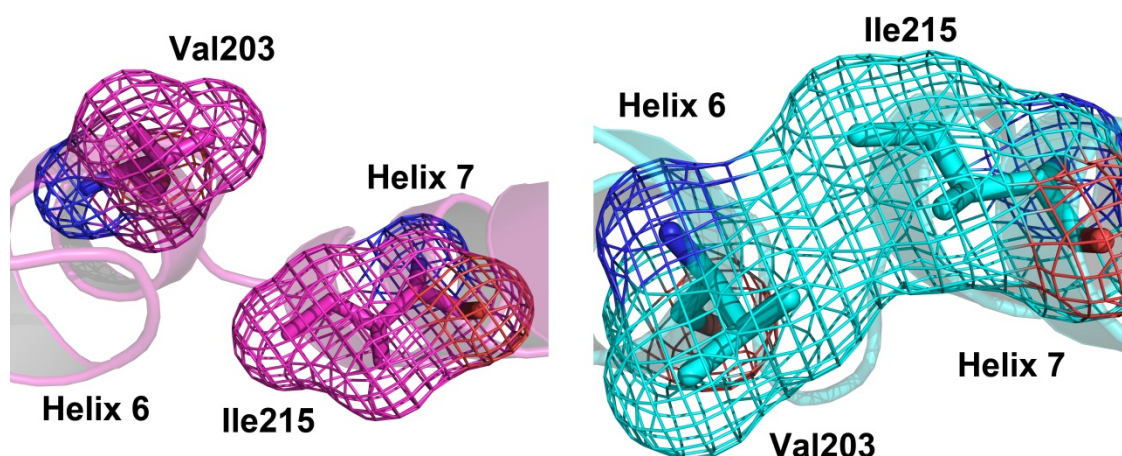


Figure 5.8. A close view of Val203 and Ile215 in the active site.

Positions of Val203 and Ile215 in the active site of InhA complexes formed with **PT070** (magenta, 2x23.pdb, [109]) and **PT119** (cyan).

The conformations of α -helices 6 and 7 conformations are almost the same in complexes of **PT070** and **PT092** (**Figure 5.7.A**), which is expected from their similar residence times and binding affinities. However, **PT119** resulted in a different “closed” conformation for the EI* complex. Because the cyano group of **PT119** is bulkier than the methyl group of **PT070**, this group displaces the B-ring of **PT119** 0.4 Å away from the helix and interacts with 2'-OH of the nicotinamide ribose through hydrogen bonding (**Figure 5.7.B**). To accommodate this change, helix 6 turns by one residue and shifts 2 Å in the direction towards the substrate binding site. As a result, Ala201, Ile202, and Val203 in the **PT119** complex replace Ile202, Val203, and Gly204 in the **PT070** complex, respectively (**Figure 5.7.B**). In particular, the side chain of Ile202 in the **PT119** complex is superimposed perfectly on Val203 in the **PT070** complex.

The movement of Val203 and Ile215 is of most interest because the side chains of these residues contact each other tightly and will sterically clash as the conformation changes (**Figure 5.8**). As a result, since the new “closed” conformation requires further motion of helix 6, **PT119** needs to traverse a higher energy transition state than **PT070**. This would account for a longer residence time despite a lower affinity (**Figure 5.9**).

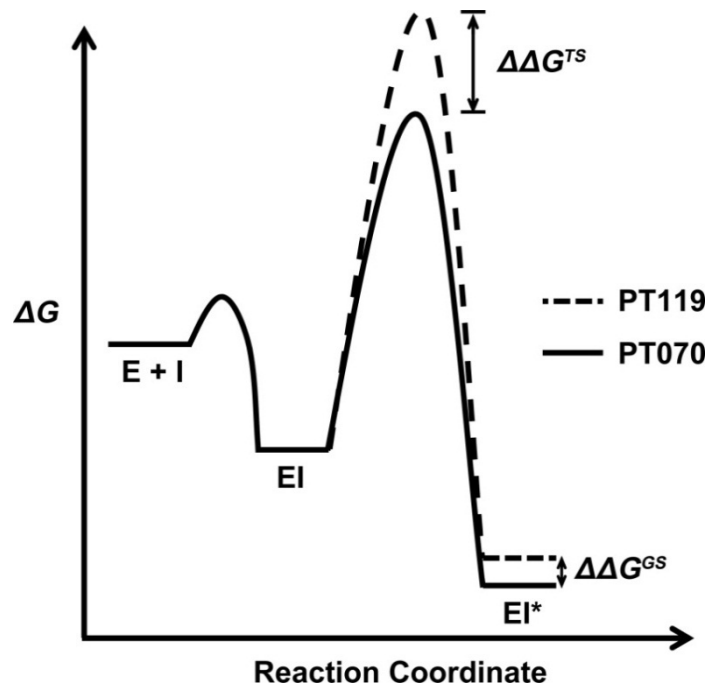


Figure 5.9. Schematic energy diagram of PT070 and PT119 binding to InhA.

The reduced binding affinity of **PT119** could be a result of less efficient interactions between Ile202 and the A-ring, compared to the situation observed for **PT070** where both Ile202 and Val203 interact with the A-ring (**Figure 5.10**). Although the EI* of **PT119** is destabilized compared to **PT070**, the transition state is even more destabilized due to the extra energy required for motion of helix 6 ($\Delta\Delta G^{\text{TS}} > \Delta\Delta G^{\text{GS}}$). As a result, the overall energy barrier between EI and EI* increased for **PT119** (**Figure 5.9**), accounting for a longer residence time.

Interesting results were seen for the diaryl ethers **PT130** and **PT115**, which have pyridyl B-rings. Both compounds showed longer residence times than their parent compounds **PT013** and **PT119**, which implies that other pyridyl B-rings may also result in longer residence times. Possible reasons may be higher binding affinities or additional transitions involving water molecules that interact with the pyridine ring. Further enzyme kinetics and crystallography studies are needed to fully understand these changes.

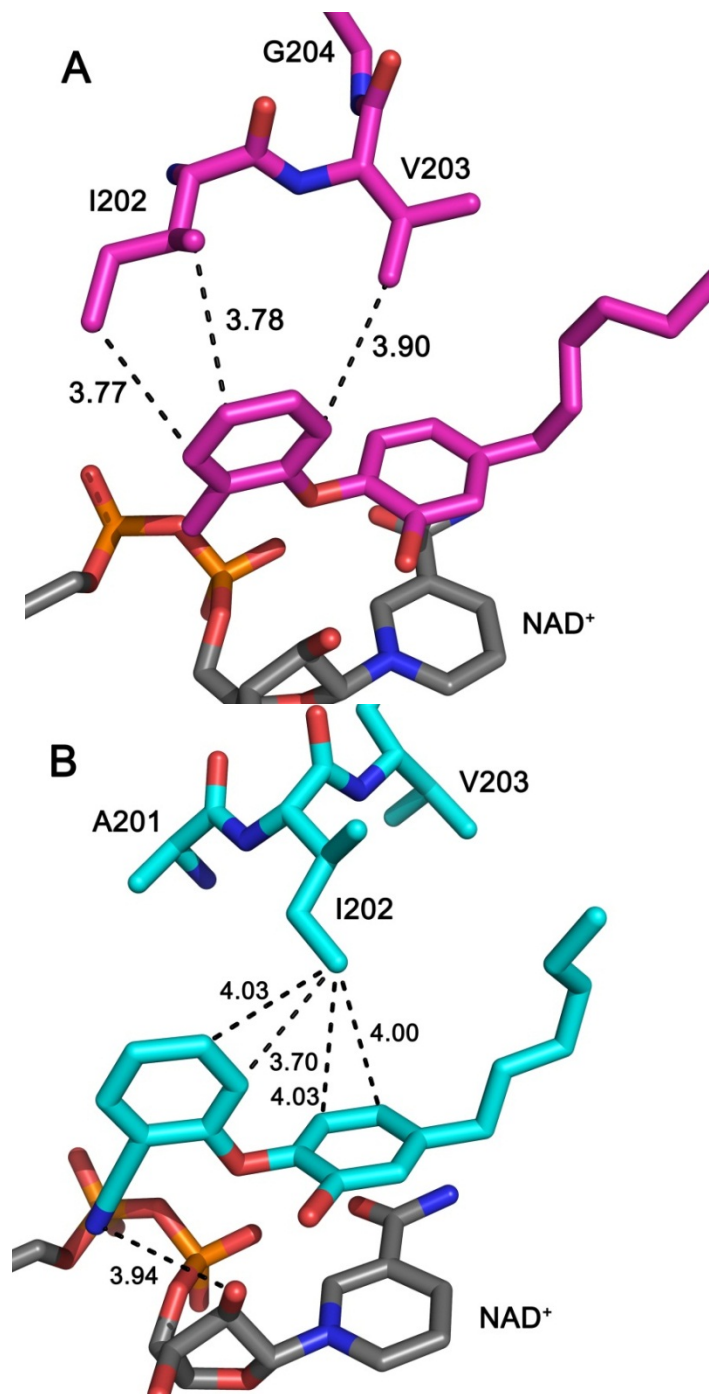


Figure 5.10. Interactions in the active sites of InhA bound to PT070 and PT119.

A) Hydrophobic interactions between the **PT070** B-ring and the substrate binding loop (magenta, 2x23.pdb [109]). **B)** Hydrophobic and hydrogen bonding interactions of the **PT119** B-ring with the substrate binding loop and cofactor (cyan). Figures were generated with PyMol [102].

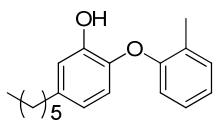
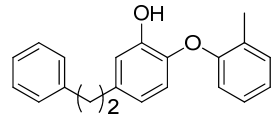
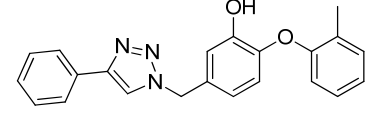
The Loop Motion Mechanism of Slow-onset Inhibition

Previous kinetic studies of the diaryl ethers suggested that the relative loop motion between helices 6 and 7 is the source of the energy barrier during the slow-onset transition. In particular, Val203 and Ile215 contribute significantly to the energy change due to van der Waals clash of these two residues. Slow-onset inhibitors should stabilize the helical conformation of the substrate binding loop in the EI* complex subsequent to a high energy barrier transition between the EI and EI* complex that lowers the association rate constant.

To evaluate the importance of V203 and I215 in enzyme inhibition the InhA mutants V203A and I215A were prepared, and the inhibition of these enzymes by **PT070** was evaluated (**Table 5.4**). Significantly, **PT070** is not a slow-onset inhibitor of either mutant, consistent with a diminished energy barrier due to reduced sizes of the van der Waals interaction pair Val203 and Ile215. This result confirmed our hypothesis that Val203 and Ile215 are the main contributors to the energy barrier. To recover slow-onset inhibition of these two mutants, the diaryl ethers **PT162** and **PT163** were designed to have bulkier substituents on the A-ring. **PT162** has a phenyl group that should compensate for the loss of Val203 by interacting with Ile215. Indeed, kinetic results showed that **PT162** recovered slow-onset inhibition to InhA mutant V203A, with a t_R of 13.6 min. However, it is not a slow-binding inhibitor of the InhA mutant I215A. Ile215 is farther away from the diaryl ether scaffold, thereby requiring a longer linker length. Accordingly, **PT163** was synthesized and demonstrated the predicted slow-onset inhibition to

InhA mutant I215A with a t_R of 71.4 min. These results confirmed the loop motion mechanism of slow-onset inhibition, where van der Waals interactions between Val203 and Ile215 are the primary origin of the energy barrier between EI and EI*. Significantly, our design of new slow-onset inhibitors of mutant InhA showed that rational modulation of transition state energy to prolong t_R is possible.

Table 5.4. Binding kinetics of the diaryl ethers to InhA and its mutants.

Compound	wt InhA	V203A	I215A
PT070^a 	Slow-onset $t_R = 24 \pm 2$ min	Rapid reversible	Rapid reversible
PT162 	Rapid reversible	Slow-onset $t_R = 13.6 \pm 2.1$ min	Rapid reversible
PT163 	Slow-onset $t_R = 25.3 \pm 2.6$ min	N.D. ^b	Slow-onset $t_R = 71.4 \pm 4.2$ min

^a Data taken from [109]

^b Not determined.

Identification of Rapid-On Slow-Off Inhibitors

Progress curves analysis monitors the forward process of an enzyme catalyzed reaction to detect the slow transition from the EI complex to the EI* complex (**Figure 5.11.A**). The method however does not identify inhibitors that form the EI* complex rapidly and dissociate slowly. In this case, the energy barrier of dissociation is composed mainly by the thermodynamic stabilization of the EI* complex since there is a low energy barrier to association (**Figure 5.11.B**). In general, the thermodynamic stabilization needed to observe slow dissociation kinetics is consistent with tight-binding inhibition.

To characterize rapid-on slow-off InhA inhibitors, concentrated assay solutions were rapidly diluted and tested with progress curves analysis. Three such inhibitors were identified, and their t_R values were measured (**Table 5.5**).

The overall energy change from the free enzyme to the final complex was calculated to be 51.5 kJ/mol using the K_i value and **Equation 5.5**.

$$\Delta G = -RT \ln K_i \qquad \text{Equation 5.5}$$

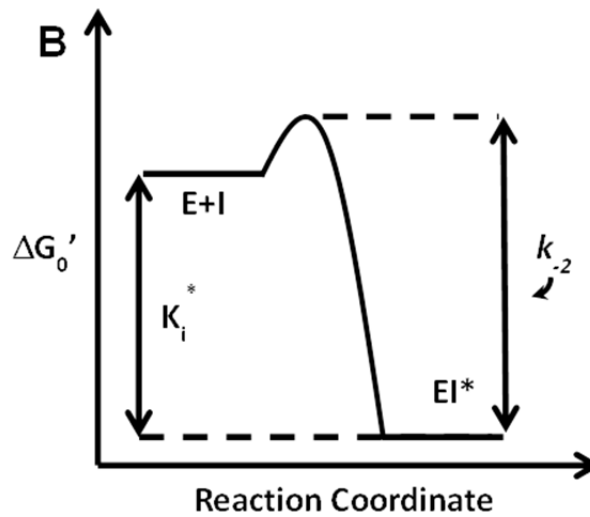
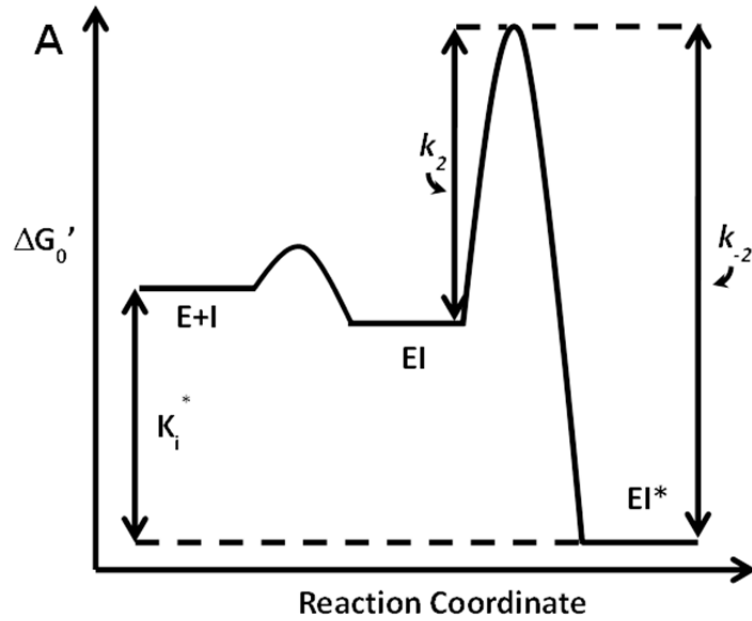


Figure 5.11. Schematic reaction coordinate for slow-off inhibitors.

A) Slow-onset inhibitors that form the EI^* complex slowly, with detectable energy barriers in both forward and backward transition. **B)** Tight binding slow-off inhibitors that form the EI^* complex rapidly, with an energy barrier only from the EI^* to EI complex (or to the free enzyme).

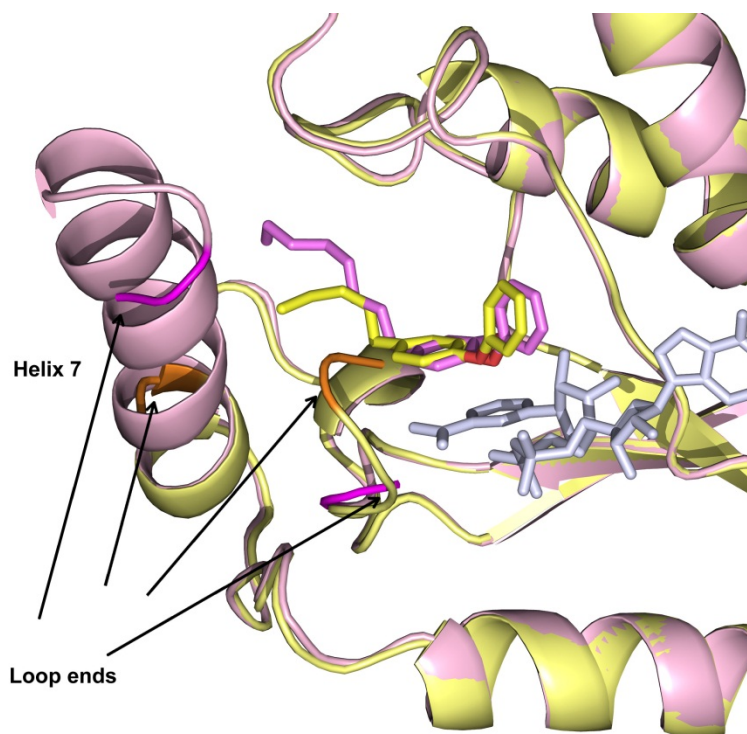
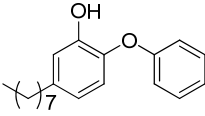
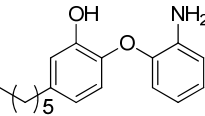
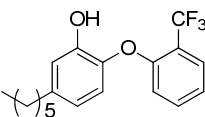


Figure 5.12. The substrate binding loop in InhA complex with PT003 and PT005.

The substrate binding loop in the complex of InhA and **PT005** (pink, 2b37.pdb, [86]) showed helix 7 and disordered helix 6, while the complex of InhA and **PT003** showed both helices 6 and 7 disordered (yellow, 2b36.pdb, [86]). The ends of the missing electron density are labeled in magenta and orange for the complexes with **PT005** and **PT003**, respectively.

Table 5.5. Rapid-on slow-off InhA inhibitors.

Compound	t_R (min)	IC_{50} (nM)	K_i (nM)
PT005 	17 ± 5.3	5.0 ± 0.3	1.1 ± 0.2
PT013 	5.2 ± 1.2	61.9 ± 4.5	N.D. ^a
PT095 	9.1 ± 2.3	29.65 ± 5.1	N.D. ^a

^a Not determined.

Based on the kinetics and crystallographic structures of **PT070** (2x22.pdb [109]) and **PT003** (2b36.pdb, [86]), an substrate binding loop that is ordered and forms α -helices 6 and 7 is correlated with slow-onset inhibition of InhA. Interestingly, the X-ray crystallographic structure of rapid-on slow-off inhibitor **PT005** revealed a partly helical structure of the substrate binding loop (**Figure 5.12**), in which helix 7 is ordered, while both helices 6 and 7 are missing in the structure of **PT003**. This structural evidence further confirmed the correlation between slow-onset inhibition and motion of the substrate binding loop.

In Vivo Efficacy of Slow-onset Diaryl Ethers

Previously, we showed that *in vivo* efficacy of slow-onset diaryl ether inhibitors of *ftuFabI* is correlated only to their t_R , using *Francisella tularensis* infected mice model (Figure 5.4). To explore this correlation in *M. tuberculosis* infected mice, **PT004**, **PT070** and **PT091** were synthesized in large scales (grams) and tested in the short-term mouse model of TB infection.

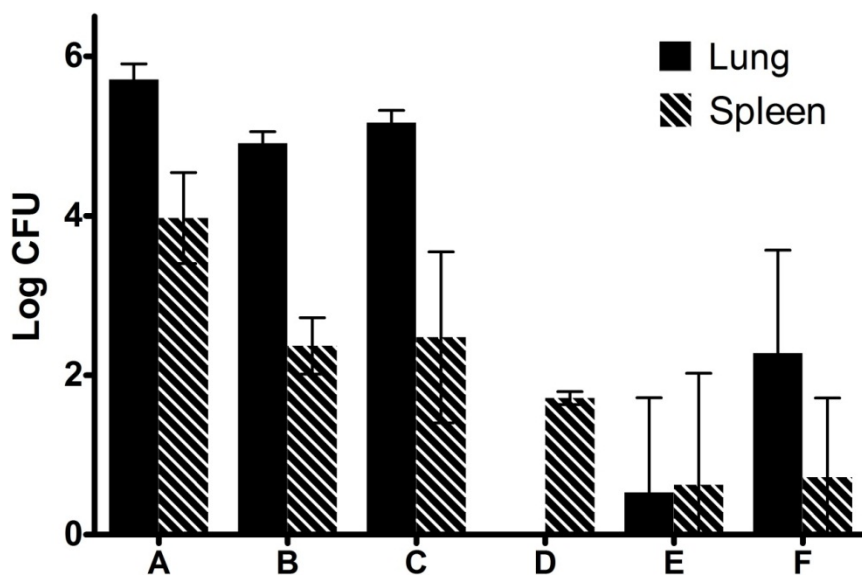


Figure 5.13. *In vivo* efficacy of PT070 and PT091.

In vivo efficacy of **PT070**, **PT091**, isoniazid, ethambutol, and rifampin, orally administrated (PO) once per day (SID). **A**) Control. **B**) **PT070**, 200 mg/kg, 200 μ L. **C**) **PT091**, 200 mg/kg, 200 μ L. **D**) Isoniazid, 25 mg/kg, 100 μ L. **E**) Ethambutol, 100 mg/kg, 100 μ L. **F**) Rifampin, 10 mg/kg, 100 μ L. Experiments were performed by Susan Knudson, Colorado State University.

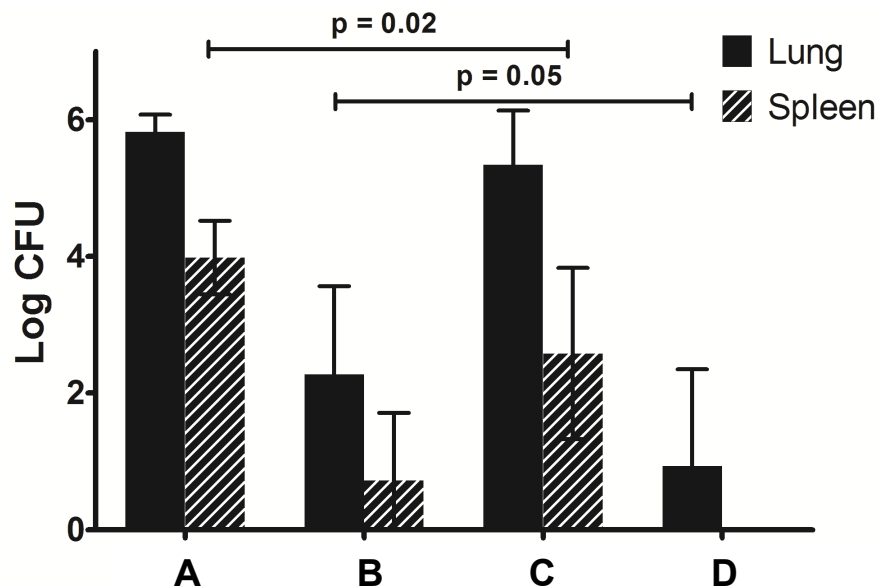


Figure 5.14. *In vivo* efficacy of PT091 (IP).

In vivo efficacy of **PT070**, **PT091**, and rifampin administrated by intraperitoneal injection (IP) SID. **A)** Control. **B)** Rifampin, 10 mg/kg. **C)** **PT091**, 200 mg/kg. **D)** **PT091**, 50 mg/kg and rifampin, 10 mg/kg. Experiments were performed by Susan Knudson, Colorado State University.

As expected, the rapid reversible inhibitor **PT004** did not show any *in vivo* efficacy, while slow-onset inhibitors **PT070** and **PT091** both showed decreases of 1 log unit and 2 log units in lung and spleen colony formation unit (CFU) (**Figure 5.13**). In addition, **PT091** showed synergistic efficacy with rifampicin, completely killing *M. tuberculosis* in spleen and decreasing the liver CFU by 5 log units. The results confirmed the correlation between the residence time of inhibitor-target complex and *in vivo* efficacy, and support the opinion that drug-target complex residence time should be included as an important criterion in drug development. The synergistic efficacy also showed the prospect of the diaryl ethers being used in combination therapy of TB.

Summary

To understand the mechanism of slow-onset inhibition, progress curve analysis was used to identify ten slow-onset diaryl ether inhibitors of InhA. All of them have an *ortho* substituent on the B-ring, which suggests that restricting rotation around the diphenyl ether linkage may be important for time-dependent InhA inhibition by this class of compounds. Similar to the SAR results of the binding affinities, small hydrogen bonding acceptors gave longer residence times than small nonpolar groups, which indicates that both hydrogen bonding and van der Waals interactions promote slow-onset inhibition.

The slow-onset inhibitor **PT119** was found to have a longer residence time but weaker binding affinity than **PT070**. Comparison of the X-ray crystallographic structures of InhA complexes with both compounds confirmed the loop motion mechanism for slow-onset inhibition of InhA and implied that the energy barrier for the transition is mainly a result of steric clashes between Val203 and Ile215. To test this hypothesis, the InhA mutants V203A and I215A were prepared in order to reduce the steric hindrance between their respective side chains, which resulted in the loss of slow-onset inhibition of InhA by **PT070**. Compound **PT162** and **PT163** were designed to complement changes in residue sizes and were shown to be slow-onset inhibitors of the InhA mutants. These results confirmed the role of interactions between Val203 and Ile215 in slow-onset inhibition and provided an example that our understanding of slow-onset mechanism would substantiate the modulation of residence times.

Rapid dilution experiments were performed to identify tight binding slow-onset inhibitors and measure their residence times. With MD simulations and direct measurement of inhibitor dissociation, residence times were correlated to the activation energy and using the K_i values, the forward energy barrier was also calculated.

The diaryl ethers **PT004**, **PT070**, and **PT091** were synthesized in large scale and tested in the short-term *M. tuberculosis* infection model. The results showed that only slow-onset inhibitors **PT070** and **PT091** had *in vivo* efficacy, which supports the correlation between *in vivo* efficacy and drug-target residence time. In addition, the synergistic effect of **PT091** and rifampicin supports the possible use of the diaryl ethers in combination therapy of TB.

Conclusions and Future Work

Derivatives with diaryl ether and 4-pyridone scaffolds were synthesized, and their inhibitory activities to InhA and *M. tuberculosis* growth were evaluated to understand the SAR of these series of InhA inhibitors. With crystallography and computational simulation data, the interactions in the binding pocket were outlined.

Progress curve analysis was used to identify time-dependent inhibitors and to measure residence time of inhibition-enzyme complexes. The results confirmed the hypothesis that slow-onset inhibition of InhA is correlated with the closed conformations of helices 6 and 7, where Val203 and Ile215 are essential van der Waals interaction partners that contribute to the energy barrier of the transition state.

SAR on the A-Ring of the Diaryl Ethers

Previous SAR studies on the A-ring substituents showed that linear alkyl groups with 6-8 carbon atoms resulted in the best activity of the diaryl ethers [86], while in this research project, various groups were introduced into the A-ring of the diaryl ethers and revealed more detailed SAR.

Generally, hydrophobic substituents are preferred on the A-ring, as the binding area contains mostly hydrophobic residues. A benzyl group resulted in the same IC₅₀ and MIC values, compared to a hexyl group, suggesting that a

cyclic group well mimics the conformation of linear alkyl groups. The observation is also supported by crystallographic structures of inhibitors with linear and cyclic groups (**Figure 2.5**).

A linker between the cyclic group and the A-ring is necessary, and a methylene linker resulted in the best activity. Ether linkers showed similar IC₅₀ values and higher MIC values than parent compounds. Amino substituents resulted in weak binding affinity to InhA.

Compared to linear substituents, cyclic groups retained activities and lowered flexibility of the diaryl ethers, which should reduce entropy change and favor binding to InhA. Therefore, a hydrophobic cyclic group with a methylene linker to the A-ring would be the best choice for the A-ring substituent in future optimization.

SAR on the B-Ring of the Diaryl Ethers

The binding affinity of the diaryl ethers is known to be sensitive to the size of substituents on the B-ring [104]. SAR studies with various B-ring substituents showed that an *ortho* group containing more than two heavy atoms will significantly decrease the binding affinity. Nonpolar and electron withdrawing groups, especially small halogen atoms, are preferred on the *ortho* position of the B-ring. Introduction of groups on both *ortho* positions resulted in a loss of binding affinity, mainly because the steric hindrance of the two groups resulted in high internal energy and disfavored binding to the active site.

Studies on pyridyl B-rings showed similar SAR to phenyl B-rings, while 2'-N pyridyl B-rings resulted in better activities than 4'-N pyridyl B-rings, which can be explained by potential hydrogen bonding interactions between 2'-N and surrounding residues (**Figure 3.7**). Compared to phenyl compounds, 2'-N pyridyl inhibitors showed lower MIC values, probably due to enhanced cell uptake, and thus 2'-N pyridyl B-ring should be used in future design of the diaryl ethers.

SAR of the Pyranones and Pyridones

InhA inhibitors containing 4-pyranones and 4-pyridones as the A-ring were synthesized, aiming at metabolic stability and hydrophilicity. SAR of the new scaffolds was also studied with their derivatives.

Similar to the diaryl ethers, a hexyl group on the A-ring is preferred for the 4-pyranones and 4-pyridones, and an *ortho* methyl group on the B-ring improved binding affinity significantly. The 4-pyridone A-ring always resulted in better activities than the 4-pyranones, which indicates that the 4-pyridone is a better scaffold.

More detailed SAR studies on the 4-pyridones showed that small B-ring substituents are preferred on the *ortho* position. The 4-pyridones with 2'-N pyridyl B-rings were also synthesized to improve *in vitro* activities. Contrary to the diaryl ethers, the 4-pyridones prefer an *ortho* amino group over a fluorine atom, which can be explained by different conformations of InhA complexes with the diaryl ethers and the 4-pyridones bound (**Figure 4.7**).

Pharmacokinetic studies showed that the 4-pyridone **PT166** has an AUC/MIC value 5 fold higher than the diaryl ethers **PT001** and **PT119**, while **PT166** and **PT119** showed similar MIC against *M. tuberculosis*. Therefore, the 4-pyridone is a promising scaffold to improve the *in vivo* activity against TB.

Mechanisms of Slow-Onset Inhibition of InhA

To understand the role of the B-ring *ortho* substituents in slow-onset inhibition, progress curve analysis was used to identify and evaluate slow-onset InhA inhibitors. The data showed that *ortho* nonpolar and electron withdrawing groups are preferred for slow-onset inhibition, which suggests that both conformation restriction and the interactions between *ortho* substituents and active site residues are important to slow-onset inhibition.

Enzyme kinetic, crystallographic, and computational results of **PT070** and **PT119** suggest that the energy barrier of the transition state in slow-onset inhibition is mainly caused by steric clashes between residues Val203 and Ile215. InhA mutants **V203A** and **I215A** lost slow-onset inhibition with **PT070**, which confirms the important roles of Val203 and Ile215. Furthermore, bulkier inhibitors **PT162** and **PT163** were synthesized to compensate the loss in size of Val203 and Ile215. **PT162** regained slow-onset inhibition against InhA mutant V203A, and **PT163** elongated the residence time to InhA mutant I215A by 3 fold.

In the end, the *in vivo* activity of **PT004**, **PT070**, and **PT091** were evaluated in *M. tuberculosis* infected short-term mice model. The results showed that slow-

onset inhibitors **PT070** and **PT091** reduced CFU in the lung and spleen by 1 and 2.5 log units, respectively. While rapidly reversible inhibitor **PT004** did not show significant *in vivo* efficacy. The result confirmed the correlation between residence time and *in vivo* efficacy.

References

1. Donoghue, H.D., et al., *Tuberculosis: from prehistory to Robert Koch, as revealed by ancient DNA*. Lancet Infect. Dis., 2004. **4**(9): p. 584-592.
2. Wright, A., et al., *Emergence of Mycobacterium tuberculosis with extensive resistance to second-line drugs - Worldwide, 2000-2004 (Reprinted from MMWR, vol 55, pg 301-305, 2006)*. Jama-Journal of the American Medical Association, 2006. **295**(20): p. 2349-2351.
3. WHO, *Global tuberculosis control 2011*, 2011.
4. Scheindlin, S., *The fight against tuberculosis*. Mol. Interventions, 2006. **6**(3): p. 124-130.
5. Kaufmann Stefan, H.E., *Robert Koch, the Nobel Prize, and the ongoing threat of tuberculosis*. N. Engl. J. Med., 2005. **353**(23): p. 2423-2426.
6. Madkour, M.M., *Textbook of tuberculosis* 2003, New York: Springer.
7. Ryan, K.J. and J.C. Sherris, *Sherris medical microbiology*. 3rd ed 1994, Norwalk, Conn.: Appleton & Lange. xiii, 890 p.
8. Cox, R.A., *Quantitative relationships for specific growth rates and macromolecular compositions of Mycobacterium tuberculosis, Streptomyces coelicolor A3(2) and Escherichia coli B/r: an integrative theoretical approach*. Microbiology, 2004. **150**(Pt 5): p. 1413-1426.
9. Hiriyanna, K.T. and T. Ramakrishnan, *Deoxyribonucleic-acid replication time in Mycobacterium tuberculosis H37Rv*. Arch. Microbiol., 1986. **144**(2): p. 105-109.

10. Russell, D.G., C.E. Barry, and J.L. Flynn, *Tuberculosis: What we don't know can, and does, hurt Us*. Science, 2010. **328**(5980): p. 852-856.
11. Clemens, D.L., *Characterization of the Mycobacterium tuberculosis phagosome*. Trends Microbiol., 1996. **4**(3): p. 113-118.
12. Russell, D.G., et al., *Foamy macrophages and the progression of the human tuberculosis granuloma*. Nat. Immunol., 2009. **10**(9): p. 943-948.
13. Vogt, G. and C. Nathan, *In vitro differentiation of human macrophages with enhanced antimycobacterial activity*. J. Clin. Invest., 2011. **121**(10): p. 3889-3901.
14. Kumar, V. and S.L. Robbins, *Robbins basic pathology*. 8th ed2007, Philadelphia, PA: Saunders/Elsevier. xiv, 946 p.
15. Bloom, B.R. and C.J. Murray, *Tuberculosis: commentary on a reemergent killer*. Science, 1992. **257**(5073): p. 1055-1064.
16. Espinal, M.A., *The global situation of MDR-TB*. Tuberculosis, 2003. **83**(1-3): p. 44-51.
17. Oliveira, J.S., et al., *Enoyl reductases as targets for the development of anti-tubercular and anti-malarial agents*. Curr. Drug Targets, 2007. **8**(3): p. 399-411.
18. WHO, *Tuberculosis facts 2009*. 2009.
19. WHO, *MDR and XDR-TB progress report 2011 - fact sheet*. 2011.
20. WHO, *HIV and TB (TB/HIV) - fact sheet*, 2011.
21. Kochi, A., *The global tuberculosis situation and the new control strategy of the World Health Organization*. Tubercle, 1991. **72**(1): p. 1-6.

22. Rattan, A., A. Kalia, and N. Ahmad, *Multidrug-resistant Mycobacterium tuberculosis: molecular perspectives*. *Emerg. Infect. Dis.*, 1998. **4**(2): p. 195-209.
23. Centers for Disease Control and Prevention, N.C.f.H.A., Viral Hepatitis, STD, and TB Prevention, Division of Tuberculosis Elimination, *Core curriculum on tuberculosis: What the clinician should know*, 2011.
24. Truffot-Pernot, C. and E. Cambau, [*Bacteriological diagnosis of tuberculosis*]. *Rev. Pneumol. Clin.*, 1994. **50**(5): p. 240-246.
25. Orme, I.M., *Vaccination against tuberculosis: Recent progress*. *Advances in Veterinary Medicine*, Vol 41, 1999. **41**: p. 135-143.
26. Verma, I. and A. Grover, *Antituberculous vaccine development: a perspective for the endemic world*. *Expert Rev. Vaccines*, 2009. **8**(11): p. 1547-1553.
27. Huebner, R.E. and K.G. Castro, *The changing face of tuberculosis*. *Annu. Rev. Med.*, 1995. **46**: p. 47-55.
28. World Health Organization. and Stop TB Initiative (World Health Organization), *Treatment of tuberculosis : guidelines*. 4th ed2010, Geneva: World Health Organization. x, 147 p.
29. Gupta, P., et al., *Simultaneous ethambutol & isoniazid resistance in clinical isolates of Mycobacterium tuberculosis*. *Indian J. Med. Res.*, 2006. **123**(2): p. 125-130.
30. Zhang, Y. and L.M. Amzel, *Tuberculosis drug targets*. *Curr. Drug Targets*, 2002. **3**(2): p. 131-154.

31. Schroeder, E.K., et al., *Drugs that inhibit mycolic acid biosynthesis in Mycobacterium tuberculosis*. *Curr. Pharm. Biotechnol.*, 2002. **3**(3): p. 197-225.
32. Qian, L. and P.R.O. de Montellano, *Oxidative activation of thiacetazone by the Mycobacterium tuberculosis flavin monooxygenase EtaA and human FMO1 and FMO3*. *Chem. Res. Toxicol.*, 2006. **19**(3): p. 443-449.
33. Hanouille, X., et al., *Selective intracellular accumulation of the major metabolite issued from the activation of the prodrug ethionamide in mycobacteria*. *J. Antimicrob. Chemother.*, 2006. **58**(4): p. 768-772.
34. Morlock, G.P., et al., *ethA, inhA, and katG loci of ethionamide-resistant clinical Mycobacterium tuberculosis isolates*. *Antimicrob. Agents Chemother.*, 2003. **47**(12): p. 3799-3805.
35. Heifets, L.B., M.A. Flory, and P.J. Lindholmlevy, *Does pyrazinoic acid as an active moiety of pyrazinamide have specific activity against Mycobacterium tuberculosis*. *Antimicrob. Agents Chemother.*, 1989. **33**(8): p. 1252-1254.
36. Zimhony, O., et al., *Pyrazinamide inhibits the eukaryotic-like fatty acid synthetase I (FASI) of Mycobacterium tuberculosis*. *Nat. Med.*, 2000. **6**(9): p. 1043-1047.
37. Zhang, Y., et al., *Role of acid pH and deficient efflux of pyrazinoic acid in unique susceptibility of Mycobacterium tuberculosis to pyrazinamide*. *J. Bacteriol.*, 1999. **181**(7): p. 2044-2049.

38. Shi, W.L., et al., *Pyrazinamide inhibits trans-translation in Mycobacterium tuberculosis*. *Science*, 2011. **333**(6049): p. 1630-1632.
39. Takayama, K. and J.O. Kilburn, *Inhibition of synthesis of arabinogalactan by ethambutol in Mycobacterium smegmatis*. *Antimicrob. Agents Chemother.*, 1989. **33**(9): p. 1493-1499.
40. Khoo, K.H., et al., *Truncated structural variants of lipoarabinomannan in ethambutol drug-resistant strains of Mycobacterium smegmatis. Inhibition of arabinan biosynthesis by ethambutol*. *J. Biol. Chem.*, 1996. **271**(45): p. 28682-28690.
41. Dong, X., et al., *Development of a quantitative assay for mycobacterial endogenous arabinase and ensuing studies of arabinase levels and arabinan metabolism in Mycobacterium smegmatis*. *Appl. Environ. Microbiol.*, 2006. **72**(4): p. 2601-2605.
42. Caceres, N.E., et al., *Overexpression of the D-alanine racemase gene confers resistance to D-cycloserine in Mycobacterium smegmatis*. *J. Bacteriol.*, 1997. **179**(16): p. 5046-5055.
43. David, H.L., K. Takayama, and D.S. Goldman, *Susceptibility of mycobacterial D-alanyl-D-alanine synthetase to D-cycloserine*. *Am. Rev. Respir. Dis.*, 1969. **100**(4): p. 579-581.
44. Buynak, J.D., *Understanding the longevity of the beta-lactam antibiotics and of antibiotic/beta-lactamase inhibitor combinations*. *Biochem. Pharmacol.*, 2006. **71**(7): p. 930-940.

45. Reddy, V.M., J.F. O'Sullivan, and P.R. Gangadharam, *Antimycobacterial activities of riminophenazines*. J. Antimicrob. Chemother., 1999. **43**(5): p. 615-623.
46. Busscher, G.F., F.P. Rutjes, and F.L. van Delft, *2-Deoxystreptamine: central scaffold of aminoglycoside antibiotics*. Chem. Rev., 2005. **105**(3): p. 775-791.
47. Carter, A.P., et al., *Functional insights from the structure of the 30S ribosomal subunit and its interactions with antibiotics*. Nature, 2000. **407**(6802): p. 340-348.
48. Kannan, K. and A.S. Mankin, *Macrolide antibiotics in the ribosome exit tunnel: species-specific binding and action*. Ann. N. Y. Acad. Sci., 2011. **1241**: p. 33-47.
49. Swaney, S.M., et al., *The oxazolidinone linezolid inhibits initiation of protein synthesis in bacteria*. Antimicrob. Agents Chemother., 1998. **42**(12): p. 3251-3255.
50. Long, K.S., et al., *Interaction of pleuromutilin derivatives with the ribosomal peptidyl transferase center*. Antimicrob. Agents Chemother., 2006. **50**(4): p. 1458-1462.
51. Pucci, M.J., et al., *Antimicrobial evaluation of nocathiacins, a thiazole peptide class of antibiotics*. Antimicrob. Agents Chemother., 2004. **48**(10): p. 3697-3701.
52. Janin Yves, L., *Antituberculosis drugs: ten years of research*. Bioorg. Med. Chem., 2007. **15**(7): p. 2479-2513.

53. Potkar, C., et al., *Phase I pharmacokinetic study of a new 3-azinomethyl-rifamycin (rifametane) as compared to rifampicin*. *Chemotherapy*, 1999. **45**(3): p. 147-153.
54. Champoux, J.J., *DNA topoisomerases: structure, function, and mechanism*. *Annu. Rev. Biochem.*, 2001. **70**: p. 369-413.
55. Rengarajan, J., et al., *The folate pathway is a target for resistance to the drug para-aminosalicylic acid (PAS) in mycobacteria*. *Mol. Microbiol.*, 2004. **53**(1): p. 275-282.
56. Kumar, K., et al., *Discovery of anti-TB agents that target the cell-division protein FtsZ*. *Future Medicinal Chemistry*, 2010. **2**(8): p. 1305-1323.
57. Li, X.K., et al., *CoA adducts of 4-oxo-4-phenylbut-2-enoates: Inhibitors of MenB from the M. tuberculosis menaquinone biosynthesis pathway*. *Acs Medicinal Chemistry Letters*, 2011. **2**(11): p. 818-823.
58. Debnath, J., et al., *Discovery of selective menaquinone biosynthesis inhibitors against Mycobacterium tuberculosis*. *J. Med. Chem.*, 2012.
59. Marriner, G.A., et al., *The medicinal chemistry of tuberculosis chemotherapy*. *Topics in Medicinal Chemistry*, 2011. **7**: p. 47-124.
60. Barry, C.E., et al., *Mycolic acids: Structure, biosynthesis and physiological functions*. *Prog. Lipid. Res.*, 1998. **37**(2-3): p. 143-179.
61. Brennan, P.J. and H. Nikaido, *The envelope of mycobacteria*. *Ann. Rev. Biochem.*, 1995. **64**: p. 29-63.

62. Weidenmaier, C. and A. Peschel, *Teichoic acids and related cell-wall glycopolymers in Gram-positive physiology and host interactions*. Nat. Rev. Microbiol., 2008. **6**(4): p. 276-287.
63. Dessen, A., et al., *Crystal-structure and function of the isoniazid target of Mycobacterium tuberculosis*. Science, 1995. **267**(5204): p. 1638-1641.
64. Banerjee, A., et al., *inhA, a gene encoding a target for isoniazid and ethionamide in Mycobacterium tuberculosis*. Science, 1994. **263**(5144): p. 227-230.
65. Banerjee, A., et al., *inhA, a Gene Encoding a Target for Isoniazid and Ethionamide in Mycobacterium tuberculosis*. Science, 1994. **263**(5144): p. 227-230.
66. Quemard, A., et al., *Enzymatic characterization of the target for isoniazid in Mycobacterium tuberculosis*. Biochemistry, 1995. **34**(26): p. 8235-8241.
67. Rozwarski, D.A., et al., *Modification of the NADH of the isoniazid target (InhA) from Mycobacterium tuberculosis*. Science, 1998. **279**(5347): p. 98-102.
68. Rawat, R., A. Whitty, and P.J. Tonge, *The isoniazid-NAD adduct is a slow, tight-binding inhibitor of InhA, the Mycobacterium tuberculosis enoyl reductase: Adduct affinity and drug resistance*. Proc. Natl. Acad. Sci. U. S. A., 2003. **100**(24): p. 13881-13886.
69. Vilcheze, C., et al., *Inactivation of the inhA-encoded fatty acid synthase II (FASII) enoyl-acyl carrier protein reductase induces accumulation of the*

- FAI end products and cell lysis of Mycobacterium smegmatis*. J. Bacteriol., 2000. **182**(14): p. 4059-4067.
70. Zhang, Y., et al., *The catalase-peroxidase gene and isoniazid resistance of Mycobacterium tuberculosis*. Nature, 1992. **358**(6387): p. 591-593.
71. Broussy, S., et al., *The first chemical synthesis of the core structure of the benzoylhydrazine-NAD adduct, a competitive inhibitor of the Mycobacterium tuberculosis enoyl reductase*. J. Org. Chem., 2005. **70**(25): p. 10502-10510.
72. Bonnac, L., et al., *Synthesis of 4-phenoxybenzamide adenine dinucleotide as NAD analogue with inhibitory activity against enoyl-ACP reductase (InhA) of Mycobacterium tuberculosis*. Bioorg. Med. Chem. Lett., 2007. **17**(16): p. 4588-4591.
73. Hogenauer, G. and M. Woisetschlager, *A diazaborine derivative inhibits lipopolysaccharide biosynthesis*. Nature, 1981. **293**(5834): p. 662-664.
74. Baldock, C., et al., *A mechanism of drug action revealed by structural studies of enoyl reductase*. Science, 1996. **274**(5295): p. 2107-2110.
75. Baldock, C., et al., *Mechanism of action of diazaborines*. Biochem. Pharmacol., 1998. **55**(10): p. 1541-1550.
76. de Boer, G.J., et al., *Molecular genetic analysis of enoyl-acyl carrier protein reductase inhibition by diazaborine*. Mol. Microbiol., 1999. **31**(2): p. 443-450.

77. Roujeinikova, A., et al., *Inhibitor binding studies on enoyl reductase reveal conformational changes related to substrate recognition*. J. Biol. Chem., 1999. **274**(43): p. 30811-30817.
78. Levy, C.W., et al., *A study of the structure-activity relationship for diazaborine inhibition of Escherichia coli enoyl-ACP reductase*. J. Mol. Biol., 2001. **309**(1): p. 171-180.
79. Delano, W.L., *The PyMOL Molecular Graphics System* <http://www.pymol.org>, 2002.
80. Davis, M.C., S.G. Franzblau, and A.R. Martin, *Syntheses and evaluation of benzodiazaborine compounds against M. tuberculosis H37Rv in vitro*. Bioorg. Med. Chem. Lett., 1998. **8**(7): p. 843-846.
81. Musser, J.M., et al., *Characterization of the catalase-peroxidase gene (katG) and inhA locus in isoniazid-resistant and -susceptible strains of Mycobacterium tuberculosis by automated DNA sequencing: restricted array of mutations associated with drug resistance*. J. Infect. Dis., 1996. **173**(1): p. 196-202.
82. Ramaswamy, S.V., et al., *Single nucleotide polymorphisms in genes associated with isoniazid resistance in Mycobacterium tuberculosis*. Antimicrob. Agents Chemother., 2003. **47**(4): p. 1241-1250.
83. Lei, B.F., C.J. Wei, and S.C. Tu, *Action mechanism of antitubercular isoniazid - Activation mycobacterium tuberculosis KatG, isolation, and characterization of InhA inhibitor*. J. Biol. Chem., 2000. **275**(4): p. 2520-2526.

84. Timmins, G.S. and V. Deretic, *Mechanisms of action of isoniazid*. Mol. Microbiol., 2006. **62**(5): p. 1220-1227.
85. Sullivan, T.J., et al., *High affinity InhA inhibitors with activity against drug-resistant strains of Mycobacterium tuberculosis*. ACS Chem. Biol., 2006. **1**(1): p. 43-53.
86. Sullivan, T.J., et al., *High affinity InhA inhibitors with activity against drug-resistant strains of Mycobacterium tuberculosis*. ACS Chem. Biol., 2006. **1**(1): p. 43-53.
87. He, X., et al., *Pyrrolidine Carboxamides as a Novel Class of Inhibitors of Enoyl Acyl Carrier Protein Reductase from Mycobacterium tuberculosis*. J. Med. Chem., 2006. **49**(21): p. 6308-6323.
88. Kuo, M.R., et al., *Targeting tuberculosis and malaria through inhibition of enoyl reductase: Compound activity and structural data*. J. Biol. Chem., 2003. **278**(23): p. 20851-20859.
89. Staveski, M.M., et al., *InhA inhibitors and methods of use thereof*, 2002, (Genzyme Corporation, USA). Application: US. p. 32 pp.
90. He, X., A. Alian, and P.R. Ortiz de Montellano, *Inhibition of the Mycobacterium tuberculosis enoyl acyl carrier protein reductase InhA by arylamides*. Bioorg. Med. Chem., 2007. **15**(21): p. 6649-6658.
91. Copeland, R.A., D.L. Pompliano, and T.D. Meek, *Drug-target residence time and its implications for lead optimization*. Nat. Rev. Drug Discovery, 2006. **5**(9): p. 730-739.

92. Stewart, M.J., et al., *Structural basis and mechanism of enoyl reductase inhibition by triclosan*. J. Mol. Biol., 1999. **290**(4): p. 859-865.
93. Sivaraman, S., et al., *Structure-activity studies of the inhibition of FabI, the enoyl reductase from Escherichia coli, by triclosan: kinetic analysis of mutant FabIs*. Biochemistry, 2003. **42**(15): p. 4406-4413.
94. Ward, W.H.J., et al., *Kinetic and structural characteristics of the inhibition of enoyl (acyl carrier protein) reductase by triclosan*. Biochemistry, 1999. **38**(38): p. 12514-12525.
95. Tummino, P.J. and R.A. Copeland, *Residence time of receptor-ligand complexes and its effect on biological function*. Biochemistry, 2008. **47**(32): p. 8465.
96. Swinney, D.C., *Biochemical mechanisms of drug action: what does it take for success?* Nat. Rev. Drug Discovery, 2004. **3**(9): p. 801-808.
97. Lu, H. and P.J. Tonge, *Residence time: Critical information for lead optimization*. Curr. Opin. Chem. Biol., 2010: p. in press.
98. Luckner, S.R., et al., *Crystal structures of Mycobacterium tuberculosis KasA show mode of action within cell wall biosynthesis and its inhibition by thiolactomycin*. Structure, 2009. **17**(7): p. 1004-1013.
99. Cockerill, F.R., et al., *Rapid Identification of a Point Mutation of the Mycobacterium-Tuberculosis Catalase-Peroxidase (Katg) Gene Associated with Isoniazid Resistance*. J. Infect. Dis., 1995. **171**(1): p. 240-245.

100. Tonge, P.J.S., NY, US), Sullivan, Todd (Winsted, CT, US), Johnson, Francis (Setauket, NY, US), *Diphenyl ether antimicrobial compounds*, 2010, Research Foundation of State University of New York (Albany, NY, US): United States.
101. Rozwarski, D.A., et al., *Crystal structure of the Mycobacterium tuberculosis enoyl-ACP reductase, InhA, in complex with NAD(+) and a C16 fatty acyl substrate*. J. Biol. Chem., 1999. **274**(22): p. 15582-15589.
102. Schrodinger, LLC, *The PyMOL Molecular Graphics System, Version 0.99rc6*, 2010.
103. Freundlich, J.S., et al., *Triclosan derivatives: towards potent inhibitors of drug-sensitive and drug-resistant Mycobacterium tuberculosis*. ChemMedChem, 2009. **4**(2): p. 241-248.
104. am Ende, C.W., et al., *Synthesis and in vitro antimycobacterial activity of B-ring modified diaryl ether InhA inhibitors*. Bioorg. Med. Chem. Lett., 2008. **18**(10): p. 3029-3033.
105. Clive, D.L.J. and J. Wang, *A tin hydride designed to facilitate removal of tin species from products of stannane-mediated radical reactions*. J. Org. Chem., 2002. **67**(4): p. 1192-1198.
106. Doyle, M.P., et al., *Reductive deamination of arylamines by alkyl nitrites in N,N-dimethylformamide - Direct conversion of arylamines to aromatic hydrocarbons*. J. Org. Chem., 1977. **42**(22): p. 3494-3498.

107. Kime, D.E. and J.K. Norymberski, *Synthesis of fully aromatic cyclic polyethers*. Journal of the Chemical Society-Perkin Transactions 1, 1977(9): p. 1048-1052.
108. Chhibber, M., et al., *Novel diphenyl ethers: Design, docking studies, synthesis and inhibition of enoyl ACP reductase of Plasmodium falciparum and Escherichia coli*. Bioorg. Med. Chem., 2006. **14**(23): p. 8086-8098.
109. Luckner, S.R., et al., *A slow, tight binding inhibitor of InhA, the enoyl-acyl carrier protein reductase from Mycobacterium tuberculosis*. J. Biol. Chem., 2010. **285**(19): p. 14330-14337.
110. Freundlich, J.S., et al., *Triclosan derivatives: Towards potent inhibitors of drug-sensitive and drug-resistant Mycobacterium tuberculosis*. ChemMedChem, 2009. **4**(2): p. 241-248.
111. Parikh, S.L., G. Xiao, and P.J. Tonge, *Inhibition of InhA, the enoyl reductase from Mycobacterium tuberculosis, by triclosan and isoniazid*. Biochemistry, 2000. **39**(26): p. 7645-7650.
112. Sivaraman, S., et al., *Inhibition of the bacterial enoyl reductase FabI by triclosan: A structure-reactivity analysis of FabI inhibition by triclosan analogues*. J. Med. Chem., 2004. **47**(3): p. 509-518.
113. Yajko, D.M., et al., *Colorimetric method for determining MICs of antimicrobial agents for Mycobacterium tuberculosis*. J. Clin. Microbiol., 1995. **33**(9): p. 2324-2327.

114. Lipinski, C.A., et al., *Experimental and computational approaches to estimate solubility and permeability in drug discovery and development settings*. Adv. Drug Delivery Rev., 2001. **46**(1-3): p. 3-26.
115. Lau, W.M., et al., *Scope and limitations of the co-drug approach to topical drug delivery*. Curr. Pharm. Des., 2008. **14**(8): p. 794-802.
116. Marcoux, J.-F., S. Doye, and S.L. Buchwald, *A general copper-catalyzed synthesis of diaryl ethers*. J. Am. Chem. Soc., 1997. **119**(43): p. 10539-10540.
117. Dai, C.Y. and G.C. Fu, *The first general method for palladium-catalyzed Negishi cross-coupling of aryl and vinyl chlorides: Use of commercially available Pd(P(t-BU)(3))(2) as a catalyst*. J. Am. Chem. Soc., 2001. **123**(12): p. 2719-2724.
118. Sala, C., et al., *Simple model for testing drugs against nonreplicating Mycobacterium tuberculosis*. Antimicrob. Agents Chemother., 2010. **54**(10): p. 4150-4158.
119. Cho, S.H., et al., *Low-oxygen-recovery assay for high-throughput screening of compounds against nonreplicating Mycobacterium tuberculosis*. Antimicrob. Agents Chemother., 2007. **51**(4): p. 1380-1385.
120. Pan, P. and P.J. Tonge, *Targeting InhA, the FASII enoyl-ACP reductase: SAR studies on novel inhibitor scaffolds*. Curr. Top. Med. Chem., 2012. **12**(7): p. 672-693.
121. Stewart, M.J., et al., *Structural basis and mechanism of enoyl reductase inhibition by triclosan*. J. Mol. Biol., 1999. **290**(4): p. 859-865.

122. Levy, C.W., et al., *Molecular basis of triclosan activity*. Nature, 1999. **398**(6726): p. 383-384.
123. Slayden, R.A. and C.E. Barry, *The role of KasA and KasB in the biosynthesis of meromycolic acids and isoniazid resistance in Mycobacterium tuberculosis*. Tuberculosis, 2002. **82**(4-5): p. 149-160.
124. Sullivan, T.J., et al., *High affinity InhA inhibitors with activity against drug-resistant strains of Mycobacterium tuberculosis*. ACS Chem. Biol., 2006. **1**(1): p. 43-53.
125. Freundlich, J.S., et al., *Triclosan derivatives: Towards potent inhibitors of drug-sensitive and drug-resistant Mycobacterium tuberculosis*. ChemMedChem, 2009. **4**(2): p. 241-248.
126. Ryzhkov, L.R., *Radical nature of pathways to alkene and ester from thermal decomposition of primary alkyl diacyl peroxide*. J. Org. Chem., 1996. **61**(8): p. 2801-2808.
127. Parikh, S., et al., *Roles of tyrosine 158 and lysine 165 in the catalytic mechanism of InhA, the enoyl-ACP reductase from Mycobacterium tuberculosis*. Biochemistry, 1999. **38**(41): p. 13623-13634.
128. Copeland, R.A., *Evaluation of enzyme inhibitors in drug discovery: A guide for medicinal chemists and pharmacologists* 2005: Wiley, Hoboken. NJ. 141-154.
129. Jang, G.R., R.Z. Harris, and D.T. Lau, *Pharmacokinetics and its role in small molecule drug discovery research*. Med. Res. Rev., 2001. **21**(5): p. 382-396.

130. Thompson, T.N., *Early ADME in support of drug discovery: The rule of metabolic stability studies*. *Curr. Drug Metab.*, 2000. **1**(3): p. 215-241.
131. Lipinski, C.A., et al., *Experimental and computational approaches to estimate solubility and permeability in drug discovery and development settings*. *Advanced drug delivery reviews*, 2001. **46**(1-3): p. 3-26.
132. Caldwell, J., I. Gardner, and N. Swales, *An introduction to drug disposition: the basic principles of absorption, distribution, metabolism, and excretion*. *Toxicol. Pathol.*, 1995. **23**(2): p. 102-114.
133. Lin, J., et al., *The role of absorption, distribution, metabolism, excretion and toxicity in drug discovery*. *Curr. Top. Med. Chem.*, 2003. **3**(10): p. 1125-1154.
134. Thompson, T.N., *Optimization of metabolic stability as a goal of modern drug design*. *Med. Res. Rev.*, 2001. **21**(5): p. 412-449.
135. Black, J.G., D. Howes, and T. Rutherford, *Percutaneous absorption and metabolism of Irgasan Dp300*. *Toxicology*, 1975. **3**(1): p. 33-47.
136. Wang, L.-Q., C.N. Falany, and M.O. James, *Triclosan as a substrate and inhibitor of 3'-phosphoadenosine 5'-phosphosulfate-sulfotransferase and UDP-glucuronosyl transferase in human liver fractions*. *Drug Metab. Dispos.*, 2004. **32**(10): p. 1162-1169.
137. England, K., et al., *Substituted diphenyl ethers as a broad-spectrum platform for the development of chemotherapeutics for the treatment of tularaemia*. *J. Antimicrob. Chemother.*, 2009. **64**(5): p. 1052-1061.

138. Yamashiki, N., et al., *Presence of phenol UDP-glucuronosyltransferase in bovine alveolar macrophages and bronchial epithelial cells*. Toxicology, 2002. **176**(3): p. 221-227.
139. Aytemir, M.D., E. Septioglu, and U. Calis, *Synthesis and anticonvulsant activity of new kojic acid derivatives*. Arzneimittelforschung., 2010. **60**(1): p. 22-29.
140. Bransova, J., et al., *Antileukemic activity of 4-pyranone derivatives*. Int. J. Biochem. Cell Biol., 1995. **27**(7): p. 701-706.
141. Bransova, J., et al., *5-benzyloxy-2-thiocyanatomethyl-4-pyranone, a novel heterocyclic compound: synthesis, structure determination and effects on neoplastic cell growth*. Anticancer Res., 1997. **17**(2A): p. 1175-1178.
142. Yeates, C.L., et al., *Synthesis and structure-activity relationships of 4-pyridones as potential antimalarials*. J. Med. Chem., 2008. **51**(9): p. 2845-2852.
143. Aytemir, M.D. and B. Ozcelik, *A study of cytotoxicity of novel chlorokojic acid derivatives with their antimicrobial and antiviral activities*. Eur. J. Med. Chem., 2010. **45**(9): p. 4089-4095.
144. Takahata, S., et al., *Discovery of 4-pyridone derivatives as specific inhibitors of enoyl-acyl carrier protein reductase (FabI) with antibacterial activity against Staphylococcus aureus*. J. Antibiot., 2007. **60**(2): p. 123-128.

145. Kitagawa, H., et al., *4-Pyridone derivatives as new inhibitors of bacterial enoyl-ACP reductase FabI*. *Bioorg. Med. Chem.*, 2007. **15**(2): p. 1106-1116.
146. Kitagawa, H., et al., *Phenylimidazole derivatives of 4-pyridone as dual inhibitors of bacterial enoyl-acyl carrier protein Reductases FabI and FabK*. *J. Med. Chem.*, 2007. **50**(19): p. 4710-4720.
147. Yum, J.H., et al., *In vitro activities of CG400549, a novel FabI inhibitor, against recently isolated clinical staphylococcal strains in Korea*. *Antimicrob. Agents Chemother.*, 2007. **51**(7): p. 2591-2593.
148. CrystalGenomics, *Antibacterial Fab I Inhibitors*, 2004. p. 54.
149. Zweifel, G.S. and M.H. Nantz, *Modern organic synthesis : an introduction* 2007, New York: W.H. Freeman. x, 477 p.
150. Layton, C.J. and H.W. Hellinga, *Thermodynamic analysis of ligand-induced changes in protein thermal unfolding applied to high-throughput determination of ligand affinities with extrinsic fluorescent dyes*. *Biochemistry*, 2010. **49**(51): p. 10831-10841.
151. <http://www.thermofluor.org/>.
152. Mahendrarajah, K., et al., *A high-throughput fluorescence chemical denaturation assay as a general screen for protein-ligand binding*. *Anal. Biochem.*, 2011. **411**(1): p. 155-157.
153. Paul, S.M., et al., *How to improve R&D productivity: the pharmaceutical industry's grand challenge*. *Nat. Rev. Drug Discovery*, 2010. **9**(3): p. 203-214.

154. Adams, C.P. and V.V. Brantner, *Estimating the cost of new drug development: Is it really \$802 million?* Health Aff. (Millwood), 2006. **25**(2): p. 420-428.
155. Walter, C.L., A. Shah, and M. Nolte, *Strategies to support drug discovery through integration of systems and data.* Drug Discov. Today, 2007. **12**(15-16): p. 634-639.
156. Kola, I. and J. Landis, *Can the pharmaceutical industry reduce attrition rates?* Nat. Rev. Drug Discovery, 2004. **3**(8): p. 711-715.
157. Copeland, R., *The dynamics of drug-target interactions: drug target residence time and its impact on efficacy and safety.* Expert Opin Drug Discov, 2010. **5**(4): p. 1-6.
158. Copeland, R.A., D.L. Pompliano, and T.D. Meek, *Drug-target residence time and its implications for lead optimization.* Nat. Rev. Drug Discov., 2006. **5**(9): p. 730-739.
159. Zhang, R. and F. Monsma, *The importance of drug-target residence time.* Curr. Opin. Drug Discov. Devel., 2009. **12**(4): p. 488-496.
160. Tummino, P.J. and R.A. Copeland, *Residence time of receptor-ligand complexes and its effect on biological function.* Biochemistry, 2008. **47**(20): p. 5481-5492.
161. Lu, H. and P.J. Tonge, *Drug-target residence time: critical information for lead optimization.* Curr. Opin. Chem. Biol., 2010. **14**(4): p. 467-474.
162. Rawat, R., A. Whitty, and J. Tonge Peter, *The isoniazid-NAD adduct is a slow, tight-binding inhibitor of InhA, the Mycobacterium tuberculosis enoyl*

- reductase: adduct affinity and drug resistance*. Proc. Natl. Acad. Sci. U. S. A., 2003. **100**(24): p. 13881-13886.
163. Swinney, D.C., *Biochemical mechanisms of new molecular entities (NMEs) approved by United States FDA during 2001-2004: Mechanisms leading to optimal efficacy and safety*. Curr. Top. Med. Chem., 2006. **6**(5): p. 461-478.
164. Copeland, R.A., D.L. Pompliano, and T.D. Meek, *Drug-target residence time and its implications for lead optimization*. Nat. Rev. Drug Discovery, 2006. **5**(9): p. 730-739.
165. Copeland, R.A., *The dynamics of drug-target interactions: drug-target residence time and its impact on efficacy and safety*. Expert Opinion on Drug Discovery, 2010. **5**(4): p. 305-310.
166. Lu, H. and P.J. Tonge, *Drug-target residence time: critical information for lead optimization*. Curr. Opin. Chem. Biol., 2010. **14**(4): p. 467-474.
167. Swinney, D.C., *Can binding kinetics translate to a clinically differentiated drug? From theory to practice*. Lett. Drug Des. Discovery, 2006. **3**(8): p. 569-574.
168. Lu, H., et al., *Slow-onset inhibition of the FabI enoyl reductase from francisella tularensis: residence time and in vivo activity*. ACS Chem. Biol., 2009. **4**(3): p. 221-231.
169. Rozwarski, D.A., et al., *Modification of the NADH of the isoniazid target (InhA) from Mycobacterium tuberculosis*. Science, 1998. **279**(5347): p. 98-102.